Systematic Shell-Model Study of Nuclei around ^{208}Pb

Eri Teruya

Thesis for the degree of Doctor of Science

Department of Physics,
Graduate school of Science and Engineering

Saitama University

March, 2017

Abstract

Nuclei in the heavy mass region are attractive to study since neutron-rich nuclei in this mass region are important for understanding the r-process in the nucleosynthesis. Up to now many investigations of nuclear structure for neutron-rich nuclei in the heavy mass region have been carried out. In recent years, for example, nuclei in the superheavy mass region have been produced and intensively studied at Radioactive Isotope Beam Factory (RIBF) in RIKEN.

Theoretically, nuclear structure in the heavy mass region has been studied using various models. For example, these nuclei are studied using mean field theories, where each nucleon motion is treated in a mean field. The nucleus shows various characteristic features and aspects due to the collective motion of nucleons. On the other hand, it is important to investigate the nucleus by considering independent motion of nucleons in addition to the collective motion, since some features of nuclei are determined by specific motion of only one or a few nucleons.

One of the established models that treat motion of nucleons microscopically is the nuclear shell model. By treating the nucleon motion in a completely independent way, the shell model describes irregular patterns of energy spectra in even-even nuclei in the transitional region and structure of odd-mass and doubly-odd nuclei, which are generally difficult to be reproduced in other models. However, only a limited number of shell model calculations have been carried out in the heavy mass region since dimension of shell-model configurations in the calculation becomes huge, then the shell model calculations soon infeasible. In particular, open-shell nuclei with more than mass number 200 require a large dimension of shell-model configurations so that they have not been analyzed enough using the shell model until now. Moreover, in order to understand nuclei deeply, it is necessary to analyze not only each nucleus itself, but also nuclei in that mass region systematically within one framework. However, there are only a limited number of systematic studies in the heavy mass region.

Recently we have devised a new method to reduce the dimension of the shell model configurations by effectively excluding the high-lying states which do not affect the low-lying structure. It enables us to carry out the systematic shell model calculation in the heavy mass region.

The aim of this thesis is to study features, aspects, and systematics of nuclear structure of nuclei around ^{208}Pb using the large scale nuclear shell model. The systematic study is performed for nuclei with less than 126 neutrons and more than 82 protons (nuclei around mass 210; 33 species) and for nuclei with more than 126 neutrons and more than 82 protons (nuclei around mass 220; 23 species). Pb, Bi, Po, At, Rn, and Fr isotopes for even-even, odd-mass, and doubly-odd nuclei are systematically investigated. The energy levels and electromagnetic properties are calculated and compared with experiment. Specific features of each nucleus are analyzed and discussed. Additionally, structure of isomeric states, whose half lives are more than several nanoseconds, are analyzed for each nucleus.

Contents

List of Figures

List of Tables

Chapter 1

Introduction

The nucleus is a many-body system consisting of several to around 300 nucleons and about 3000 species are known at present. The nucleus was first discovered in 1900's by Rutherford's experiment. Since then its synthesis and properties have been studied. Now it is generally accepted that light nuclei up to Lithium isotopes were created at the time of the Big-Bang, and heavy nuclei were later created at the center of stars by nuclear reactions. Recently there is a new hypothesis that heavier mass nuclei might be created by the neutron capture reaction at the time two neutron stars are merged together.

The nucleus shows various specific features according to its neutron and proton numbers. A nucleus with almost the same neutron and proton numbers is relatively stable in the light mass region. However, the nucleus with more neutrons than protons are likely to be stable in the medium and heavy mass regions because of its Coulomb energy. A nucleus with a magic neutron and/or proton number is generally stable. The ground states of these nuclei have a spherical shape. Nuclei away from the magic numbers show vibrational or rotational features. Understanding of these features for each nucleus and also the systematics of them are important.

Features of nuclei in the medium and heavy mass regions have been poorly studied up to now. In particular, neutron-rich nuclei are important for understanding the r-process in the nucleosynthesis. However, a part of the nuclear chart in the heavy neutron rich region remains empty even though some theories predict its existence. Recently many efforts of filling this vacancy have been made. At the Radioactive Isotope Beam Factory (RIBF) in RIKEN, explorations of new elements have been carried out recently [1–3]. The naming right for the new nucleus with $Z = 113$ (Nh) [4] was given for RIKEN at long last in 2016.

Around the doubly-magic nucleus ^{208}Pb, many intriguing features are experimentally known. The nucleus ^{208}Pb is known to exhibit an aspect of a strong core, partly seen in the large excitation energies of the first 2^+ and 3^- states [5]. In the nuclei near the magic numbers, states made by core excitations have been identified. It is important to distinguish these core excited states from normal states to understand nuclear structure of each nucleus.

The importance of the octupole interaction is suggested by several experiments in nuclei with more than 126 neutrons. The low-lying 3^- states and strong $E3$ transitions in these nuclei are considered to be a consequence of the strong octupole correlation. Experimental evidence for the octupole vibration and the octupole deformation were discussed in Rn isotopes [6]. Moreover, many isomers have been identified in these regions.

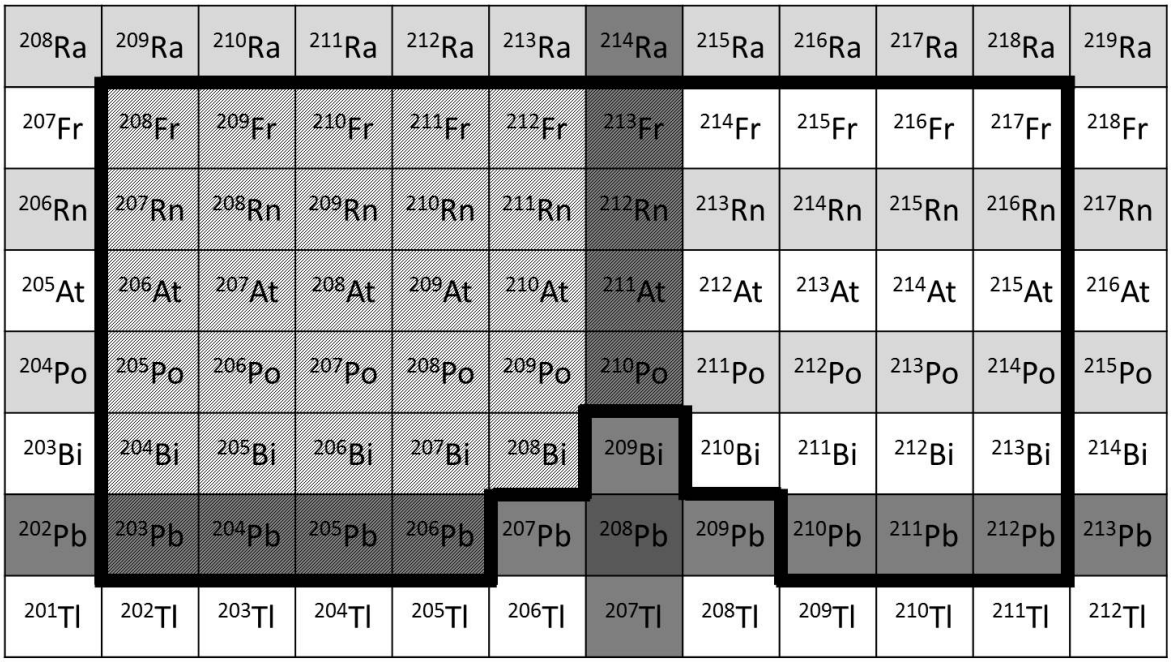

Figure 1.1: The nuclei discussed in this study (nuclei framed by a bold line). The shaded nuclei are treated in Chapter 3 (nuclei around mass 210) and others are treated in Chapter 4 (nuclei around mass 220).

Here, a state with a half life of more than several nanoseconds is called an isomeric state, or an isomer in short. In general the half life of an isomeric state becomes longer because of delicate reasons, for instance, a structural difference of wavefunctions between the isomeric state and the low-lying state connected by the electro-magnetic transition, and a narrow energy gap between the isomeric state and the connected low-lying state [7–9]. Thus a microscopic treatment is necessary to understand its mechanism of being an isomer.

Nuclei in this mass region are attractive to us not only for their own nuclear structure, but also for its connection to the fundamental physics. For example, experimental efforts of observing the electric dipole moment (EDM) have been made using atoms and molecules in this mass region. ^{199}Hg is the most intensively studied system for an observation of the atomic EDM [10]. One of the most promising candidates for observing the finite EDM is a radioactive nucleus, ^{225}Ra. The first trial of measuring the atomic EDM using this nucleus was carried out recently [11]. ^{211}Rn and ^{208}Tl are also candidates for the observation of the atomic EDM. Moreover, Fr and Tl are used for the search of the electron EDM [12,13].

For these reasons, nuclei around ^{208}Pb have been one of the most attractive subjects of research. Thus these nuclei have been extensively studied in both experiment and theory. However, most of theoretical studies were carried out within the framework of the mean field theories and only a few microscopic studies using the nuclear shell model have been carried out until quite recently due to the huge dimension of the shell model configurations that one needs to handle.

The aim of this thesis is to shed light on the nuclear structure of nuclei with more than 82 protons around the ^{208}Pb nucleus through theoretical investigations in the nuclear shell model. Even-even, odd-mass, and doubly-odd nuclei of Pb, Bi, Po, At, Rn, and Fr

isotopes are systematically studied. Here, the nuclei discussed in this thesis are shown in Fig. 1.1. The detailed analysis for each nucleus is carried out to elucidate its nuclear structure. The systematic features of nuclei in this mass region are also discussed.

This thesis is organized as follows. In Chapter 2, our framework of the shell model calculation is given. In Chapter 3, the shell model analysis for nuclei around mass 210 are carried out. Here nuclei with less than 126 neutrons and more than 82 protons near to ^{208}Pb are called "nuclei around mass 210". In this thesis, $^{203-206}$Pb, $^{204-208}$Bi, $^{205-210}$Po, $^{206-211}$At, $^{207-212}$Rn, and $^{208-213}$Fr nuclei are discussed. In Chapter 4, the shell model analysis for nuclei around mass 220 are discussed. Here nuclei with more than 126 neutrons and more than 82 protons near to ^{208}Pb are called "nuclei around mass 220". Here $^{210-212}$Pb, $^{210-213}$Bi, $^{211-214}$Po, $^{212-215}$At, $^{213-215}$Rn, and $^{214-217}$Fr nuclei are discussed. Finally, this study is summarized in Chapter 5. The details of the necessary formula in this thesis are summarized in the Appendix.

Chapter 2

Framework of the nuclear shell model

2.1 Basic concept of the nuclear shell model

The nucleus is a many-body system which consists of a number of neutrons and protons. The nucleons are strongly combined with each other and a nucleus can be considered as a droplet of nucleons. The collective motion is one of notable features of nuclei and one can understand these features thorough collective models such as the liquid model and Interactive-Boson-Model (IBM). On the other hand, the nucleus can be understood by considering motions of each nucleon. In the mean field theories such as the Hartree-Fock (HF) method and the Random-Phase-Approximation (RPA), nucleon motions are treated in a mean field. A model that describes nucleon motions completely in a microscopic way is the nuclear shell model. In the shell model, each nucleon is treated independently and interactions between all nucleons are considered independently.

The concept of the nuclear shell model is based on the fact that nucleons are moving independently in a nucleus suffering the Pauli uncertain principle and the concept of the shell model originates from an experimental observation of the magic numbers. It is well known that the nuclei which have either 2, 8, 20, 28, 50, 82, or 126 neutrons and protons are especially stable. These numbers are called magic numbers and nuclei which have these numbers of nucleons make a closed core. These magic numbers were first explained by Mayer and Jensen in 1949 by introducing a spin orbit coupling, $v(r)l \cdot s$, to the average central potential of the nucleus, where l and s represents the orbital angular momentum and spin of nucleons, respectively [14–16].

In the shell model, nuclear states are constructed by nucleons occupying single particle orbitals. Eigen-wavefunctions are obtained by diagonalizing the shell model Hamiltonian. Due to the configuration mixing by the many-body interaction, a nuclear ground state is not just constructed by nucleons in orbitals from the lowest energy level, but constructed by nucleons in higher orbitals. The dimension of diagonalization becomes huge when the number of treated nucleons increases, so that it is important how one handles this diagonalization or how one decreases the dimension of diagonalization.

The shell model has been applied for various nuclei, especially for light mass nuclei. The features of light nuclei are well described using the shell model. In recent years, the no-core shell model using the *ab*-initio interaction has been applied for nuclei with mass $A < 20$ and the importance of the three-body effect has been suggested [17–20]. The

vanishment of the traditional magic numbers and the appearance of a new magic number was studied using the shell model. For the medium and heavy nuclei, the nuclear structure of nuclei around a doubly-magic nucleus has been also studied using the shell model. For example, the systematic calculations were carried out assuming the ^{40}Ca core [21], the ^{56}Ni core [22, 23], the ^{78}Ni core [24–26], and the ^{132}Sn core [8, 27–32].

2.2 Procedure of the shell model calculation and truncation scheme

The nuclear shell model is one of the successful methods to understand nuclear structure. However, one difficulty in carrying out the shell model is the expansion of the dimension for the diagonalization of the shell model Hamiltonian. The shell model dimension in medium and heavy nuclei amounts to more than 10^{10}, which overwhelmingly exceeds the number of configurations tractable with the present computing power. Thus one needs to settle down this problem when the shell model is applied to medium and heavy nuclei. For example, the Monte Carlo shell model is one of the promising methods and attracts considerable attention, although it takes a lot of computational time [33, 34]. In contrast, the conventional diagonalization approach using the Lanczos diagonalization method requires a truncation of the shell model space [35, 36].

In our shell model code, the shell model dimension is relived according to the following prescription as shown in Fig. 3.14 and it enables us to carry out numerical calculations for medium and heavy nuclei. The following procedure is based on the assumption that interactions between neutrons and protons are not so large and they are separable. In the medium and heavy mass region (especially in neutron rich nuclei), numbers of protons and neutrons in one nucleus are very different and this assumption is reasonable.

First, the neutron eigen-wavefunctions are determined and the neutron interaction $\hat{H}_\nu$ in the neutron space is diagonalized. All the eigen-energies and eigen-wavefunctions are obtained in the neutron(ν)-system,

$$\hat{H}_\nu \left|i, I_i M_i\right\rangle_\nu = E_\nu(i, I_i) \left|i, I_i M_i\right\rangle_\nu , \tag{2.1}$$

where i takes $i = 1, \cdots, L_\nu$ and I_i is spin of the ith state and L_ν is the maximum number of possible states. M_i represents the projection of the angular momentum $M_i = 0$ is taken for even-particle systems and $M_i = 1/2$ for odd-particle systems. The eigen-energies are ordered in increasing order as $E_\nu(1, I_1) \leq E_\nu(2, I_2) \leq \cdots$. Next, the proton eigen-wavefunctions are determined and the proton interaction $\hat{H}_\pi$ is diagonalized. All the eigen-energies and eigen-wavefunctions are obtained in the proton(π)-system,

$$\hat{H}_\pi \left|j, I_j M_j\right\rangle_\pi = E_\pi(j, I_j) \left|j, I_j M_j\right\rangle_\pi , \tag{2.2}$$

where j takes $j = 1, \cdots, L_\pi$ and eigen-energies are ordered in increasing order $E_\pi(1, I_1) \leq E_\pi(2, I_2) \leq \cdots$. Then, by coupling a neutron state and a proton state in the angular momentum space, a neutron-proton basis state is obtained:

$$\begin{aligned} \left|IM, \alpha\right\rangle &= \left[\left|i, I_i\right\rangle_\nu \otimes \left|j, I_j\right\rangle_\pi\right]^{(I)}_M \\ &= \sum_{M_i M_j} (I_i M_i I_j M_j | IM) \left|i, I_i M_i\right\rangle_\nu \left|j, I_j M_j\right\rangle_\pi . \end{aligned} \tag{2.3}$$

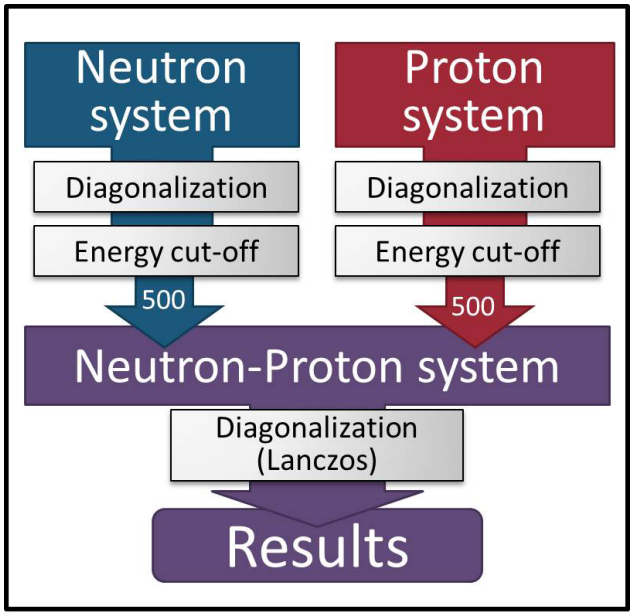

Figure 2.1: The procedure of the truncation of our shell-model code.

Finally, the total hamiltonian is diagonalized as follows,

$$\hat{H}\,|\Phi(I_k;k)\rangle = E(I_k,k)\,|\Phi(I_k;k)\rangle\,. \tag{2.4}$$

Here, k represents the kth state with total spin I_k in the total neutron-proton space and the eigen-state $|\Phi(I_\ell;\ell)\rangle$ is expressed as $|\Phi(I_\ell;\ell)\rangle = \sum_\alpha v_{\ell\alpha}^{(I)}\,|I,\alpha\rangle$ using the basis states in Eq. (2.3). The coefficients $v_{\ell\alpha}^{(I)}$ are obtained by diagonalizing Eq. (2.7).

Here numbers of levels for a neutron system and a proton system are reduced to truncate the total shell model dimension when the neutron-proton system is calculated. Namely, maximum numbers of i and j are cut off to L_c,

$$i,j = 1,\cdots,L_c. \tag{2.5}$$

In this study the $L_c = 500$ is taken for all the calculations. The validity of the cut-off is checked in Sec. 3.4.1.

2.3 Shell model Hamiltonian

The Hamiltonian of a nucleus is derived from the nuclear force [37, 38]. However, the interaction in the many-body nuclear system differs from the bare nuclear force between two nucleons due to various many-body effects. For example, we generally consider a limited model space when we perform a shell model calculation and we need to incorporate this effect. Therefore we consider the effective shell model interaction. The shell-model Hamiltonian of the A-nucleon system which considers up to two-body interactions is generally written as

$$\hat{H} = \sum_{i=1}^{A}\hat{T}_i + \frac{1}{2}\sum_{i,j=1}^{A}V_{ij}, \tag{2.6}$$

where the first term represents a one-body interaction and the second term represents a two-body interaction. This effective Hamiltonian has been derived in many mass regions by many people using the theory of effective interaction. However, the number of two-body interactions V_{ij} becomes large in the medium and heavy nuclei due to the expansion of the single particle levels and it is not reasonable to use this type of the Hamiltonian. Thus we employ the effective interaction which simply incorporates important nature of the nucleus. In this study we take the following Hamiltonian which consists of the pairing plus quadrupole-quadrupole and multipole interactions.

The adopted effective shell-model Hamiltonian is written as

$$\hat{H} = \hat{H}_\nu + \hat{H}_\pi + \hat{H}_{\nu\pi}, \tag{2.7}$$

where $\hat{H}_\nu$, $\hat{H}_\pi$ and $\hat{H}_{\nu\pi}$ represent neutron, proton and neutron-proton interactions, respectively. The interactions among like nucleons are expressed as

$$\hat{H}_\tau = \hat{H}_{c\tau} + \hat{H}_{h\tau}. \tag{2.8}$$

The first term $\hat{H}_{c\tau}$ ($\tau = \nu$ or π) represents the conventional pairing plus quadrupole interaction, which consists of spherical single-particle energies, the monopole-pairing (MP) interaction, the quadrupole-pairing (QP) interaction, and the quadrupole-quadrupole (QQ) interaction,

$$\hat{H}_{c\tau} = \sum_{jm} \varepsilon_{j\tau} c^\dagger_{jm\tau} c_{jm\tau} - G_{0\tau} \hat{P}^{\dagger(0)}_\tau \hat{P}^{(0)}_\tau - G_{2\tau} \hat{P}^{\dagger(2)}_\tau \cdot \hat{\tilde{P}}^{(2)}_\tau - \kappa_\tau : \hat{Q}_\tau \cdot \hat{Q}_\tau :, \tag{2.9}$$

where :: represents the normal ordering. Here $c^\dagger_{jm\tau}$ and $c_{jm\tau}$ are the nucleon creation and annihilation operators, respectively, and (jm) stands for a shorthand notation of all the quantum numbers to uniquely specify a harmonic-oscillator basis state $|n\ell jm\rangle$. The monopole pair-creation operator $\hat{P}^{\dagger(0)}_\tau$, the quadrupole pair-creation operator $\hat{P}^{\dagger(2)}_{M\tau}$, and the quadrupole operator $\hat{Q}_{M\tau}$ are defined by

$$\hat{P}^{\dagger(0)}_\tau = \sum_j \frac{\sqrt{2j+1}}{2} A^{\dagger(0)}_{0\tau}(jj), \tag{2.10}$$

$$\hat{P}^{\dagger(2)}_{M\tau} = \sum_{j_1 j_2} Q_{j_1 j_2} A^{\dagger(2)}_{M\tau}(j_1 j_2), \tag{2.11}$$

$$\hat{\tilde{P}}^{(2)}_{M\tau} = (-)^M \left\{ \hat{P}^{\dagger(2)}_{-M\tau} \right\}^\dagger, \tag{2.12}$$

$$\hat{Q}_{M\tau} = \sum_{j_1 j_2} Q_{j_1 j_2} [c^\dagger_{j_1\tau} \tilde{c}_{j_2\tau}]^{(2)}_M, \tag{2.13}$$

with

$$\tilde{c}_{jm\tau} = (-1)^{j-m} c_{j-m\tau}, \tag{2.14}$$

$$Q_{j_1 j_2} = -\frac{\left\langle j_1 \left\| r^2 Y^{(2)} \right\| j_2 \right\rangle}{\sqrt{5}}. \tag{2.15}$$

Here the creation operator of a pair of like-nucleons in the orbitals j_1 and j_2 with the total angular momentum J and its projection M is constructed by

$$\begin{aligned} A^{\dagger(J)}_M(j_1 j_2) &= \sum_{m_1 m_2} (j_1 m_1 j_2 m_2 | JM) c^\dagger_{j_1 m_1} c^\dagger_{j_2 m_2} \\ &= [c^\dagger_{j_1} c^\dagger_{j_2}]^{(J)}_M, \end{aligned} \tag{2.16}$$

where $(j_1 m_1 j_2 m_2 | JM)$ stands for a Clebsch-Gordan coefficient. Here isospin notation τ has been skipped.

The second term $\hat{H}_{h\tau}$ in Eq. (2.8) represents the newly introduced higher angular-momentum interactions, which consists of higher multipole-pairing (HMP) interactions,

$$\hat{H}_{h\tau} = -\sum_{L=4,6,8,10} G_{L\tau} \hat{P}^{\dagger(L)}_{\tau} \cdot \hat{\tilde{P}}^{(L)}_{\tau}. \tag{2.17}$$

Here the positive-parity multipole pair-creation operator, $\hat{P}^{\dagger(L)}_{\tau}$ ($L = 4, 6, 8, 10$), is defined as

$$\hat{P}^{\dagger(L)}_{M\tau} = \sum_{j_1 j_2} H^{(L)}_{j_1 j_2} A^{\dagger(L)}_{M\tau}(j_1 j_2), \tag{2.18}$$

with

$$H^{(L)}_{j_1 j_2} = -\frac{\left\langle j_1 \left\| Y^{(L)} \right\| j_2 \right\rangle}{\sqrt{2L+1}}, \tag{2.19}$$

and

$$\hat{\tilde{P}}^{(L)}_{M\tau} = (-1)^M \left\{ \hat{P}^{\dagger(L)}_{-M\tau} \right\}^{\dagger}. \tag{2.20}$$

In other words each HMP operator is an extension of the quadrupole pair-creation operator without radial dependence.

The interaction between neutrons and protons $\hat{H}_{\nu\pi}$ is given as

$$\hat{H}_{\nu\pi} = -\kappa_{\nu\pi} \hat{Q}_{\nu} \cdot \hat{Q}_{\pi}, \tag{2.21}$$

where $\hat{Q}_{\tau}$ is the quadrupole operator defined by Eq. (2.13). Harmonic-oscillator states are used as the single-particle basis states with the oscillator parameter $b = \sqrt{\hbar/(M\omega)}$.

The basic form of the adopted Hamiltonian is given as described. In addition to the above Hamiltonian, we introduce other types of interactions in some nuclei for better description of nuclei. The strengths of each interaction are determined to reproduce experimental energy levels systematically.

2.4 Framework of the pair-truncated shell model

In this thesis, the pair-truncated shell model (PTSM) [39–41] is also used for analysis. The PTSM is one of the shell model approaches, but a gigantic shell-model space is restricted to the space mainly made of only low-spin collective pairs. It is well known that the collective motion is important to describe nucleus. In the PTSM calculation, the S-pair (angular momenta $L = 0$), D-pair ($L = 2$), and G-pair ($L = 4$) are introduced as follows:

$$S^{\dagger} = \sum_{j} \alpha_j A^{\dagger(0)}_0(jj), \tag{2.22}$$

$$D^{\dagger}_M = \sum_{j_1 j_2} \beta_{j_1 j_2} A^{\dagger(2)}_M(j_1 j_2), \tag{2.23}$$

$$G^{\dagger}_M = \sum_{j_1 j_2} \gamma_{j_1 j_2} A^{\dagger(4)}_M(j_1 j_2), \tag{2.24}$$

where $A^{\dagger(J)}_M(j_1 j_2)$ is the pair creation operator of nucleons defined in Eq. (2.16). The structure coefficient α is determined as

$$\delta \left\langle S^{n_s} \left| \hat{H} \right| S^{n_s} \right\rangle = 0. \tag{2.25}$$

After determining α, the structure coefficient β is also determined as

$$\delta \left\langle S^{n_s-1} D \left| \hat{H} \right| S^{n_s-1} D \right\rangle = 0, \tag{2.26}$$

and γ is determined in the same way. Here the Hamiltonian $\hat{H}$ is the same as one used for the shell-model calculation and n_s is the number of S-pairs.

The many-body wavefunctions of even-nucleon systems for neutrons or protons are created by applying the pair creation operators $\hat{S}^\dagger$, $\hat{D}^\dagger$ and $\hat{G}^\dagger$ to the inert core $|-\rangle$:

$$|S^{n_s} D^{n_d} G^{n_g} I\eta\rangle = (\hat{S}^\dagger)^{n_s} (\hat{D}^\dagger)^{n_d} (\hat{G}^\dagger)^{n_g} |-\rangle \,, \tag{2.27}$$

where I is the total angular momentum, and η, an additional quantum number required to completely specify the states. Here, the angular momentum coupling is carried out exactly, but it is not denoted explicitly for simplicity. For a description of odd-nucleon systems, we add an unpaired nucleon in the j orbital to the even-nucleon system. The state is now written as

$$|j S^{n_s} D^{n_d} G^{n_g} I\eta\rangle = \left[\hat{c}^\dagger_j \, |S^{n_s} D^{n_d} G^{n_g} I'\eta\rangle \right]^{(I)} . \tag{2.28}$$

The odd-mass state with neutron odd and proton even for total spin I and its projection M is written as a product of the above odd-neutron state and the even-proton state:

$$|\Phi(IM\eta)\rangle = \left[|j_n S^{\bar{n}_s}_n D^{\bar{n}_d}_n G^{\bar{n}_g}_n I_n \eta_n\rangle \otimes \left| S^{n_s}_p D^{n_d}_p G^{n_g}_p I_p \eta_p \right\rangle \right]^{(I)}_M , \tag{2.29}$$

where $2(\bar{n}_s + \bar{n}_d + \bar{n}_g) + 1$ and $2(n_s + n_d + n_g)$ are the numbers of valence neutrons and protons, respectively. The odd-mass state with neutron even and proton odd is written in the same way. In addition to the S-, D-, and G-pairs, noncollective pairs are introduced depending on nuclei for a better description of nuclear states. These newly introduced pairs will be described in each part of discussions.

Chapter 3

Analysis for nuclei around mass 210

3.1 Nuclei around mass 210

In this Chapter, we analyze structure of $^{203-206}$Pb, $^{204-208}$Bi, $^{205-210}$Po, $^{206-211}$At, $^{207-212}$Rn, and $^{208-213}$Fr nuclei. Nuclei in this mass region have less than 126 neutrons and more than 82 protons. Besides ^{206}Pb, ^{207}Pb, and ^{208}Pb nuclei which are stable nuclei, these nuclei are relatively stable and their half lives are over a year to several seconds.

Experimentally this mass region is one of a extensively studied region. In recent years, a number of experimental investigations have been carried out in these nuclei [42–50]. Energy spectra for high-lying states and new high-spin isomers are observed in several nuclei. For example, spectroscopy were carried out for ^{210}Fr and the high-spin structure was studied using the ^{197}Au(^{18}O, $5n$)^{210}Fr reaction [50]. High-spin states were newly constructed and their spins were assigned. An isomer was observed which decays to a lower state via the $E3$ transition and its configuration was assigned. Energy spectra up to nearly 10 MeV were newly constructed in ^{206}Bi using γ-ray coincidence spectroscopy following deep-inelastic reactions with the ^{76}Ge + ^{208}Bi system [47]. Some isomers were found to arise from the ^{208}Pb core excitations.

Theoretically, microscopic shell-model calculations for single-closed nuclei were carried out assuming the ^{208}Pb core [51–55] and also for some open-shell nuclei with a few valence particles [56, 57]. Using a few valence particles for the shell-model configurations, the measured magnetic moments of the isomeric 8_1^+ states in $^{210-214}$Rn are well described by the assignment of the $(\pi h_{9/2}^4)$ configuration [58]. In a paper by Caurier and others [55], $N = 126$ isotones from ^{210}Po to ^{218}U were calculated using a realistic two-body interaction derived from the Kuo-Herling interaction. They well described energy levels and transition rates for these nuclei. The nucleon pair approximation was applied for low-lying states of nuclei around ^{208}Pb by Xu and others [59]. The SD-pair calculation was carried out systematically for 33 even-even and odd-mass nuclei with mass $A = 202 - 212$. They calculated energy levels and transition rates below 2.0 MeV. In the preliminary study [60], the shell-model calculations were carried out for even-even Po and Rn isotopes. A phenomenological monopole and quadrupole pairing plus quadrupole-quadrupole interaction was used for the effective interaction. The experimental energy levels of the low-lying states were well reproduced except for the 8_1^+ states, where the level ordering of the 6_1^+ and 8_1^+ states was predicted in reverse. Except for these shell model studies, several mean field approaches were applied. For example, low-lying near-yrast states were analyzed in terms of the interacting boson plus two quasiparticles model [61], where one of the bosons

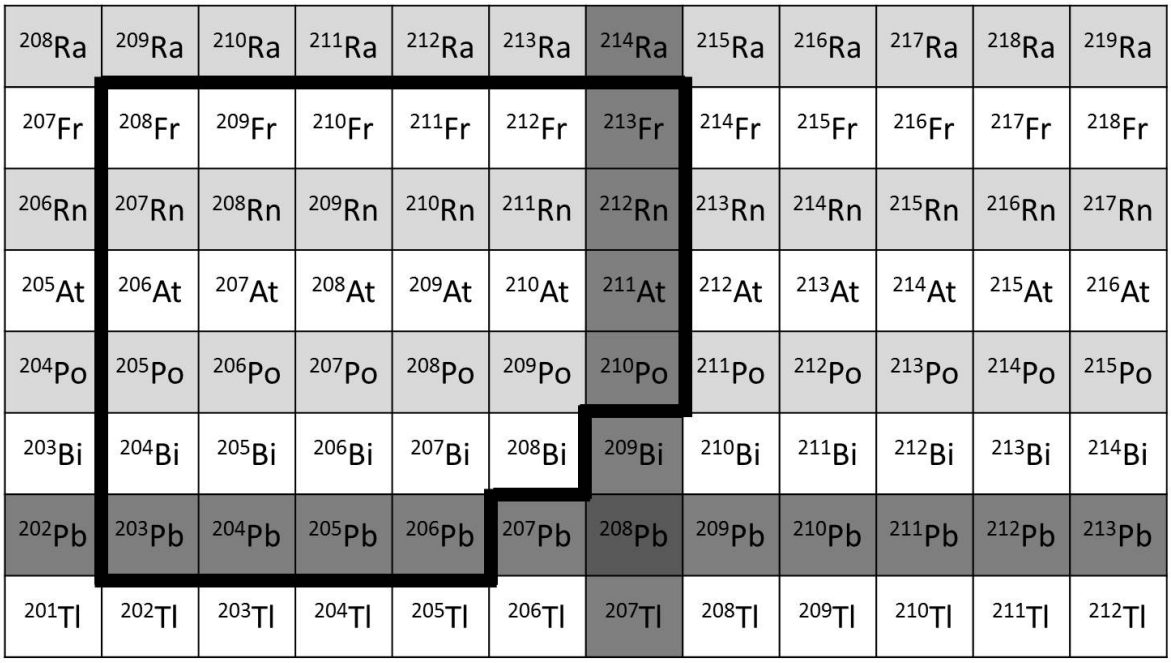

Figure 3.1: The nuclei discussed in this Chapter (nuclei framed by a bold line). The shaded nuclei are nuclei which have the magic number 82 protons and 126 neutrons.

is replaced by a pair of nucleons at high spin [62].

As described above, there have been already several systematic studies using the shell model. However, the numbers of treated nuclei and nuclear states are limited in most of the studies, and especially open shell nuclei and odd-mass and doubly-odd mass nuclei are studied enough. Thus it is necessary to analyze nuclear structure systematically using one set of the credible framework.

In this Chapter, even-even, odd-mass, and doubly-odd nuclei for of $_{82}$Pb, $_{83}$Bi, $_{84}$Po, $_{85}$At, $_{86}$Rn, and $_{87}$Fr isotopes with up to five neutron-holes and five proton-particles systems are treated assuming ^{208}Pb as a doubly magic core. The treated nuclei are figured in Fig. 3.1. The energy spectra and electromagnetic properties are calculated and compared with the experimental data. Isomeric states are analyzed in terms of the shell-model configurations. Furthermore, several features are analyzed at the end of this Chapter.

3.2 Theoretical framework for nuclei around mass 210

For single-particle levels, all the six $0h_{9/2}$, $1f_{7/2}$, $0i_{13/2}$, $2p_{3/2}$, $1f_{5/2}$ and $2p_{1/2}$ orbitals in the major shell between the magic numbers 82 and 126 are taken into account for both neutrons and protons. Neutrons are treated as holes and protons are treated as particles. The single-particle energies ε_τ ($\tau = \nu$ or π) employed in the present calculations are listed in Table 3.1, which are adopted from the experimental energy levels of ^{209}Bi (for proton single-particle energies) and ^{207}Pb (for neutron single-hole energies). As for each neutron or proton $0i_{13/2}$ orbital, it is assumed that the energy of the single-particle orbital

Table 3.1: Adopted single-particle energies ε_τ ($\tau = \nu$ or π) for neutron holes and proton particles (in MeV). The energies for the neutron $0i_{13/2}$ and the proton $0i_{13/2}$ orbitals are changed linearly with numbers of valence neutron holes ($\bar{N}_\nu$) and proton particles (N_π). Definitions of $\epsilon_\nu(i_{13/2})$ and $\epsilon_\pi(i_{13/2})$ are given in the text.

j	$2p_{1/2}$	$1f_{5/2}$	$2p_{3/2}$,	$0i_{13/2}$	$1f_{7/2}$	$0h_{9/2}$
ε_ν	0.000	0.570	0.898	$\epsilon_\nu(i_{13/2})$	2.340	3.415
ε_π	3.634	2.826	3.119	$\epsilon_\pi(i_{13/2})$	0.896	0.000

changes linearly with the numbers of valence neutron holes and proton particles. They are determined (in MeV) as follows,

$$\epsilon_\nu(0i_{13/2}) = -0.065\bar{N}_\nu + 1.698, \tag{3.1}$$
$$\epsilon_\pi(0i_{13/2}) = -0.050N_\pi + 1.659, \tag{3.2}$$

where $\bar{N}_\nu$ and N_π represent the number of valence neutron holes and valence proton particles, respectively. The number dependence of the single-particle energies in the $0i_{13/2}$ orbitals conforms with the experimentally suggested value when $N_\pi = 1$ and $\bar{N}_\nu = 1$. This number dependence is introduced for a better reproduction of the low-lying positive parity states of odd-mass nuclei after adjusting two-body interactions.

The adopted Hamiltonian is the same as described in Sec. 2.3. However, we introduce the following interaction for protons in addition to Eq. (2.7),

$$\hat{H}^{(8)}(\pi h_{9/2}f_{7/2}) = -G^{(8)}_{\pi h_{9/2}f_{7/2}}\hat{P}^{\dagger(8)}_\pi\left(h_{9/2}f_{7/2}\right)\cdot\hat{\tilde{P}}^{(8)}_\pi\left(h_{9/2}f_{7/2}\right), \tag{3.3}$$

with

$$\hat{P}^{\dagger(8)}_{M\pi}\left(h_{9/2}f_{7/2}\right) = \left[c^\dagger_{h_{9/2}}c^\dagger_{f_{7/2}}\right]^{(8)}_M. \tag{3.4}$$

Here, two protons in the $0h_{9/2}$ and $1f_{7/2}$ orbitals are coupled with spin 8 and positive parity, which is the maximum spin available between these two orbitals. $c^\dagger_j$ is the nucleon creation operator in the orbital j. We call this additional pairing interaction with spin 8 between two protons in the $0h_{9/2}$ and $1f_{7/2}$ orbitals, $\hat{H}^{(8)}(\pi h_{9/2}f_{7/2})$, the MP-8 interaction. The necessity of this interaction is discussed and its effects are analyzed in Sec. 3.4.3.

The adopted two-body interaction strengths are listed in Table 3.2. Only one set of strengths is adopted for all the nuclei for this mass region.

For $E2$ transition rates and quadrupole moments, the effective charges are taken as $e_\nu = -0.85e$ for neutrons and $e_\pi = 1.50e$ for protons. For magnetic moments, the adopted gyromagnetic ratios for orbital angular momenta are $g_{\ell\nu} = 0.00$, $g_{\ell\pi} = 1.00$, and those for spin are $g_{s\nu} = -1.91$ and $g_{s\pi} = 2.79$, which are free-nucleon g factors attenuated by a factor of 0.5. These effective charges and gyromagnetic ratios are adjusted to reproduce the experimental data in single-closed nuclei.

Table 3.2: Strengths of adopted two-body interactions between neutrons (ν-ν) and those between protons (π-π). G_0 and G_2 indicate the strengths of the monopole (MP) and quadrupole-pairing (QP) interactions between like nucleons. G_L ($L = 4, 6, 8, 10$) denote the strengths for higher multipole-pairing (HMP) interactions between like nucleons. The strength of the proton two-body interaction between the $0h_{9/2}$ and $1f_{7/2}$ orbitals (MP-8) is taken as $G^{(8)}_{\pi h_{9/2} f_{7/2}} = 0.50$. The strength of the $Q_\nu Q_\pi$ interaction between neutrons and protons is taken as $\kappa_{\nu\pi} = -0.060$. The strengths of the MP, HMP, and MP-8 interactions are given in units of MeV. The strengths of the QP and QQ interactions are given in units of MeV/b^4 using the oscillator parameter $b = \sqrt{\hbar/M\omega}$.

	G_0	G_2	G_4	G_6	G_8	G_{10}
ν-ν	0.145	0.013	0.500	0.500	1.100	2.000
π-π	0.145	0.013	0.400	0.400	−0.600	0.000

3.3 Theoretical results for nuclei around mass 210

In this section, the theoretical results are given for each nucleus. The energy spectra, $E2$ transition rates, magnetic moments, and quadrupole moments are calculated. For energy spectra, up to four observed energy levels are shown from the yrast state for each spin and parity in experiment. As for the theoretical states, two levels for each spin and parity from the lowest level are shown in general. If third or fourth states are observed in experiment, third or fourth energy levels are shown in theory.

In this section, isomeric states are also investigated. There are several reasons why states become isomers. Due to their reasons for existence, they are classified as K isomers, spin-gap isomers, shape isomers, and so on [7]. Many isomers in this region are spin-gap isomers, which do not undertake gamma transitions with low-spin change, such as $E2$ or $M1$ transitions, because of the large spin difference between initial and final states. In particular, many of the isomers whose half-lives are longer than few seconds are known to be spin-gap isomers. Here, isomeric states are analyzed in terms of the shell-model configurations.

3.3.1 Pb isotopes

Here $^{203-206}$Pb isotopes are discussed. Figure 3.2 shows the theoretical energy spectra for even-even Pb isotopes in comparison with the experimental data [63,65,67]. Not only the yrast states, but also non-yrast states are excellently reproduced. The 3^-_1 states in both ^{206}Pb and ^{204}Pb, which are known to be made by core excitations, are beyond the present framework. Similarly, the 1^- states at 3.744 and 4.329 MeV and 2^- states at 3.980 and 4.317 MeV for ^{206}Pb also are seemingly made by core excitations.

In both nuclei, states whose spin and parity is assigned as 8^+ are not observed experimentally below 4 MeV. From the fact that the experimental 10^+_1 states decay to the 9^-_1

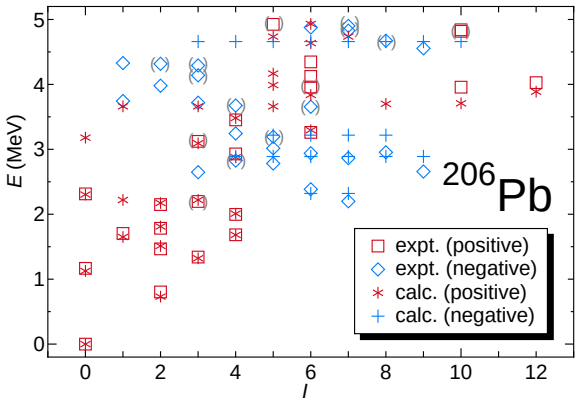

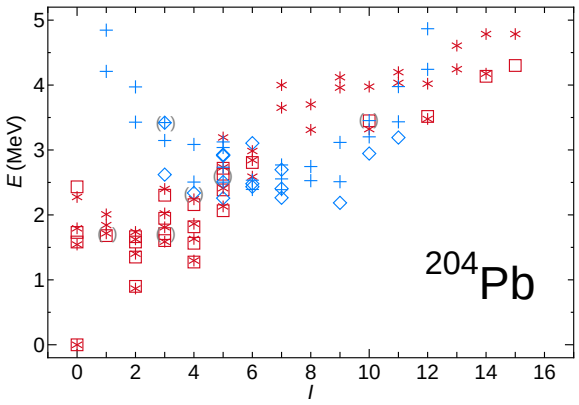

Figure 3.2: (color on line) Theoretical energy spectra for even-even Pb isotopes in comparison with the experimental data. The squares and diamonds represent experimental positive and negative parity states, respectively. The asterisks and crosses represent theoretical positive and negative parity states, respectively. The experimental data are taken from Refs. [63–67]. Ambiguous states are shown with parentheses.

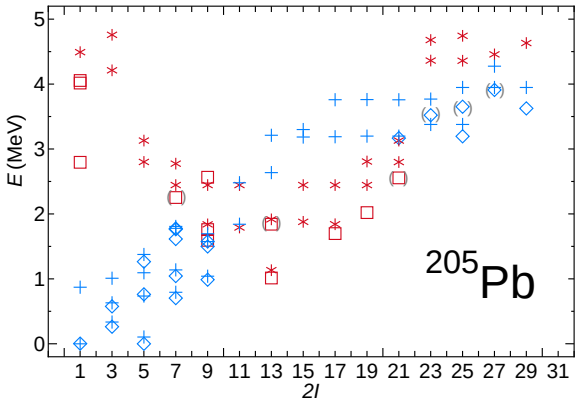

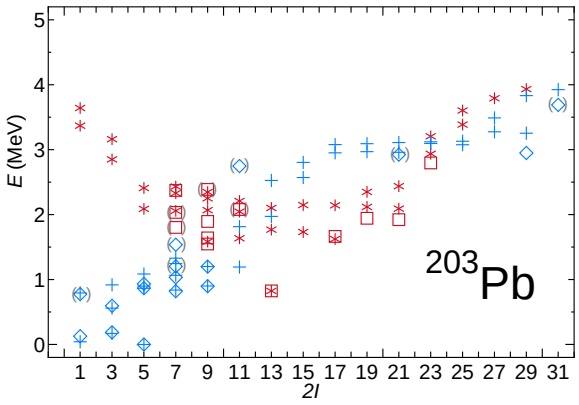

Figure 3.3: (color on line) Theoretical energy spectra for odd-mass Pb isotopes in comparison with the experimental data. The squares and diamonds represent experimental positive and negative parity states, respectively. The asterisks and crosses represent theoretical positive and negative parity states, respectively. The experimental data are taken from Refs. [63–67]. Ambiguous states are shown with parentheses.

Table 3.3: Comparison between the experimental $B(E2)$ values (expt.) and the theoretical results (calc.) for Pb isotopes (in W.u.). The experimental data are taken from Refs. [63–67].

	$B(E2)$	
^{206}Pb	expt.	calc.
$2_1^+ \to 0_1^+$	2.80(9)	2.939
$4_1^+ \to 2_1^+$		3.160
$6_1^+ \to 4_1^+$		1.931
$8_1^+ \to 6_1^+$		0.324
$12_1^+ \to 10_1^+$	0.34(6)	0.281
$6_1^- \to 7_1^-$	0.08^{+31}_{-8}	0.064
^{204}Pb	expt.	calc.
$2_1^+ \to 0_1^+$	4.69(5)	4.262
$4_1^+ \to 2_1^+$	0.00382(9)	0.062
$6_1^+ \to 4_1^+$		0.089
$8_1^+ \to 6_1^+$		0.002
$0_2^+ \to 2_1^+$	0.81(25)	0.078
$7_1^- \to 5_1^-$	$\sim$0.6	0.064
$7_1^- \to 9_1^-$	0.15^{+4}_{-6}	0.004
^{205}Pb	expt.	calc.
$1/2_1^- \to 5/2_1^-$	0.0108(4)	0.199
$3/2_1^- \to 5/2_1^-$		1.095
$3/2_1^- \to 1/2_1^-$		0.032
$7/2_1^- \to 5/2_1^-$		3.960
$7/2_1^- \to 3/2_1^-$		0.003
$25/2_1^- \to 21/2_1^-$	0.053(10)	0.282
$29/2_1^- \to 25/2_1^-$	0.7317(20)	1.021
$17/2_1^+ \to 13/2_1^+$	0.13009(20)	2.618
$19/2_1^+ \to 17/2_1^+$	~ 0.14	0.004
$21/2_1^+ \to 17/2_1^+$	0.01694(5)	3.160
^{203}Pb	expt.	calc.
$1/2_1^- \to 5/2_1^-$	0.96(6)	0.792
$3/2_1^- \to 5/2_1^-$		0.306
$3/2_1^- \to 1/2_1^-$		0.032
$7/2_1^- \to 5/2_1^-$		3.125
$7/2_1^- \to 3/2_1^-$		0.781
$21/2_1^+ \to 17/2_1^+$	0.139(10)	0.029

Table 3.4: Comparison of the magnetic dipole moments μ (in μ_N) and the electric quadrupole moments Q (in eb) obtained by the shell model (calc.) to the experimental data (expt.) for Pb isotopes. The experimental data are taken from Refs. [63–68].

	μ		Q	
^{206}Pb	expt.	calc.	expt.	calc.
2_1^+	<0.030	+0.056	+0.05(9)	+0.282
4_1^+		+0.413		+0.328
6_1^+		−0.263		+0.358
8_1^+		−1.156		+0.037
12_1^+	−1.795(22)	−1.763	0.51(2)	+0.468
7_1^-	−0.152(3)	−0.637	0.33(5)	+0.304
6_1^-	+0.8(4)	−1.217		+0.294
^{204}Pb	expt.	calc.	expt.	calc.
2_1^+	<0.02	+0.043	+0.23(9)	−0.052
4_1^+	+0.224(3)	+0.210	0.44(2)	+0.462
6_1^+		+0.691		+0.381
8_1^+		−1.154		+0.037
^{205}Pb	expt.	calc.	expt.	calc.
$1/2_1^-$		+0.319		
$3/2_1^-$		−0.665		+0.134
$5/2_1^-$	+0.7117(4)	+0.594	+0.226(37)	+0.206
$7/2_1^-$		+0.535		+0.148
$9/2_1^-$		+0.617		+0.423
$13/2_1^+$	−0.975(40)	−0.954	0.30(5)	+0.214
^{203}Pb	expt.	calc.	expt.	calc.
$1/2_1^-$		+0.319		
$3/2_1^-$		−0.780		+0.137
$5/2_1^-$	+0.6864(5)	+0.601	+0.095(52)	+0.066
$7/2_1^-$		+0.182		−0.073
$9/2_1^-$		+0.592		+0.021
$13/2_1^+$		−0.953		+0.165
$21/2_1^+$	−0.641(21)	−0.775		+0.715

states by the $E1$ transition, the 8^+_1 states might be located above the 10^+_1 states. However, the 8^+_1 states are calculated just below the 10^+_1 states. The 8^+_1 state is calculated at 3.701 MeV (3.311 MeV) for ^{206}Pb (^{204}Pb) in the present model.

Figure 3.3 shows the theoretical energy spectra for odd-mass Pb isotopes in comparison with the experimental data [63, 64, 66]. Good agreements with the experimental data are obtained, in particular for the low-lying states with negative parity. The $1/2^+_1$ state for ^{205}Pb is observed at 2.795 MeV. The theoretical $1/2^+_1$ state is calculated at 4.492 MeV in the present model. The experimental $1/2^+_1$ state is seemingly made by core excitations. The configuration is inferred as the 3^-_1 state of the even-even core ^{206}Pb coupled with the neutron $1f_{5/2}$ single-particle state: $(3^-_{\rm core} \otimes \nu f^{-1}_{5/2})$. The $3/2^+$, $5/2^+$, $\cdots$, and $11/2^+$ states with the same configuration are not confirmed in experiment.

Calculated results of the $B(E2)$ values, magnetic moments, and quadrupole moments for Pb isotopes are given in Tables 3.3 and 3.4 in comparison with the experimental data [63–68]. Theoretical calculations reproduce the experimental data very well on the whole. Small experimental $B(E2)$ values in ^{205}Pb are not reproduced well. For example, the experimental $B(E2; (21/2^+_1) \to 17/2^+_1)$ value is 0.01694(5) W.u., while the theoretical one is 3.160 W.u. In theory, the $17/2^+_1$ state consists of the $[\nu(f_{5/2})^2_{2^+} i_{13/2}]$ configuration and the $21/2^+_1$ state has the $[\nu(f_{5/2})^2_{4^+} i_{13/2}]$ configuration. This is why the theoretical $B(E2; 21/2^+_1 \to 17/2^+_1)$ value is large. The experimental spin-parity confirmation of the $(21/2^+_1)$ state might be required.

In ^{206}Pb, the sign of the magnetic moment of the 6^-_1 state is positive and that of the 7^-_1 state is negative in experiment. The signs of these values are negative in the present calculation. Both the 6^-_1 and 7^-_1 states consist of the $(\nu p^{-1}_{1/2} i^{-1}_{13/2})$ configuration and both states should have the same sign in theory. The magnetic moments of the 6^-_1 and 7^-_1 states were also calculated in Ref. [53] using the shell model and signs of both magnetic moments are also negative. Their results are consistent with ours.

3.3.2 Bi isotopes

Here $^{204-208}$Bi isotopes are discussed. Figure 3.4 shows the theoretical energy spectra for odd-mass Bi isotopes in comparison with the experimental data [63, 66, 69]. Theoretical calculations reproduce the experimental data well on the whole. In these nuclei, large differences between experiment and theory are seen in energies of the $1/2^+_1$ and $3/2^+_1$ states. It was inferred that the $1/2^+_1$ state is attributed to the $(\pi h^2_{9/2} s^{-1}_{1/2})$ configuration in these nuclei [70]. Here the proton $2s_{1/2}$ hole orbital below the magic number 82 is not included in the present framework. It was also mentioned that the $3/2^+_1$ state for ^{207}Bi mainly consists of the $(\nu p^{-2}_{1/2} \pi h^2_{9/2} d^{-1}_{3/2})$ configuration with small amount of the $(\nu p^{-2}_{1/2} \pi h_{9/2} \otimes 3^-)$ configuration [63, 71]. Likewise, the proton hole in the $1d_{3/2}$ orbital below the magic number 82 is not included in the present framework.

Figure 3.5 shows the theoretical energy spectra for doubly-odd Bi isotopes in comparison with the experimental data [5, 47, 63, 65, 67]. In ^{208}Bi, which is a one-neutron-hole and one-proton-particle system, energies of low-lying states below 1.5 MeV are well reproduced. The 12^+_2, 13^+_2 states and states with spin over 14 (irrespective of its parity) are beyond the present framework. The 12^+_1 and 13^+_1 states, which consist of the $(\nu i^{-1}_{13/2} \pi i_{13/2})$ configuration, are well reproduced in the present model.

In ^{208}Bi, the 2^-_1, 3^-_1, $\cdots$, and 11^-_1 states are members of the $(\nu i^{-1}_{13/2} \pi h_{9/2})$ configuration. The observed 2^-_1 and 11^-_1 states are higher than other members. However, the theoretical

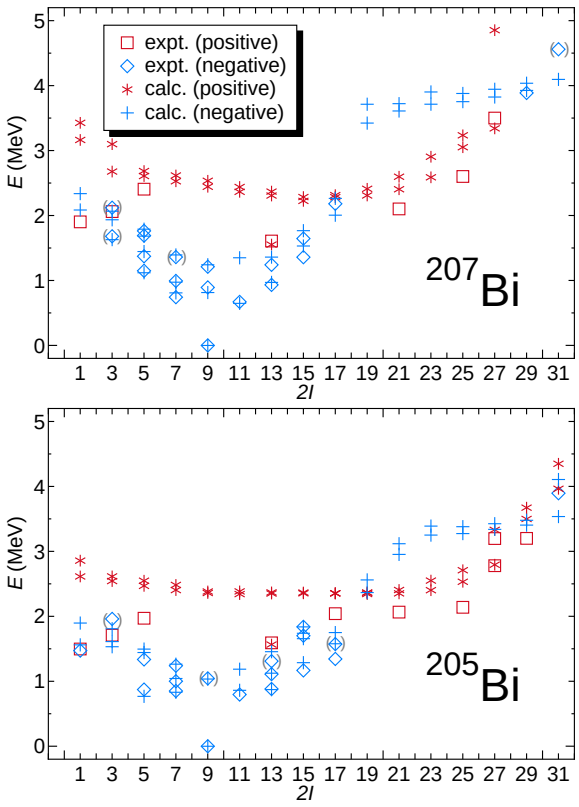

Figure 3.4: Same as fig. 3.2, but for odd-mass Bi isotopes. The experimental data are taken from Refs. [63, 66, 69].

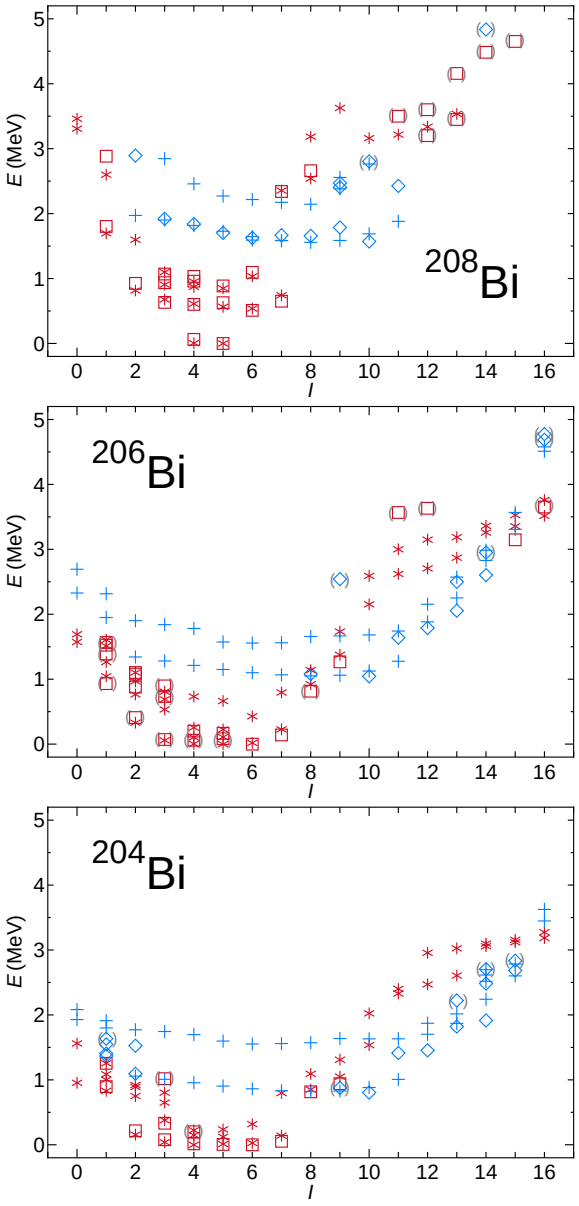

Figure 3.5: Same as fig. 3.2, but for doubly-odd Bi isotopes. The experimental data are taken from Refs. [5, 47, 63, 65, 67].

Table 3.5: Same as table 3.3, but for Bi isotopes. The experimental data are taken from Refs. [5, 63, 65–67, 69].

	$B(E2)$	
^{207}Bi	expt.	calc.
$11/2_1^- \to 9/2_1^-$		6.099
$7/2_1^- \to 9/2_1^-$		1.040
$7/2_1^- \to 11/2_1^-$		0.432
^{205}Bi	expt.	calc.
$11/2_1^- \to 9/2_1^-$		6.995
$7/2_1^- \to 9/2_1^-$		1.266
$7/2_1^- \to 11/2_1^-$		0.016
$25/2_1^+ \to 21/2_1^+$	0.58(8)	0.526
^{208}Bi	expt.	calc.
$6_1^+ \to 4_1^+$	0.10(3)	0.169
$6_1^+ \to 5_1^+$	1.5(5)	2.013
$7_1^+ \to 5_1^+$	$\leq$0.017	0.848
$4_1^+ \to 5_1^+$		0.576
^{206}Bi	expt.	calc.
$4_1^+ \to 6_1^+$	0.0180(6)	0.025
$3_1^+ \to 4_1^+$		4.159
$5_1^+ \to 4_1^+$		3.013
$5_1^+ \to 6_1^+$		0.017
^{204}Bi	expt.	calc.
$5_1^+ \to 6_1^+$		4.155
$4_1^+ \to 6_1^+$		0.693
$4_1^+ \to 5_1^+$		4.263

calculation fails in reproducing this situation. This problem was also seen in the previous calculation for ^{132}Sb [8]. This nucleus is a one-neutron-hole and one-proton-particle system assuming the ^{132}Sn core, which is a similar system as ^{208}Bi. In ^{132}Sb, the 2_1^-, 3_1^-, $\cdots$, and 9_1^- states with the $(\nu h_{11/2}^{-1} \pi g_{7/2})$ configuration are seen in the low-lying states and the 2_1^- and 9_1^- states are located at high energies than other members. A shell-model calculation was performed for ^{132}Sb in the same framework. It was found that a hexadecapole interaction among alike nucleons is important to reproduce these negative parity states [8]. Through the argument in the above, a hexadecapole interaction between neutrons and protons would be necessary to well reproduce energies of the 2_1^- and 11_1^- states in ^{208}Bi. The detailed discussion about the hexadecapole interaction is performed in Sec. 3.4.6.

Similar to ^{208}Bi, the theoretical 11_1^- states in ^{206}Bi and ^{204}Bi are calculated lower than the experimental 11_1^- states. Theoretical 11_1^- states in ^{206}Bi and ^{204}Bi would be reproduced at observed positions of the experimental 11_1^- states by introducing such a hexadecapole interaction. In fact, a shell-model calculation [47] was carried out for ^{206}Bi using the interaction deduced from the Hamada-Johnston potential and the 11_1^- state was

Table 3.6: Same as table 3.3, but for Bi isotopes. The experimental data are taken from Refs. [5, 63, 65–67, 69].

	μ		Q	
^{207}Bi	expt.	calc.	expt.	calc.
$7/2_1^-$		+3.648		−0.592
$9/2_1^-$	+4.0915(9)	+3.669	−0.545(38)	−0.717
$11/2_1^-$		+3.477		−0.434
$13/2_1^-$		+3.742		−0.224
$21/2_1^+$	+3.41(6)	+2.494	0.044(8)	−0.056
^{205}Bi	expt.	calc.	expt.	calc.
$7/2_1^-$		+3.997		−0.638
$9/2_1^-$	+4.065(7)	+3.666	−0.585(43)	−0.763
$11/2_1^-$		+3.345		−0.497
$13/2_1^-$		+3.726		−0.777
$21/2_1^+$	2.70(4)	+1.797		+0.288
$25/2_1^+$	3.21(5)	+2.713		−0.140
^{208}Bi	expt.	calc.	expt.	calc.
4_1^+		+3.712		−0.508
5_1^+	+4.578(13)	+3.819	−0.51(7)	−0.541
6_1^+		+3.916		−0.313
10_1^-	2.672(14)	+2.379		−0.006
^{206}Bi	expt.	calc.	expt.	calc.
4_1^+		+3.280		−0.512
5_1^+		+3.653		−0.561
6_1^+	+4.361(8)	+3.784	−0.39(4)	−0.664
10_1^-	2.644(14)	+2.259	0.049(9)	−0.225
^{204}Bi	expt.	calc.	expt.	calc.
4_1^+		+3.763		−0.651
5_1^+		+3.592		−0.603
6_1^+	+4.322(15)	+3.167	−0.49(15)	−0.511
10_1^-	2.36(23)	+2.269	0.063(12)	−0.298

calculated at 1.716 MeV (1.639 MeV in experiment).

Calculated results of the $B(E2)$ values, magnetic moments, and quadrupole moments for Bi isotopes are given in Tables 3.5 and 3.6 in comparison with the experimental data [5, 63, 65–67, 69]. The small $B(E2; 4_1^+ \rightarrow 6_1^+)$ value in ^{206}Bi is well reproduced. The quadrupole moments of the 10_1^- states for ^{206}Bi and ^{204}Bi are small in experiment (0.049(9) eb for ^{206}Bi and 0.063(12) eb for ^{204}Bi). However, the present results fail in reproducing these experimental data (-0.225 eb for ^{206}Bi and -0.299 eb for ^{204}Bi). It is, however, noted that the magnetic moments of the same states are well reproduced. This phenomenon is discussed in Sec. 3.4.2.

3.3.3 Po isotopes

Here $^{205-210}$Po isotopes are discussed. Figure 3.6 shows the theoretical energy spectra for even-even Po isotopes in comparison with the experimental data [5, 63, 67, 73].

^{210}Po is a system with two valence protons. The energy gap between the 8_1^+ and 10_1^+ states is large in this nucleus. This is because the 8_1^+ state is constructed by two protons in the $0h_{9/2}$ orbital. The 0_1^+, 2_1^+, 4_1^+, and 6_1^+ states are also constructed by the $(\pi h_{9/2}^2)$ configuration. In contrast, two protons need to occupy the $0i_{13/2}$ orbital to make states over 10^+. The 1_1^+, 2_2^+, 3_1^+, 4_2^+, 5_1^+, 6_2^+, 7_1^+, and 8_2^+ states are members of the $(\pi h_{9/2} f_{7/2})$ configuration.

In ^{210}Po, the 11_1^- state consists of the $(\pi h_{9/2} i_{13/2})$ configuration. The 11_2^- state and states with spin greater than 13 are beyond the present framework. Except for these states, theoretical calculations reproduce the experimental data well for all the nuclei.

Figure 3.7 shows the theoretical energy spectra for odd-mass Po isotopes in comparison with the experimental data [63, 66, 69, 72]. In ^{209}Po, a large energy difference between the calculated $21/2_1^-$ and $23/2_1^-$ states is seen. It is noted that no experimentally confirmed $23/2_1^-$ state is observed. The $21/2_1^-$ state mainly consists of the $(\nu f_{5/2}^{-1} \pi h_{9/2}^2)$ configuration. In contrast, the $23/2_1^-$ state mainly consists of the $(\nu f_{7/2}^{-1} \pi h_{9/2}^2)$ configuration. This difference of the two configurations causes the large energy gap between the $21/2_1^-$ and $23/2_1^-$ states.

The $19/2_1^-$ states are spin-gap isomers with long half-lives of 2.79(8) s and 57.4(9) ms for ^{207}Po and ^{205}Po, respectively [63]. These states mainly decay to the $13/2_1^+$ states by the $E3$ transition. From this fact, the $15/2^-$ and $17/2^-$ states which can be connected to the $19/2_1^-$ state by the $E2$ or $M1$ transitions, should be located above the $19/2_1^-$ state. In theory, however, the $15/2^-$ and $17/2^-$ states are calculated slightly lower than the $19/2_1^-$ states in both nuclei.

The calculated $B(E2)$ values, magnetic moments, and quadrupole moments for Po isotopes are given in Tables 3.7 and 3.8 in comparison with the experimental data [5, 63, 66, 67, 69, 72, 73]. In ^{210}Po, the $E2$ transition rates among the yrast states are successfully reproduced except for the $B(E2; 2_1^+ \rightarrow 0_1^+)$ value. The experimental $B(E2; 2_1^+ \rightarrow 0_1^+)$ value is 0.56(12) W.u. In contrast the theoretical $B(E2; 2_1^+ \rightarrow 0_1^+)$ value is 4.12 W.u. This $B(E2)$ value was also calculated using the shell model and was given as 3.55 W.u. [54, 55].

The experimental magnetic moments and quadrupole moments are well reproduced by the present calculation. Only one disagreement is seen in the magnetic moment of the $1/2_1^-$ state for ^{209}Po, which is calculated almost half the value of the experimental value.

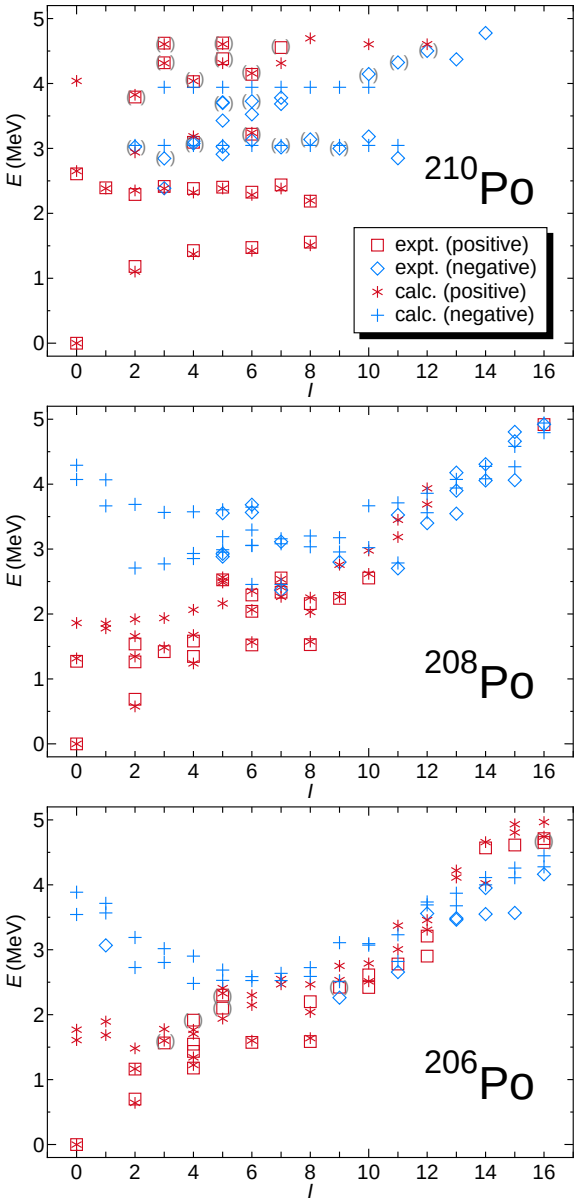

Figure 3.6: Same as fig. 3.2, but for even-even Po isotopes. The experimental data are taken from Refs. [5, 63, 67, 73].

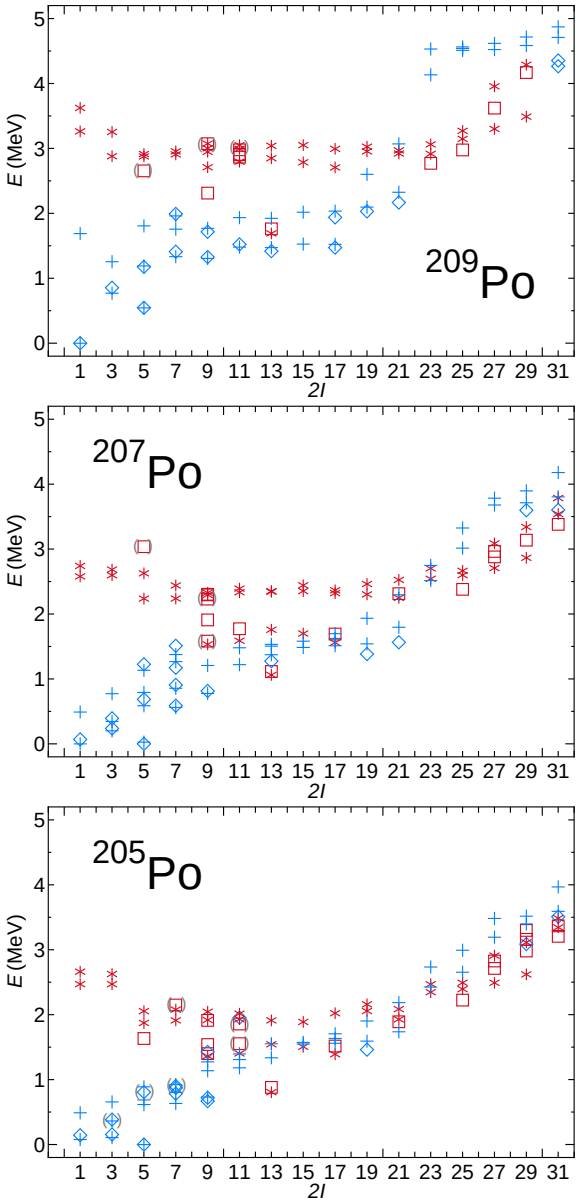

Figure 3.7: Same as fig. 3.2, but for odd-mass Po isotopes. The experimental data are taken from Refs. [63, 66, 69, 72].

Table 3.7: Same as table 3.3, but for Po isotopes. The experimental data are taken from Refs. [5, 63, 66, 67, 69, 72, 73].

	$B(E2)$	
^{210}Po	expt.	calc.
$2_1^+ \to 0_1^+$	0.56(12)	4.123
$4_1^+ \to 2_1^+$	4.46(18)	4.453
$6_1^+ \to 4_1^+$	3.05(9)	3.028
$8_1^+ \to 6_1^+$	1.12(4)	1.055
$10_1^+ \to 8_1^+$		<0.001
^{208}Po	expt.	calc.
$2_1^+ \to 0_1^+$		8.890
$4_1^+ \to 2_1^+$		11.216
$6_1^+ \to 4_1^+$	5.6(4)	6.807
$8_1^+ \to 6_1^+$	6.4(5)	1.684
$10_1^+ \to 8_1^+$		2.206
^{206}Po	expt.	calc.
$2_1^+ \to 0_1^+$		12.997
$4_1^+ \to 2_1^+$		11.151
$6_1^+ \to 4_1^+$		5.569
$8_1^+ \to 6_1^+$	2.45(16)	3.829
$10_1^+ \to 8_1^+$		5.121
^{209}Po	expt.	calc.
$5/2_1^- \to 1/2_1^-$	2.2(7)	3.691
$3/2_1^- \to 1/2_1^-$		5.206
$3/2_1^- \to 5/2_1^-$		1.298
$13/2_1^- \to 9/2_1^-$	4.37(10)	4.538
$17/2_1^- \to 13/2_1^-$	1.43(5)	1.376
$11/2_1^- \to 7/2_1^-$	13(5)	4.344
$11/2_1^- \to 9/2_1^-$	15(12)	0.172
^{207}Po	expt.	calc.
$1/2_1^- \to 5/2_1^-$	0.60(3)	0.912
$3/2_1^- \to 5/2_1^-$		4.697
$3/2_1^- \to 1/2_1^-$		0.083
$7/2_1^- \to 5/2_1^-$		10.999
$7/2_1^- \to 3/2_1^-$		0.096
^{205}Po	expt.	calc.
$1/2_1^- \to 5/2_1^-$	0.16(3)	3.586
$3/2_1^- \to 5/2_1^-$		2.048
$3/2_1^- \to 1/2_1^-$		0.196
$7/2_1^- \to 5/2_1^-$		11.022
$25/2_1^+ \to 21/2_1^+$	0.9(3)	0.707

Table 3.8: Same as table 3.4, but for Po isotopes. The experimental data are taken from Refs. [5, 63, 66, 67, 69, 72, 73].

	μ		Q	
^{210}Po	expt.	calc.	expt.	calc.
2_1^+		+1.718		+0.186
4_1^+		+3.368		+0.134
6_1^+	5.48(5)	+5.038		−0.141
8_1^+	+7.13(5)	+6.734	−0.552(20)	−0.551
11_1^-	+12.20(9)	+11.163	−0.86(11)	−0.965
^{208}Po	expt.	calc.	expt.	calc.
2_1^+		+0.521		+0.458
4_1^+		+2.398		+0.435
6_1^+	+5.3(6)	+4.780		−0.087
8_1^+	+7.37(5)	+6.617	0.90(4)	−0.926
^{206}Po	expt.	calc.	expt.	calc.
2_1^+		+0.636		+0.203
4_1^+		+1.364		+0.617
6_1^+		+4.760		−0.256
8_1^+	+7.34(7)	+6.541	1.02(4)	−0.974
^{209}Po	expt.	calc.	expt.	calc.
$1/2_1^-$	0.68(8)	+0.315		
$3/2_1^-$		−0.342		+0.223
$5/2_1^-$		+0.901		+0.326
$13/2_1^-$	6.13(9)	+5.243	0.126(5)	−0.130
$17/2_1^-$	7.75(5)	+6.718	0.659(7)	−0.703
$13/2_1^+$		−0.931		+0.529
^{207}Po	expt.	calc.	expt.	calc.
$1/2_1^-$		+0.315		
$3/2_1^-$		−0.529		+0.124
$5/2_1^-$	0.79(6)	+0.643		+0.357
$13/2_1^+$	−0.910(14)	−0.931		+0.577
$25/2_1^+$	5.41(4)	+4.921		−0.400
^{205}Po	expt.	calc.	expt.	calc.
$1/2_1^-$		+0.308		
$3/2_1^-$		−0.624		+0.274
$5/2_1^-$	+0.76(6)	+0.633		+0.189
$13/2_1^+$	−0.95(5)	−0.935		+0.506

3.3.4 At isotopes

Here $^{206-211}$At isotopes are discussed. Figure 3.8 shows the theoretical energy spectra for odd-mass At isotopes in comparison with the experimental data [63, 69, 72, 74]. In these nuclei, low-lying negative parity states are excellently reproduced.

It is noticed from Fig. 3.8 that the energy of the $19/2^-_1$ state is higher compared to other first negative parity states in these nuclei. For example, in ^{211}At, the $17/2^-_1$ and $21/2^-_1$ states are calculated at 1.356 and 1.496 MeV, respectively. In contrast, the $19/2^-_1$ state is calculated at 2.032 MeV. The $17/2^-_1$ and $21/2^-_1$ states consist of the $(\pi h^3_{9/2})$ configuration. In contrast the $19/2^-_1$ state consists of the $(\pi h^2_{9/2} f_{7/2})$ configuration. Since the single-particle energy of the $1f_{7/2}$ orbital is higher than that of the $0h_{9/2}$ orbital, the energy of the $19/2^-_1$ state is higher compared to the $17/2^-_1$ and $21/2^-_1$ states. It should be noted that the $19/2^-$ state cannot be constructed by the $(\pi h^3_{9/2})$ configuration.

The $29/2^+_1$ state at 2.429 MeV in ^{209}At is an isomer with a half-life of 0.916(10) μs [63]. This state is a spin-gap isomer, which decays to the $23/2^-_1$ state at 1.852 MeV by the $E3$ transition. The $29/2^+_1$ state mainly consists of the $[\pi(h^2_{9/2})_{8^+}\ i_{13/2}]$ configuration for the proton part, while two neutrons mainly couple to spin zero. In this configuration, the maximum spin is 29/2. As one of our empirical rules, using the effective interactions among like nucleons adopted in the present framework the maximum-spin state among members with one specific configuration is likely to get lower in energy than other members with the same configuration. Accordingly, it is likely that the state which has the maximum spin among those states with the same configuration becomes a spin-gap isomer. In this case, the maximum spin of the $[\pi(h^2_{9/2})_{8^+}\ i_{13/2}]$ configuration is 29/2. Thus this state gets lower in energy than other states with the same members and becomes a spin-gap isomer. This isomer was also analyzed in Ref. [75] and they suggested the same configuration.

Figure 3.9 shows the theoretical energy spectra for doubly-odd At isotopes in comparison with the experimental data [5, 63, 67, 73]. In ^{206}At, relative energies between the ground state and the 7^+_1 state and the states above are not known in experiment. In Fig. 3.9, the excitation energy of the 7^+_1 state is assumed as 0.09 MeV. Almost all states observed in ^{210}At are well reproduced in theory. Furthermore, low-lying positive parity states, which are densely located below 0.2 MeV, are well reproduced in ^{208}At.

The 15^-_1 state at 2.549 MeV in ^{210}At is a spin-gap isomer. The half-life of this state is 0.482(6) μs and this state decays to the 12^+ states by the $E3$ transition [63]. This state mainly consists of the $[\nu p^{-1}_{1/2}\pi(h^2_{9/2})_{8^+}\ i_{13/2}]$ configuration and spin 15 is the maximum spin made by this configuration. The 13^-_1 and 14^-_1 states, which can be connected to the 15^-_1 state by the $E2$ or $M1$ transitions, are located slightly higher than the 15^-_1 state and the theoretical calculation reproduces this experimental situation. The same configuration was also proposed in Ref. [42].

The 10^-_1 state (47.8(10) ns) and 16^-_1 state (1.5(2) μs) in ^{208}At and the 10^-_1state (410(80) ns) in ^{206}At are also isomers [63]. These states decay to lower states by $E3$ or $E1$ transitions. In theory, states which can be connected to these isomeric states by the $E2$ or $M1$ transitions are calculated almost degenerately in energy with the isomeric states. Typical energy gaps are around 0.05 MeV.

Calculated results of the $B(E2)$ values, magnetic moments, and quadrupole moments for At isotopes are given in Tables 3.9 and 3.10 in comparison with the experimental data [5, 63, 67, 69, 72–74]. The experimental data are well reproduced on the whole. In

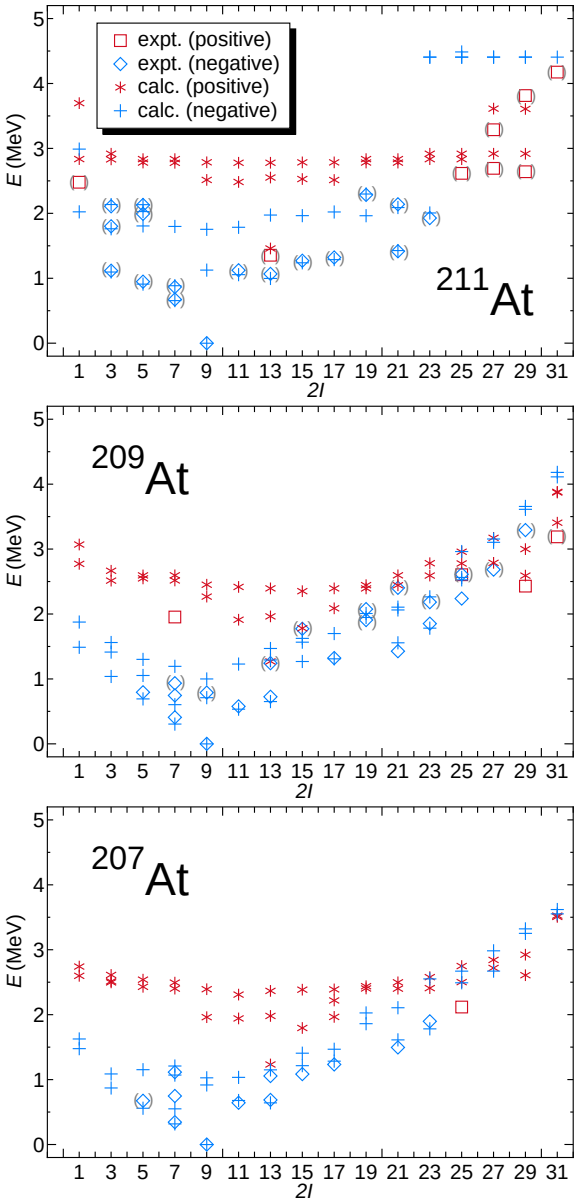

Figure 3.8: Same as fig. 3.2, but for odd-mass At isotopes. The experimental data are taken from Refs. [63, 69, 72, 74].

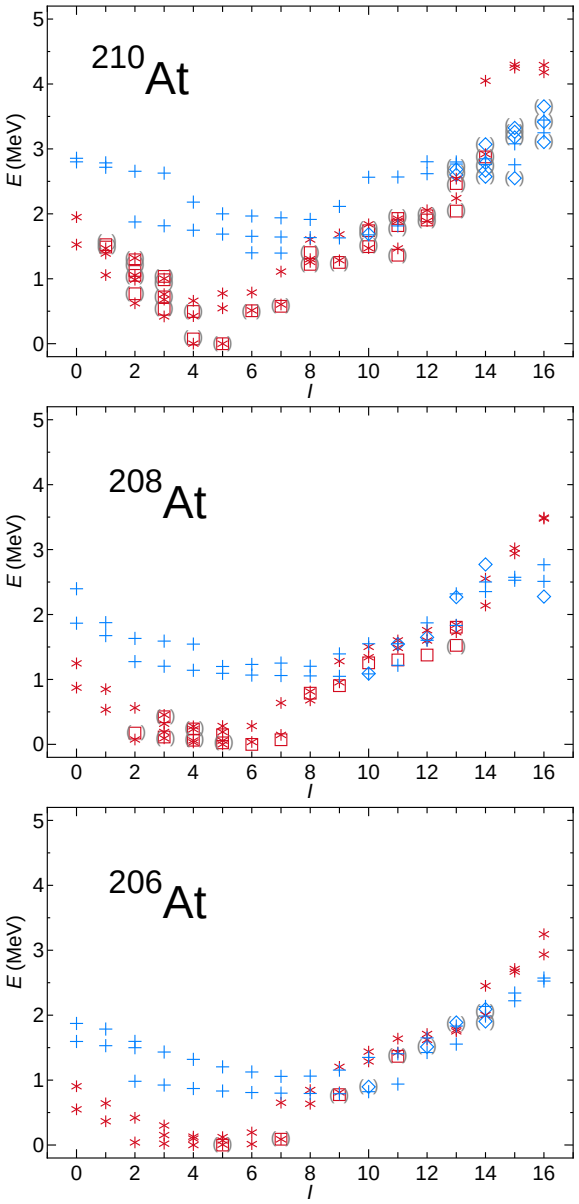

Figure 3.9: Same as fig. 3.2, but for doubly-odd At isotopes. The experimental data are taken from Refs. [5, 63, 67, 73].

Table 3.9: Same as table 3.3, but for At isotopes. The experimental data are taken from Refs. [5, 63, 67, 69, 72–74].

	$B(E2)$	
^{211}At	expt.	calc.
$13/2_1^- \to 9/2_1^-$	>0.039	4.298
$3/2_1^- \to 5/2_1^-$	12.8(14)	9.801
$3/2_1^- \to 7/2_1^-$	0.40(4)	0.874
$3/2_1^- \to 7/2_2^-$	1.78(18)	0.828
$15/2_1^- \to 11/2_1^-$	1.7(3)	2.271
$15/2_1^- \to 13/2_1^-$	0.37(8)	0.598
$17/2_1^- \to 13/2_1^-$	>84	4.108
$21/2_1^- \to 17/2_1^-$	2.66(10)	2.119
$29/2_1^+ \to 25/2_1^+$	1.8(3)	1.054
^{209}At	expt.	calc.
$7/2_1^- \to 9/2_1^-$		13.992
$11/2_1^- \to 7/2_1^-$		3.226
$11/2_1^- \to 9/2_1^-$		10.030
$21/2_1^- \to 17/2_1^-$	3.21(10)	3.545
^{207}At	expt.	calc.
$7/2_1^- \to 9/2_1^-$		17.889
$11/2_1^- \to 7/2_1^-$		1.960
$11/2_1^- \to 9/2_1^-$		13.164
^{210}At	expt.	calc.
$4_1^+ \to 5_1^+$		0.131
$6_1^+ \to 5_1^+$		3.226
$6_1^+ \to 4_1^+$		0.706
^{208}At	expt.	calc.
$5_1^+ \to 6_1^+$		2.129
$4_1^+ \to 6_1^+$		0.246
$4_1^+ \to 5_1^+$		2.913
^{206}At	expt.	calc.
$7_1^+ \to 5_1^+$		0.171
$9_1^+ \to 7_1^+$		13.618
$11_1^+ \to 9_1^+$		12.428

Table 3.10: Same as table 3.4, but for At isotopes. The experimental data are taken from Refs. [5, 63, 67, 69, 72–74].

	μ		Q	
^{211}At	expt.	calc.	expt.	calc.
$5/2_1^-$		+2.069		−0.007
$7/2_1^-$		+3.710		−0.475
$9/2_1^-$		+3.776		−0.211
$21/2_1^-$	+9.56(9)	+8.810	0.53(5)	−0.479
$29/2_1^+$	+15.31(13)	+14.129	1.00(5)	−1.092
^{209}At	expt.	calc.	expt.	calc.
$5/2_1^-$		+2.699		−0.014
$7/2_1^-$		+3.047		−0.776
$9/2_1^-$		+3.711		−0.372
$21/2_1^-$	+9.9(2)	+8.667	0.78(8)	−0.815
$29/2_1^+$	15.38(14)	+13.981	1.50(15)	−1.697
^{207}At	expt.	calc.	expt.	calc.
$5/2_1^-$		+2.629		−0.045
$7/2_1^-$		+3.011		−0.797
$9/2_1^-$		+3.680		−0.453
$25/2_1^+$	+3.75(13)	+2.870		+0.631
^{210}At	expt.	calc.	expt.	calc.
4_1^+		+3.543		−0.263
5_1^+		+3.980		−0.279
6_1^+		+4.107		−0.029
11_1^+	+9.79(3)	+8.832	0.65(8)	−0.610
19_1^+	13.26(13)	+12.746	2.20(25)	−0.810
15_1^-	+15.675(17)	+13.864	1.22(12)	−1.364
^{208}At	expt.	calc.	expt.	calc.
4_1^+		+3.027		−0.343
5_1^+		+3.456		−0.310
6_1^+		+3.889		−0.173
10_1^-	+2.69(3)	+2.318		+0.351
16_1^-		+13.971	1.7(3)	−1.839
^{206}At	expt.	calc.	expt.	calc.
5_1^+		+3.448		−0.322
7_1^+		+4.286		−0.309
9_1^+		+5.092		−0.254
11_1^+		+7.379		−0.446

^{211}At, the large value of $B(E2; 3/2^-_1 \rightarrow 5/2^-_1)$ is well reproduced. The $B(E2; 3/2^-_1 \rightarrow 5/2^-_1)$ value is 32 times larger than the $B(E2; 3/2^-_1 \rightarrow 7/2^-_1)$ value. The $3/2^-_1$ and $5/2^-_1$ states consist of the $(\pi h^3_{9/2})$ configuration. In contrast, the $7/2^-_1$ state mainly consists of the $(\pi h^2_{9/2} f_{7/2})$ configuration. It is this difference of the configurations that appears in different magnitudes of the $B(E2; 3/2^-_1 \rightarrow 5/2^-_1)$ and $B(E2; 3/2^-_1 \rightarrow 7/2^-_1)$ values.

The experimental $B(E2; 3/2^-_1 \rightarrow 7/2^-_2)$ value is 4.5 times larger than the $B(E2; 3/2^-_1 \rightarrow 7/2^-_1)$ value in ^{211}At. However, theoretical results give almost the same values for both transition rates. It might be explained by the admixture of the states of the $7/2^-_1$ and $7/2^-_2$ states. Suppose that the original $7/2^-_1$ and $7/2^-_2$ states are admixed as follows:

$$\left|\widetilde{7/2^-_1}\right\rangle = \alpha \left|7/2^-_1\right\rangle + \sqrt{1-\alpha^2}\left|7/2^-_2\right\rangle, \tag{3.5}$$

$$\left|\widetilde{7/2^-_2}\right\rangle = \sqrt{1-\alpha^2}\left|7/2^-_1\right\rangle - \alpha \left|7/2^-_2\right\rangle. \tag{3.6}$$

Here, $|\ \rangle$ represents an eigenstate and $|\widetilde{\ }\rangle$ represents an admixed state. If $\alpha = 0.95$ is assumed, the revised transition rates by the admixed states are changed as $B(E2; 3/2^-_1 \rightarrow \widetilde{7/2^-_1})$=0.36 W.u. (0.40(4) W.u. in experiment) and $B(E2; \widetilde{3/2^-_1} \rightarrow \widetilde{7/2^-_2})$=1.34 W.u. (1.78(18) W.u. in experiment).

The experimental magnetic moments and quadrupole moments are excellently reproduced by the calculation. This calculation will be helpful to determine signs of these moments.

3.3.5 Rn isotopes

Here $^{207-212}$Rn isotopes are discussed. Figure 3.10 shows the theoretical energy spectra for even-even Rn isotopes in comparison with the experimental data [5,43,63,73,76]. Just like ^{206}At, the relative positions between the ground state and many excited states are not known in ^{210}Rn. The lowest state (the (8^+_1) state) of these excited states is observed at 1.665+x MeV. In this figure, this state is shown with an assumption of $x = 0.096$ MeV.

The theoretical energy levels in ^{212}Rn as a whole are slightly lower than the experimental ones, but one-to-one correspondence of energy levels between experiment and theory is well established in these nuclei. One of the features in even-even Rn nuclei is seen in the small energy gap between the 6^+_1 and 8^+_1 states. Due to these small energy gaps, the 8^+_1 states are isomers with half-lives of 0.91(3) μs, 644(40) ns, and 487(12) ns for ^{212}Rn, ^{210}Rn, and ^{208}Rn, respectively [5, 73, 76]. Theoretical calculations well reproduce the feature of these small energy gaps.

Figure 3.11 shows the theoretical energy spectra for odd-mass Rn isotopes in comparison with the experimental data [63, 69, 72, 74]. The relative positions between the ground state and many excited states are not known in ^{211}Rn. The lowest state (the $(17/2^-_1)$ state) of these excited states is observed at 1.578+x MeV. In this figure, this state is shown with an assumption of $x = 0.050$ MeV. Low-lying negative parity states are excellently reproduced.

Calculated results of the $B(E2)$ values, magnetic moments, and quadrupole moments for Rn isotopes are given in Tables 3.11 and 3.12 in comparison with the experimental data [5, 63, 69, 72–74, 76]. Theoretical results reproduce small $B(E2; 14^+_1 \rightarrow 12^+_1)$ values for ^{212}Rn and ^{210}Rn. In ^{212}Rn, the 12^+_1 state consists of the $(\pi h^4_{9/2})$ configuration. In contrast, the 14^+_1 state consists of the $(\pi h^3_{9/2} f_{7/2})$ configuration. This difference of the

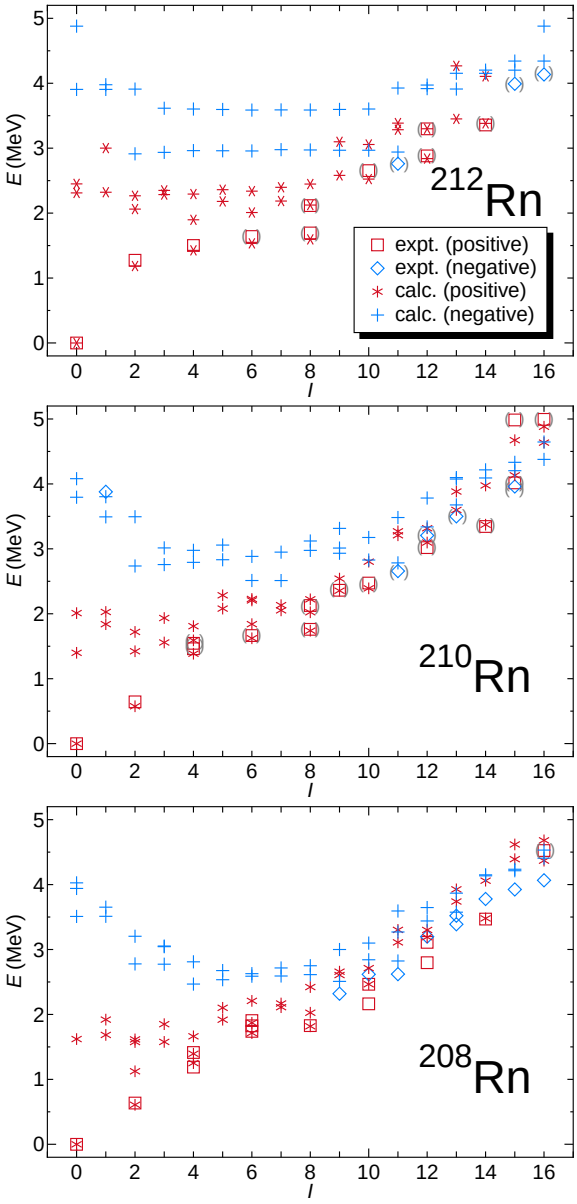

Figure 3.10: Same as fig. 3.2, but for even-even Rn isotopes. The experimental data are taken from Refs. [5, 43, 63, 73, 76].

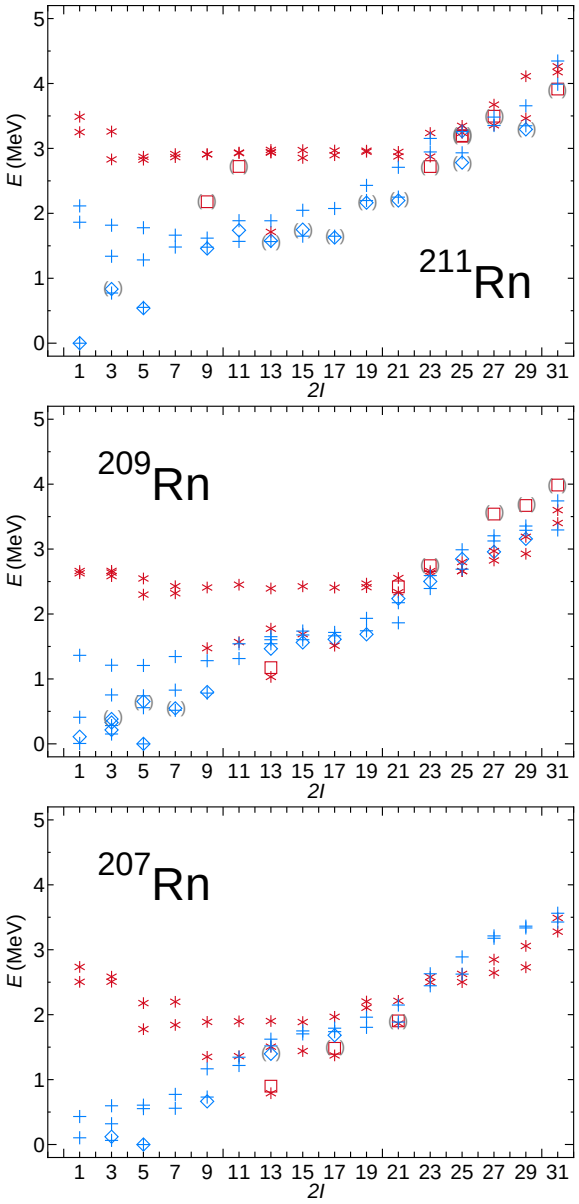

Figure 3.11: Same as fig. 3.2, but for odd-mass Rn isotopes. The experimental data are taken from Refs. [63, 69, 72, 74].

Table 3.11: Same as table 3.3, but for Rn isotopes. The experimental data are taken from Refs. [5, 63, 69, 72–74, 76].

	$B(E2)$	
^{212}Rn	expt.	calc.
$2_1^+ \to 0_1^+$		6.237
$4_1^+ \to 2_1^+$	1.04(4)	0.688
$6_1^+ \to 4_1^+$	0.40(5)	0.373
$8_1^+ \to 6_1^+$	0.115(6)	0.144
$10_1^+ \to 8_1^+$		3.950
$12_1^+ \to 10_1^+$	4.4(2)	2.966
$14_1^+ \to 12_1^+$	0.032(8)	0.0024
$14_1^+ \to 12_2^+$	<4	2.856
$17_1^- \to 15_1^-$	3.0(16)	2.111
^{210}Rn	expt.	calc.
$2_1^+ \to 0_1^+$		12.230
$4_1^+ \to 2_1^+$		18.353
$6_1^+ \to 4_1^+$	1.58(15)	1.337
$6_1^+ \to 4_2^+$	1.58(19)	2.631
$8_1^+ \to 6_1^+$		0.704
$14_1^+ \to 12_1^+$	0.0248(23)	0.001
^{208}Rn	expt.	calc.
$2_1^+ \to 0_1^+$		19.125
$4_1^+ \to 2_1^+$		10.300
$6_1^+ \to 4_1^+$		0.329
$8_1^+ \to 6_1^+$		1.417
^{211}Rn	expt.	calc.
$5/2_1^- \to 1/2_1^-$	>0.040	5.024
$21/2_1^- \to 17/2_1^-$	>0.030	4.867
$25/2_1^- \to 21/2_1^-$	>0.036	2.627
$29/2_1^- \to 25/2_1^-$	0.073(17)	0.001
$29/2_1^- \to 25/2_2^-$	1.9(6)	1.567
$31/2_1^+ \to 27/2_1^+$	>0.0077	3.340
^{209}Rn	expt.	calc.
$1/2_1^- \to 5/2_1^-$		1.210
$3/2_1^- \to 5/2_1^-$		6.837
$29/2_1^- \to 27/2_1^-$	0.66 (15)	0.107
^{207}Rn	expt.	calc.
$3/2_1^- \to 5/2_1^-$		5.024
$9/2_1^- \to 5/2_1^-$		17.633

Table 3.12: Same as table 3.4, but for Rn isotopes. The experimental data are taken from Refs. [5, 63, 69, 72–74, 76].

	μ		Q	
^{212}Rn	expt.	calc.	10pt	calc.
2_1^+		+1.714		+0.002
4_1^+	4.0(2)	+3.369		+0.040
6_1^+	5.45(5)	+5.058		−0.020
8_1^+	+7.15(2)	+6.726		−0.193
14_1^+	15.0(4)	+13.207		−0.881
17_1^-	17.9(2)	+16.205		−1.021
^{210}Rn	expt.	calc.	expt.	calc.
2_1^+		+0.470		+0.508
4_1^+		+1.603		+0.504
6_1^+		+4.937		−0.043
8_1^+	7.184(56)	+6.611	0.31(4)	−0.300
14_1^+	14.92(10)	+13.060		−1.402
11_1^-	12.16(11)	+11.014		−1.343
17_1^-	17.88(9)	+16.088	0.86(10)	−1.655
^{208}Rn	expt.	calc.	expt.	calc.
2_1^+		+0.604		+0.107
4_1^+		+0.569		+0.948
6_1^+		+4.908		−0.118
8_1^+	6.98(8)	+6.529	0.39(5)	−0.426
10_1^-	10.77(10)	+10.136		−1.843
^{211}Rn	expt.	calc.	expt.	calc.
$1/2_1^-$	+0.601(7)	+0.315		
$3/2_1^-$		−0.451		+0.229
$5/2_1^-$		+0.903		+0.373
$17/2_1^-$	+7.75(8)	+6.940	0.18(2)	−0.240
$13/2_1^+$		−0.919		+0.675
^{209}Rn	expt.	calc.	expt.	calc.
$1/2_1^-$		+0.317		
$3/2_1^-$		−0.513		+0.154
$5/2_1^-$	0.8388(4)	+0.661	+0.31(3)	+0.458
$13/2_1^+$		−0.915		+0.831
^{207}Rn	expt.	calc.	expt.	calc.
$1/2_1^-$		+0.309		
$3/2_1^-$		−0.553		+0.367
$5/2_1^-$	+0.816(9)	+0.638	+0.220(22)	+0.285
$13/2_1^+$	−0.903(3)	−0.917		+0.815

configurations makes the $B(E2; 14_1^+ \to 12_1^+)$ value small. The 12_2^+ state consists of the $(\pi h_{9/2}^3 f_{7/2})$ configuration, and the $B(E2; 14_1^+ \to 12_2^+)$ value becomes large compared to the $B(E2; 14_1^+ \to 12_1^+)$ value. In ^{212}Rn, due to this small $B(E2)$ value, the 14_1^+ state is an isomer with a half-life of 7.4(8) ns [63]. Just like ^{212}Rn, the 14_1^+ state in ^{210}Rn (^{208}Rn) is an isomer with a half-life of 76(7) ns (3.5(7) ns) [63].

The experimental magnetic moments and quadrupole moments are well reproduced by the calculation. The largest difference between the experimental value and the theoretical one is seen in the quadrupole moment of the 17_1^- state for ^{210}Rn. The theoretical value is calculated 1.9 times lager than the experimental one.

3.3.6 Fr isotopes

Here $^{208-213}$Fr isotopes are discussed. Figure 3.12 shows the theoretical energy spectra for odd-mass Fr isotopes in comparison with the experimental data [63, 72, 74, 77]. Negative parity yrast states are well reproduced in all the nuclei. Spin and parity of the ground state is $9/2^-$ for these odd-mass nuclei, which is reproduced in the calculation. Spin of the lowest positive parity states in these nuclei is 13/2, and energies of these states are calculated at 1.280, 1.101, and 1.166 MeV for ^{213}Fr, ^{211}Fr, and ^{209}Fr, respectively. These states mainly consist of the $[\pi(h_{9/2}f_{7/2})^4 i_{13/2}]$ configuration for the proton part.

The $29/2_1^+$ state in ^{213}Fr is a spin-gap isomer with a half-life of 238(6) ns [63]. This state decays to the $23/2_1^-$ state by the $E3$ transition. The $29/2_1^+$ state mainly consists of the $(\pi h_{9/2}^4 i_{13/2})$ configuration, where two of four protons in the $0h_{9/2}$ orbital are coupled to spin eight and the rest two protons are coupled to spin zero. The last proton stays in the $0i_{13/2}$ orbital. The maximum spin of this configuration is 29/2. This isomer was also analyzed in Ref. [78] and they suggested the same configuration.

Figure 3.13 shows the theoretical energy spectra for doubly-odd Fr isotopes in comparison with the experimental data [5, 46, 63, 73, 76]. There are a few observed states in these nuclei. In ^{208}Fr, spin and parity of the ground state is 7^+. However, the theoretical ground state becomes the 5^+, although the 2_1^+, 3_1^+, $\cdots$, 7_1^+ states are degenerately predicted around the ground state.

In ^{212}Fr, which is a system of one-neutron and five-protons, the lowest states are the 4^+ and 5^+ states. These two states consist of the $(\nu p_{1/2}^{-1} \pi h_{9/2})$ configuration coupled with the 0_1^+ state of the even-even core: ^{212}Rn. In contrast, in ^{208}Fr, which is a system of three neutrons and five protons, lowest states (2_1^+, 3_1^+, $\cdots$, 7_1^+) are members of the $(\nu f_{5/2}^{-1} \pi h_{9/2})$ configuration coupled with the 0_1^+ state of the even-even core: ^{208}Rn. It is seen from Fig. 3.13 that energies of negative parity states become lower and lower from ^{212}Fr to ^{208}Fr.

Calculated results of the $B(E2)$ values, magnetic moments and quadrupole moments for Fr isotopes are given in Tables 3.13 and 3.14 in comparison with the experimental data [5, 63, 72–74, 76, 77, 79]. The small transition rates of the $B(E2; 17/2_1^- \to 13/2_1^-)$ and $B(E2; 21/2_1^- \to 17/2_1^-)$ values for ^{213}Fr are well reproduced. This nucleus is a system with five valence protons. All the $13/2_1^-$, $17/2_1^-$, and $21/2_1^-$ states are seniority $v = 3$ systems assuming the single-j ($j = h_{9/2}$) scheme. The $E2$ transition rates are hindered among states with the same seniority in this system [80]. Due to these small transition rates, the $17/2_1^-$ and $21/2_1^-$ states are isomers with half-lives of 505(14) ns and 18(1) ns [63]. It should be noted that the $9/2_1^-$ state has a seniority $v = 1$. Thus the $B(E2; 13/2_1^- \to 9/2_1^-)$

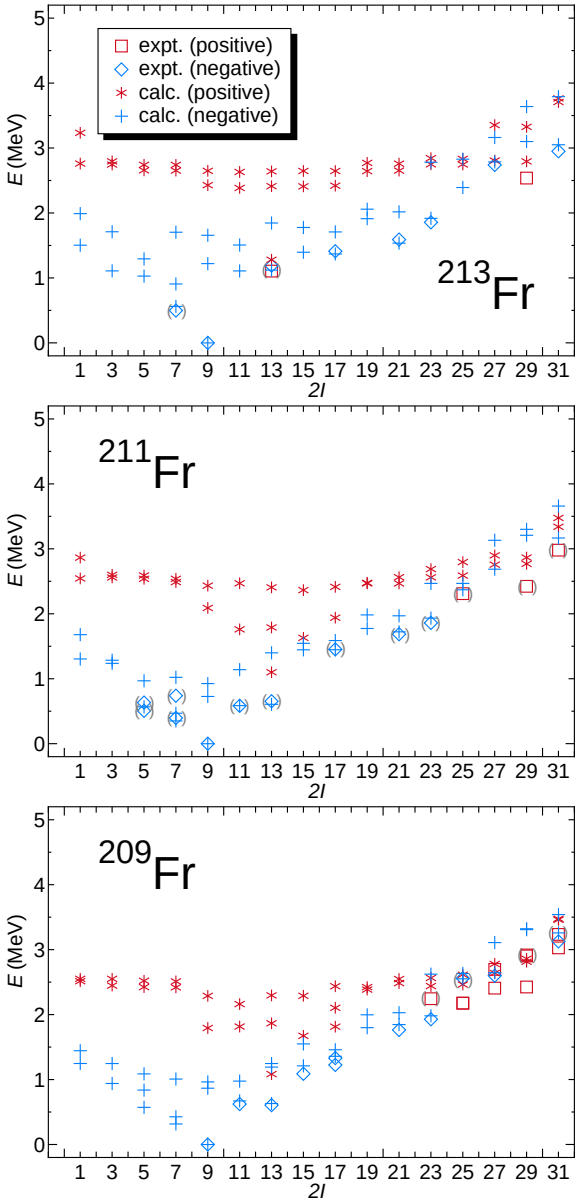

Figure 3.12: Same as fig. 3.2, but for odd-mass Fr isotopes. The experimental data are taken from Refs. [63, 72, 74, 77].

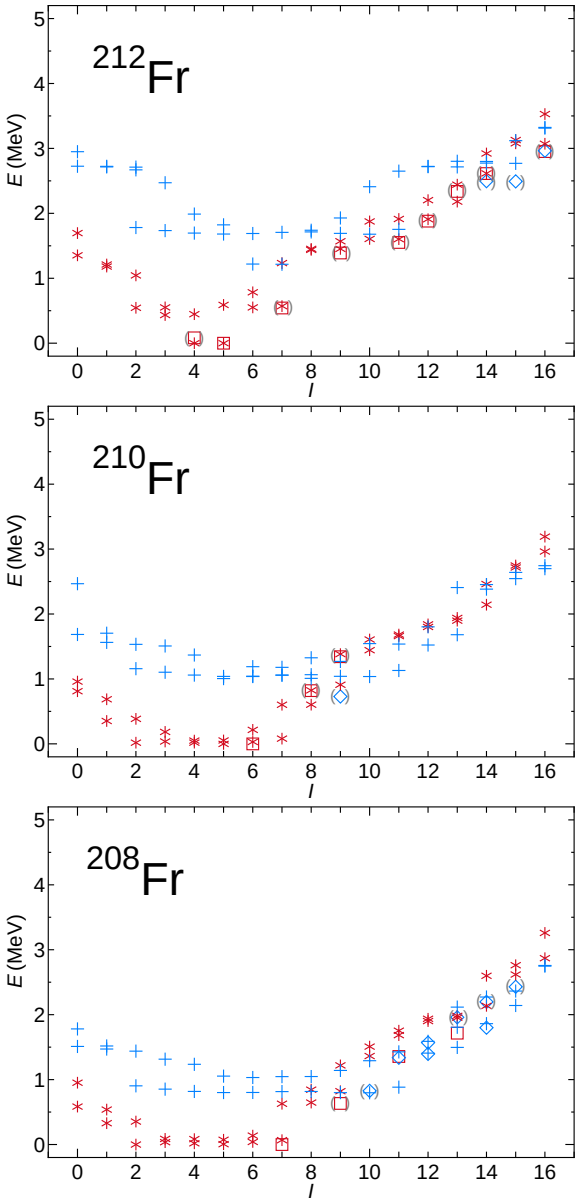

Figure 3.13: Same as fig. 3.2, but for doubly-odd Fr isotopes. The experimental data are taken from Refs. [5, 46, 63, 73, 76].

Table 3.13: Same as table 3.3,but for Fr isotopes. The experimental data are taken from Refs. [5, 63, 72–74, 76, 77, 79].

	$B(E2)$	
^{213}Fr	expt.	calc.
$7/2_1^- \rightarrow 9/2_1^-$		1.056
$13/2_1^- \rightarrow 9/2_1^-$	>0.0015	5.770
$17/2_1^- \rightarrow 13/2_1^-$	0.55(4)	0.010
$21/2_1^- \rightarrow 17/2_1^-$	0.0439(20)	0.071
$27/2_1^- \rightarrow 23/2_1^-$	0.001960(4)	4.061
$31/2_1^- \rightarrow 27/2_1^-$	1.133(14)	3.260
^{211}Fr	expt.	calc.
$7/2_1^- \rightarrow 9/2_1^-$		15.564
$5/2_1^- \rightarrow 7/2_1^-$		3.156
$5/2_1^- \rightarrow 9/2_1^-$		11.866
$13/2_1^- \rightarrow 9/2_1^-$	>0.063	12.832
$17/2_1^- \rightarrow 13/2_1^-$	>0.011	17.934
$21/2_1^- \rightarrow 17/2_1^-$	3.9(4)	3.520
$29/2_1^+ \rightarrow 25/2_1^+$	0.38(8)	0.376
^{209}Fr	expt.	calc.
$13/2_1^- \rightarrow 9/2_1^-$		19.673
$11/2_1^- \rightarrow 9/2_1^-$		17.628
$23/2_1^- \rightarrow 21/2_1^-$	>1.6	0.478
^{212}Fr	expt.	calc.
$4_1^+ \rightarrow 5_1^+$		0.002
$7_1^+ \rightarrow 5_1^+$		5.369
$11_1^+ \rightarrow 9_1^+$	0.00095(3)	0.194
^{210}Fr	expt.	calc.
$8_1^+ \rightarrow 6_1^+$		5.586
$9_1^+ \rightarrow 8_1^+$		0.816
^{208}Fr	expt.	calc.
$9_1^+ \rightarrow 7_1^+$		18.092

Table 3.14: Same as table 3.4, but for Fr isotopes. The experimental data are taken from Refs. [5, 63, 72–74, 76, 77].

	μ		Q	
^{213}Fr	expt.	calc.	expt.	calc.
$7/2_1^-$		+4.187		−0.283
$9/2_1^-$	+4.02(8)	+3.780	−0.14(2)	−0.024
$17/2_1^-$	7.5(14)	+7.164		−0.022
$21/2_1^-$	9.32(3)	+8.819		−0.032
$13/2_1^+$		+7.394		−0.440
$29/2_1^+$	15.22(3)	+14.120		−0.709
^{211}Fr	expt.	calc.	expt.	calc.
$7/2_1^-$		+3.332		−0.463
$9/2_1^-$	+4.00(8)	+3.726	−0.19(3)	−0.048
$13/2_1^+$		+7.277		−1.192
$29/2_1^+$	15.37(15)	+13.936	−1.1(2)	−1.166
^{209}Fr	expt.	calc.	expt.	calc.
$7/2_1^-$		+3.363		−0.482
$9/2_1^-$	+3.95(2)	+3.692	−0.24(2)	−0.129
$13/2_1^+$		+7.261		−1.381
^{212}Fr	expt.	calc.	expt.	calc.
4_1^+		+3.419		−0.028
5_1^+	4.62(9)	+4.079	−0.10(1)	−0.032
7_1^+		+4.678		+0.255
11_1^+	9.89(4)	+9.096		−0.022
22_1^+	22(4)	+14.954		−0.470
15_1^-	15.64(12)	+14.030	0.84(13)	−0.906
^{210}Fr	expt.	calc.	expt.	calc.
6_1^+	+4.40(9)	+3.948	+0.19(2)	+0.291
8_1^+		+4.638		+0.183
9_1^+		+4.940		+0.487
^{208}Fr	expt.	calc.	expt.	calc.
7_1^+	4.75(10)	+4.318	0.00(4)	+0.050
9_1^+		+4.927		+0.014
10_1^-		+2.314		+0.726

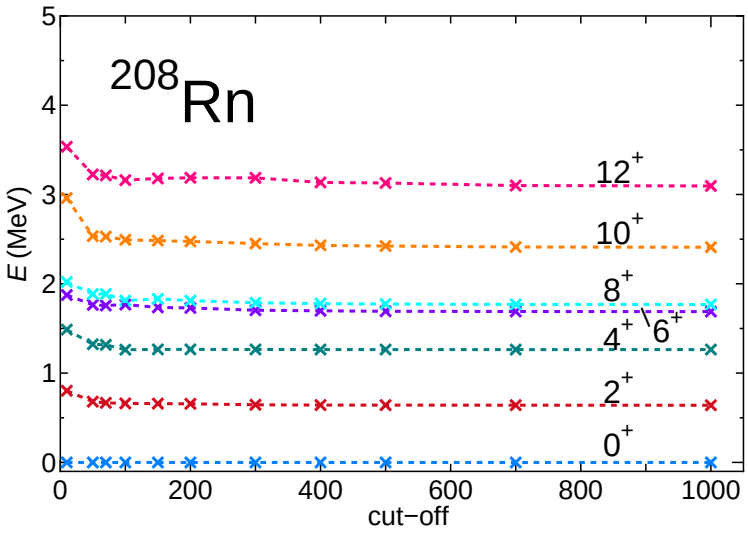

Figure 3.14: The convergence of energies for yrast states up to 12^+ for ^{208}Rn. The horizontal axis indicates the number of states taken for the diagonalization in the neutron-proton system, L_c.

value is not hindered. Examples of these seniority isomers are also seen in mass $A \sim 130$ region [8].

The quadrupole moments of the $9/2^-_1$ states for odd-mass nuclei are calculated several times smaller than experimental values. However, the magnetic moments of the same states are well reproduced.

3.4 Discussions for nuclei around mass 210

3.4.1 Validity of the truncation

Here the validity of the truncation discussed in Sec. 2.2 is confirmed. Fig. 3.14 shows the convergence of energies for yrast states up to 12^+ for ^{208}Rn, which is a system with four neutron holes and four proton particles form the doubly-magic core ^{208}Pb. In this figure, horizontal axis indicates the number of states taken for the diagonalization in the neutron-proton system, L_c. It is seen that energies rapidly converge from $L_c = 10$ to $L_c = 50$ and $L_c = 500$ is enough for the convergence.

3.4.2 Magnetic moments and quadrupole moments

As discussed in Sec. 4.3.2, the following observations are found in various cases; the calculated quadrupole moment of one specific state does not agree with the experimental data even though the calculated magnetic moment of the same state agrees with the experimental data. This phenomenon was also frequently seen in nuclei around mass 130 [8]. Here we try to shed light on this issue.

This phenomenon might be explained by the sensitiveness of operators on the mixture of states. Our assertion is made as follows. If the true state is a mixture of one main state and another secondary state, the quadrupole moment is largely affected by this admixture whereas the the magnetic moment is less affected.

Table 3.15: Magnetic moments and quadrupole moments with and without mixing of the second excited states for 10_1^- states of Bi isotopes in comparison with the experimental data. Calc1 (ratio1) represents the initial magnetic and quadrupole moments (ratio of the initial moment to the experimental value) without admixture of states. Calc2 (ratio2) represents magnetic and quadrupole moments (ratio of the calculated moment after mixing to the experimental value) with admixture of the second excited states. The mixing amplitude $\alpha = 0.979$ is taken for ^{206}Bi and $\alpha = 0.940$ is taken for ^{204}B.

^{206}Bi (10_1^-)	expt.	calc1	calc2	ratio1	ratio2
Q	0.049(9)	-0.225	-0.098	4.59	**2.00**
μ	2.644(14)	$+2.259$	$+2.030$	0.85	0.76
^{204}Bi (10_1^-)	expt.	calc1	calc2	ratio1	ratio2
Q	0.063(12)	-0.298	-0.126	4.74	**2.00**
μ	2.36(23)	$+2.269$	$+1.827$	0.96	0.77

Suppose that two states with the same spin and parity are slightly mixed,

$$|\varphi\rangle = \alpha\,|\varphi_1\rangle + \sqrt{1-\alpha^2}\,|\varphi_2\rangle\,, \tag{3.7}$$

where $|\varphi_1\rangle$ and $|\varphi_2\rangle$ represent the main state and the secondary one, respectively. Here it is assumed that the mixing amplitude α is real and $|\alpha| \simeq 1$. Then any electromagnetic moment is approximately calculated as

$$\langle\varphi|\,\hat{O}\,|\varphi\rangle \sim \alpha^2\,\langle\varphi_1|\,\hat{O}\,|\varphi_1\rangle + 2\alpha\sqrt{1-\alpha^2}\,\langle\varphi_1|\,\hat{O}\,|\varphi_2\rangle\,, \tag{3.8}$$

where $\hat{O}$ is either the magnetic moment operator or the quadrupole moment operator. To see influences by the admixture of the first (main) and the second (secondary) states, the mixing ratios of two states for the operator $\hat{O}$ defined by $S = \langle\varphi_1|\,\hat{O}\,|\varphi_2\rangle\,/\,\langle\varphi_1|\,\hat{O}\,|\varphi_1\rangle$ are numerically evaluated for the magnetic moment and the quadrupole moment.

For the 10_1^- state of ^{206}Bi, it is calculated as $S_M = -0.147$ for the magnetic moment and as $S_Q = -1.295$ for the quadrupole moment. Here $|\varphi_1\rangle = \left|10_1^-\right\rangle$ and $|\varphi_2\rangle = \left|10_2^-\right\rangle$ are assumed. For the 10_1^- state of ^{204}Bi, it is calculated as $S_M = -0.123$ for the magnetic moment and as $S_Q = -0.719$ for the quadrupole moment. It is generally true that the S values of the quadrupole moments are at least several times larger than those of the magnetic moments. Namely, the quadrupole moment is more sensitive to the admixture of states than the magnetic moment.

In order to see the actual effect of admixture of two neighboring states, magnetic moments and quadrupole moments are calculated with and without admixture of states assuming appropriate mixing amplitude α's. Table 3.15 shows calculated magnetic moments and quadrupole moments in comparison with those by the admixture of states for the 10_1^- states of ^{206}Bi and ^{204}Bi in comparison with the experimental data. $\alpha = 0.979$ (0.940) is taken for ^{206}Bi (^{204}Bi), which is so determined that each ratio of the calculated

quadrupole moment after mixing to the experimental one becomes two. Then the ratio of the calculated magnetic moment to the experimental one is reduced from 0.85 to 0.76 for ^{206}Bi. Thus the calculated magnetic moment is slightly deteriorated whereas the quadrupole moment is largely improved. ^{204}Bi also shows a similar tendency. This analysis also shows that admixture of neighboring states is insufficient to simultaneously explain disagreements to experiment for the quadrupole moment and the magnetic moment.

The reason for different sensitivities to the admixture of states for the quadrupole moment and the magnetic moment might be surmised as follows. The magnetic moment operator as a one-body operator changes spin up to only one. In contrast the quadrupole moment one-body operator changes spin up to two. It is inferred that the quadrupole moment operator more largely mix single-particle orbitals compared to the magnetic moment operator and consequently the quadrupole moment is more easily affected by the admixture of states.

The other possibility which explains this phenomenon is the difference of effective charges of orbitals. In this study, we assume values of effective charge are constant for all single-particle orbitals. However, it is reasonable that the effective charges of each orbital are different. The 10^-_1 states of ^{206}Bi consist of the $[\nu(p_{1/2}f_{5/2}p_{3/2})^2 i_{13/2}\pi h_{9/2}]$ configuration. The $0i_{13/2}$ orbital is the highest-j orbital among six orbitals in this region and there is a possibility that the effective charge of the $0i_{13/2}$ orbital is largely different from effective charges of other orbitals. It is an interesting challenge to check whether the quadrupole moment is reproduced by changing the effective charge of the $0i_{13/2}$ orbital. This phenomenon should be further investigated in a future study.

3.4.3 The MP-8 interaction

In this study, a specific interaction with spin 8 between protons in the $0h_{9/2}$ and $1f_{7/2}$ orbitals (MP-8) given in Eq. (3.3) has been added as part of an effective interaction. In this section the necessity of this interaction is discussed.

Figure 3.15 shows the theoretical energy spectra for positive parity states in ^{210}Po with and without the MP-8 interaction in comparison with the experimental data [63, 73]. The theoretical calculation well reproduces the experimental data with the MP-8 interaction. By comparing results with and without the MP-8 interaction, it is concluded that the influences coming from the MP-8 interaction are not so large on almost all the states except for the 8^+_2 state. The calculated energy of the 8^+_2 state without the MP-8 interaction is 0.490 MeV higher than that with the MP-8 interaction. The 8^+_1 state mainly consists of the $(\pi h^2_{9/2})$ configuration whereas the 8^+_2 state mainly consists of the $(\pi h_{9/2}f_{7/2})$ configuration. Therefore the 8^+_2 state is directly affected by the MP-8 interaction.

Figure 3.16 shows the theoretical energy spectra for negative parity states in ^{211}At with and without the MP-8 interaction in comparison with the experimental data [63,74]. Low-lying states below 1.5 MeV are not at all affected by the MP-8 interaction. However, large influences are seen for energy levels over 1.5 MeV. For example, the $23/2^-_1$ state is not well reproduced without the MP-8 interaction. Since the $23/2^-_1$ state is found to consist of the $[\pi h_{9/2}(h_{9/2}f_{7/2})^2_{8^+}]$ configuration, the state is largely affected by the MP-8 interaction.

Figure 3.17 shows the theoretical energy spectra for positive parity states in ^{212}Rn with and without the MP-8 interaction in comparison with the experimental data [63,76]. There are no influences on the low-lying states below 1.5 MeV. However, the 8^+_2, 12^+_2 and

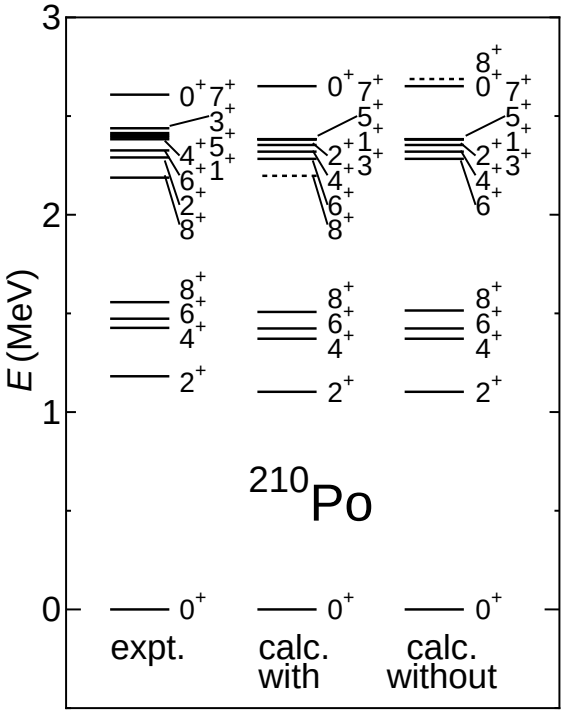

Figure 3.15: Comparison between the experimental spectra (expt.) and the shell-model results with (calc. with) and without (calc. without) the MP-8 interaction for positive parity states in ^{210}Po. The experimental data are taken from Refs. [63, 73]. The states with the energy difference of more than 0.1 MeV between those with and without the MP-8 interaction are indicated by dotted lines.

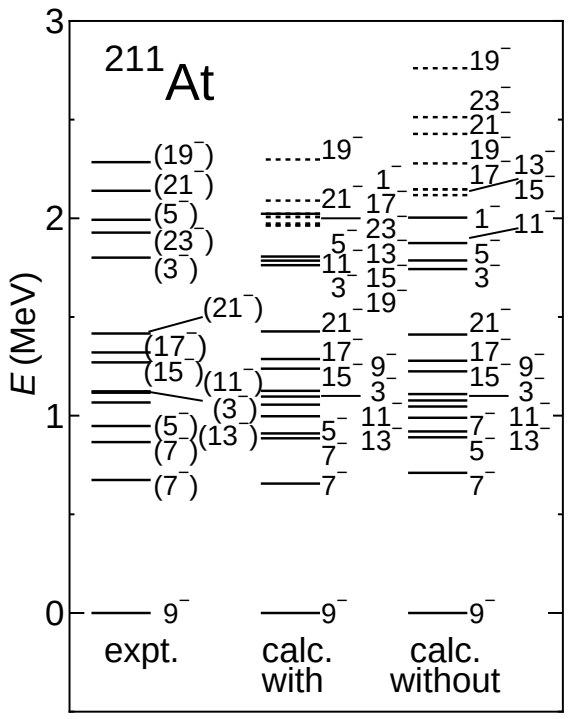

Figure 3.16: Same as fig. 3.15, but for negative parity states of ^{211}At. Spin is denoted by twice the original value. The experimental data are taken from Refs. [63, 74]. Only the first and second states for each spin are shown.

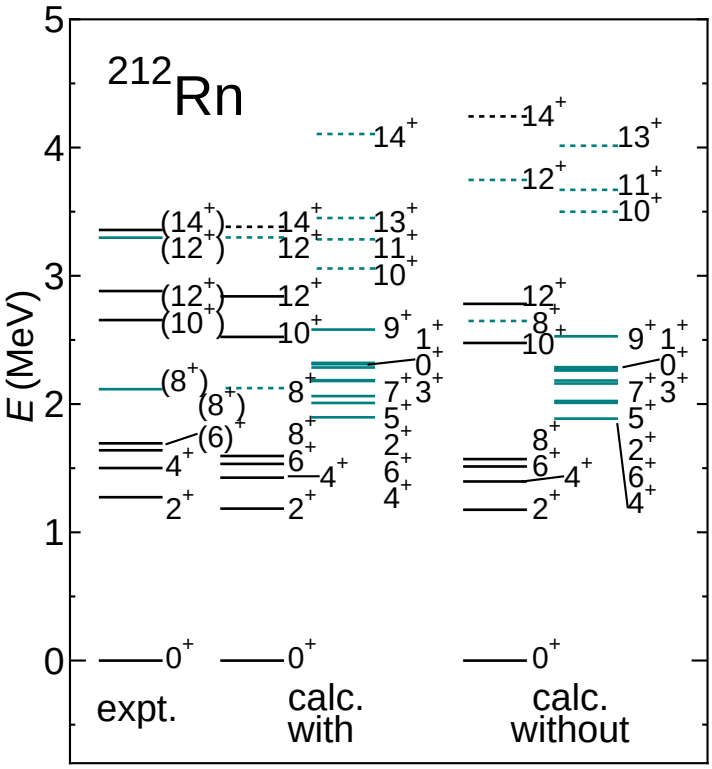

Figure 3.17: Same as fig. 3.15, but for positive parity states of ^{212}Rn. The experimental data are taken from Refs. [63,76]. Only the first and second states for each spin are shown. The 14_2^+ state calculated without the MP-8 interaction is not shown in the figure, but this state is predicted at 5.282 MeV.

14_1^+ states are not well reproduced without the MP-8 interaction. This is due to the fact that the 8_2^+, 12_2^+ and 14_1^+ states mainly consist of the $[\pi(h_{9/2}^2)_{I^+}(h_{9/2}f_{7/2})_{8^+}]$ configuration, where those states with $I = 0$, $I = 4$, and $I = 6$ correspond to the 8_2^+, 12_2^+ and 14_1^+ states, respectively.

As a phenomenological study any kind of two-body interactions which act nucleons in any two orbitals should be introduced for a better fit to the experimental data, but only the MP-8 interaction is introduced in the present study. This is because both the $0h_{9/2}$ and $1f_{7/2}$ orbitals are the most low-lying orbitals for protons and influences from these two low-lying orbitals are dominantly observed in experiment. However, why spin of this specific interaction must be eight, is not clarified from the present analysis. The reason might be related with the fact that spin 8 is the maximum spin in both the $(\pi h_{9/2}^2)$ and $(\pi h_{9/2}f_{7/2})$ configurations. The detailed analysis, however, is necessary in a future analysis.

3.4.4 The particle number dependence of the $i_{13/2}$ orbitals

In this study, it has been assumed that single-particle energies of the neutron and the proton $0i_{13/2}$ orbitals change linearly with the numbers of valence neutron holes and proton particles. These number dependences are introduced for better descriptions of energies of the $13/2_1^+$ states of odd-mass nuclei. It should be noted, however, that the influences of these number dependences are not large and rough energies of the $13/2_1^+$ states are

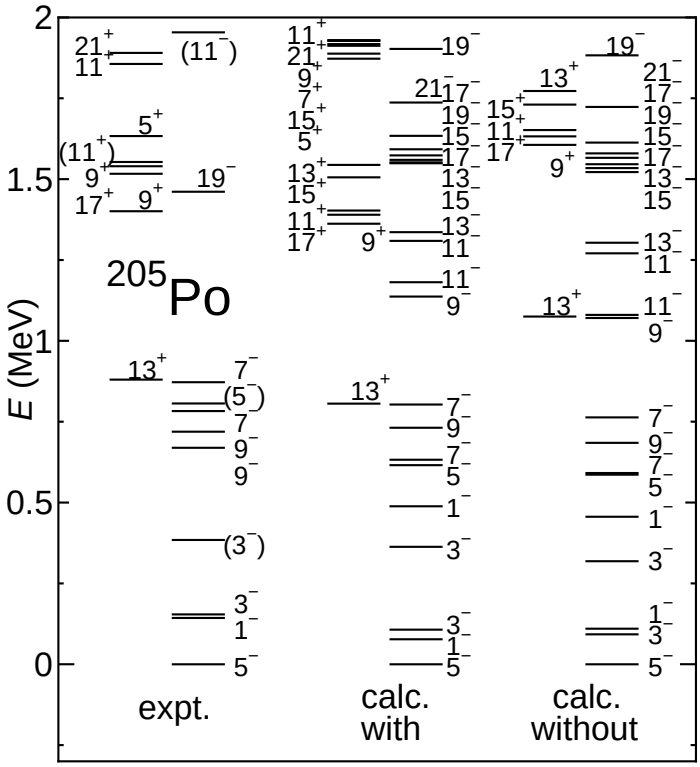

Figure 3.18: Comparison between the experimental spectra (expt.) and the shell-model results with (calc. with) and without (calc. without) the particle number dependence of the $i_{13/2}$ orbitals for ^{205}Po. The experimental data are taken from Refs. [63,66]. Only the first and second states for each spin and parity are shown. Spin is denoted by twice the original value.

reproduced without the number dependences.

Figure 3.18 and 3.19 show the theoretical energy spectra for positive parity states in ^{205}Po and ^{207}Rn with and without the number dependence of the $0i_{13/2}$ orbitals in comparison with the experimental data [63, 66, 69]. For calculations without the number dependences, single-particle energies of the $0i_{13/2}$ orbitals are taken as 1.633 MeV for neutrons and 1.609 MeV for protons, which are taken from the experimental excitation energies of ^{207}Pb (for neutrons) and ^{209}Bi (for protons). With the number dependences, energies of positive parity states are better reproduced than those without the number dependences, but differences of these two results are small.

It is known that the single-particle energies are shifted by the effects of the monopole interactions of the nucleon-nucleon (NN) interaction as protons or neutrons occupy certain orbitals [81–83]. There are a lot of studies which consider the effects of the monopole interaction in lighter mass regions (e.g. see Ref. [84]). For example, a mechanism of change of single-particle energies in the *p*- and *sd*-shell regions were studied by analyzing contributions from different components of NN interactions [85]. It was shown that the neutron-proton monopole interactions play an important role for the change of the single-particle energies and the triplet-even component due to the central interactions and the second-order tensor correlations are dominant for the monopole interaction.

Since the present study is carried out from a phenomenological point of view, the shifts of single-particle energies coming from the monopole interactions are not considered. The

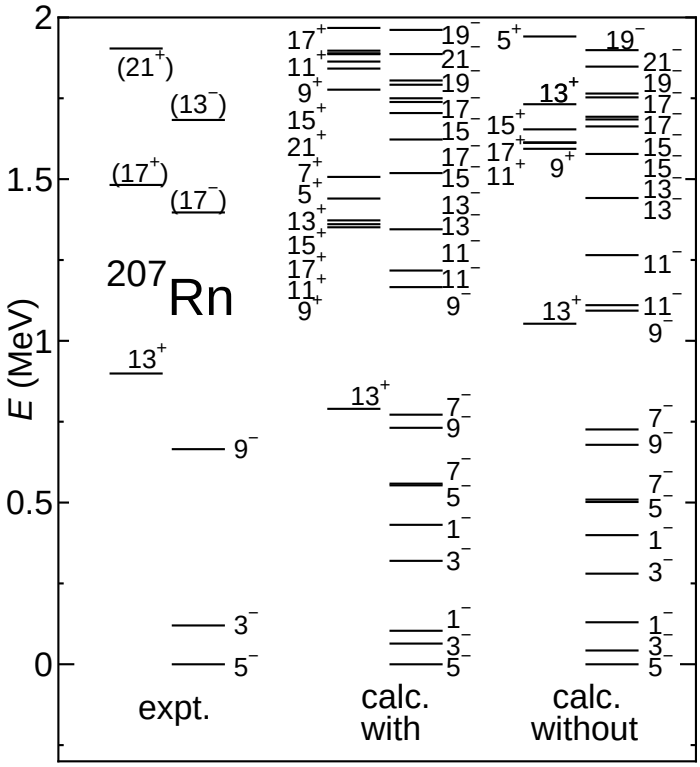

Figure 3.19: Same as fig. 3.18, but for ^{207}Rn. The experimental data are taken from Refs. [63, 69].

number dependence of the single-particle energy has been introduced only for the $0i_{13/2}$ orbitals. It is because this effect is easily seen since parity of the $0i_{13/2}$ orbital is only positive among all the orbitals. As a phenomenological study we do not pursue this number-dependence problem of single-particle energies any further, but this issue is so important that it should be studied in the future from the point of view of the monopole interactions.

3.4.5 The $\nu i_{13/2}^{-1} \otimes \pi i_{13/2}$ band

In the medium and heavy nuclei, intruder orbitals are important to describe the low-lying nuclear structure. For example, the intruder orbital between the magic numbers 28 and 50 is the $0g_{9/2}$ orbital and this orbital plays an important role for the nuclear structure. In the region between the magic numbers 50 and 82, the intruder orbital is the $0h_{11/2}$ orbital and states with the $(\nu h_{11/2}^{-1} \pi h_{11/2})$ configuration are observed and analyzed in doubly-odd nuclei in the mass $A \sim 130$ region (e.g. see references in Ref. [86]). In the mass $A \sim 130$ region, states which have the $(\nu h_{11/2}^{-1} \pi h_{11/2})$ configuration are occasionally located below those states with the positive-positive configuration, where the positive-positive configuration means that the state consists of a positive-parity state for the neutron part and also a positive-parity state for the proton part. Note that only the $0h_{11/2}$ orbital has negative parity and other orbitals have positive parity in the mass $A \sim 130$ region. The yrast and yrare bands with the $(\nu h_{11/2}^{-1} \pi h_{11/2})$ configuration are experimentally found to be almost degenerate in energy. These bands are called $\Delta I = 1$ doublet bands [87–89].

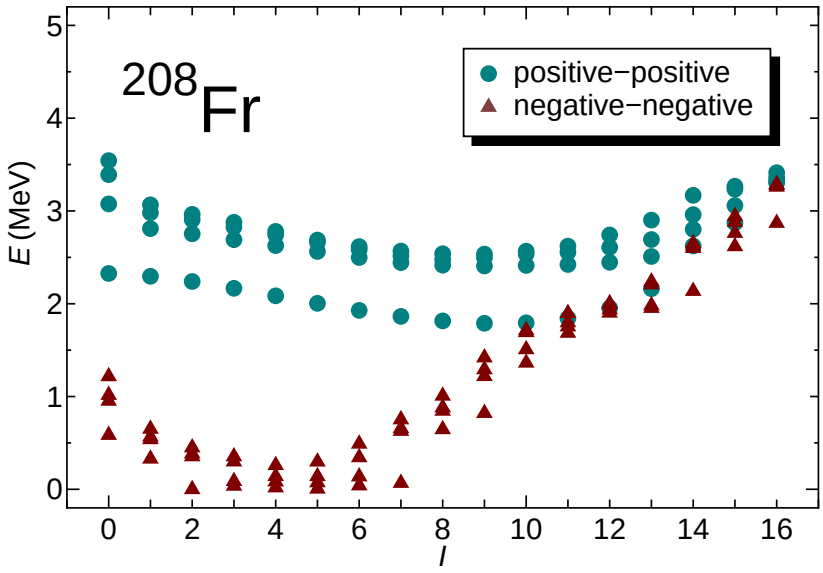

Figure 3.20: Theoretical energy levels for positive parity states in ^{208}Fr. The circles and triangles represent the theoretical results of the positive-positive configuration and negative-negative configurations, respectively. Up to four calculated states are shown for each spin and each configuration.

In the region treated in this study, the intruder orbital is the $0i_{13/2}$ orbital. Only this orbital has positive parity among the six orbitals. Just like the nuclei in the mass $A \sim 130$ region, states with the $(\nu i_{13/2}^{-1} \pi i_{13/2})$ configuration are expected to be observed in doubly-odd nuclei.

Figure 3.20 shows the calculated energy levels of the positive parity states for ^{208}Fr, which are separately shown for the positive-positive configuration and the negative-negative configurations. Here states of the positive-positive configuration mean those states which consist of the positive-parity state for the neutron part and the positive-parity state for the proton part. Namely these states have the $(\nu i_{13/2}^{-1} \pi i_{13/2})$ configuration. States of the negative-negative configuration means those states which consist of the negative-parity state for the neutron part and the negative-parity state for the proton part.

As seen in Fig. 3.20 states of the positive-positive configuration are calculated over 2.0 MeV. It is theoretically found that the lowest $0^+, 1^+, \cdots, 13^+$ states with the positive-positive configuration located at $2.0 \sim 2.5$ MeV, consist of the $(\nu i_{13/2}^{-1} \pi i_{13/2})$ configuration coupled with the 0_1^+ state of the corresponding even-even core of ^{208}Rn. States over these states with the positive-positive configuration consist of the $(\nu i_{13/2}^{-1} \pi i_{13/2})$ configuration coupled with the $2_1^+, 4_1^+, \cdots$ states of the ^{208}Rn core. In ^{208}Fr, states with the $(\nu i_{13/2}^{-1} \pi i_{13/2})$ configuration are calculated in energy above the negative-negative configuration in low-spin states. Thus no $\Delta I = 1$ doublet bands are expected in this region at least near ^{208}Pb as the yrast band.

In the mass $A \sim 130$ region, the neutron $0h_{11/2}$ orbital is one of the low-lying orbital and the proton $0h_{11/2}$ orbital is located about 2.8 MeV from a doubly-magic core. In contrast, the $0i_{13/2}$ orbitals are located in the middle of the shell for neutrons and protons in the mass $A \sim 210$ region. To make the $(\nu i_{13/2}^{-1} \pi i_{13/2})$ configuration, both one neutron and one proton need to be excited to the $0i_{13/2}$ orbitals. For the calculation of ^{208}Fr, the

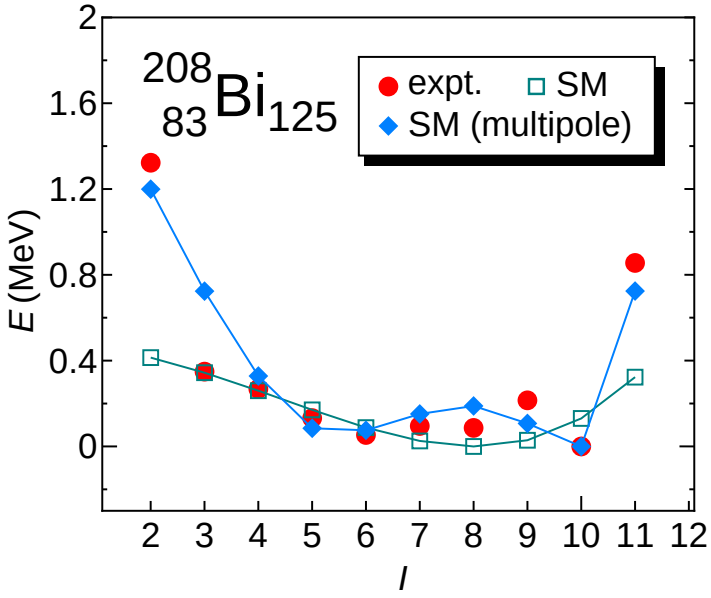

Figure 3.21: Comparison between the experimental energy levels (expt.) and two kinds of calculated results for ^{208}Bi using phenomenological neutron-proton two-body interactions : the shell-model results (SM) with only the QQ interaction and the SM results including multipole interactions [SM(multipole)].

$0i_{13/2}$ orbital for neutrons is located at 1.373 MeV and the $0i_{13/2}$ orbital for protons is located at 1.409 MeV in our calculation. In much lighter Fr isotopes one may find those states with the $(\nu i^{-1}_{13/2}\pi i_{13/2})$ configuration as the yrast states.

3.4.6 The necessity of other kinds of interactions

In this section ^{208}Bi is discussed. ^{208}Bi is a system of one neutron hole and one proton particle with the doubly magic core ^{208}Pb. So far this nucleus has been treated using only the neutron-proton QQ interaction in the present model. As seen fig. 3.5, the 2^-_1, 3^-_1, $\cdots$, 11^-_1 states with the $(\nu i^{-1}_{13/2}\pi h_{9/2})$ configuration are seen in low-lying states. On the other hand, the 10^-_1 state, which is the neighboring spin state to the 11^-_1 state is the lowest negative parity state among members of the $(\nu i^{-1}_{13/2}\pi h_{9/2})$ configuration. This feature has not been reproduced in the present interaction. As mentioned before, only the QQ interaction has been employed for the neutron-proton interaction. New kinds of interactions besides the QQ interaction should be introduced to reproduce the energy gap between the 10^-_1 and 11^-_1 states.

The experimental 2^-_1 and 11^-_1 states are especially higher compared to other spin states. These states are generally well reproduced. However, theoretical 2^-_1 and 11^-_1 states are calculated 0.92 MeV and 0.55 MeV lower than experiment, respectively.

To examine the necessity of the new kind of the interactions, single-j calculations are phenomenologically performed. In this calculation, new kinds of higher-multipole interactions between the neutron $i^{-1}_{13/2}$ orbital and the proton $h_{9/2}$ orbital are introduced in addition to the QQ interaction. The definition of interaction strengths are given in Appendix A.3.

Fig. 3.21 shows the calculated results using the hexadecapole interaction [$\chi^{(4)} = +6.0$]

in addition to the quadrupole interaction [$\chi^{(2)} = +7.0$] between neutrons and protons in each single-j orbital (the neutron $i_{13/2}$ and proton $h_{9/2}$ orbitals). Theoretical energy of the 10^- state is adjusted to the experimental one. Using this new interaction the 10^- state becomes the lowest state and the energy gap between the 10^- and 11^- states and energy of the 2^- states are well reproduced.

This problem was also seen in the previous calculation for ^{132}Sb [8], which is a system with one neutron hole and one proton particle form the doubly magic core ^{132}Sn.

Chapter 4

Analysis for nuclei around mass 220

4.1 Nuclei around mass 220

In this Chapter, we analyze structure of $^{210-212}$Pb, $^{210-213}$Bi, $^{211-214}$Po, $^{212-215}$At, $^{213-216}$Rn, and $^{214-217}$Fr nuclei. Nuclei in this mass region have more than 126 neutrons and more than 82 protons. These nuclei are mainly α-disintegrated.

Nuclear structure of these nuclei has not been studied enough compared to the nuclei around mass 210. Recently, ^{212}Bi was studied using ^{238}U beam and two isomers with long half lives of 25 min and 7.0 min were confirmed [90]. However, only some states are observed and spin and parity of a few states are assigned in this nucleus. The level structure of ^{213}Po was studied using the ^{18}O + ^{208}Pb reaction and the γ multidetector array [91]. The level scheme was built up to about 2.0 MeV excitation energy and spin was assigned up to 25/2 from the triple γ coincidence data. The constructed level scheme was compared with the empirical shell-model calculation [91]. ^{211}Pb was studied using the deep-inelastic reactions between ^{208}Pb ions and a thick ^{238}U target [92]. Spin and parity of high-lying states were confirmed and three high-spin isomers were identified. Configurations of several states were assigned by comparing with the shell model calculation using empirical interactions [92]. High-spin states of ^{210}Pb and ^{211}Bi were studied using deep-inelastic collisions between a pulsed beam of ^{208}Pb ions and a ^{238}U target [93]. Configurations of isomers were discussed and analyzed.

Theoretically, nuclei with a few valence nucleons were studied using the shell model approach. ^{210}Bi is a system of one neutron and one proton with the doubly magic ^{208}Pb core and relatively easy to analyze theoretically [94–98]. It is an important nucleus to reveal the interaction between a neutron and a proton. The theoretical problem on this nucleus is that the spin and parity of the experimental ground state is 1^- with the $(\nu g_{9/2}\pi h_{9/2})$ configuration. The 0^-, 1^-, $\cdots$, 9^- states with the $(\nu g_{9/2}\pi h_{9/2})$ configuration are observed in this nucleus. From the Nordheim strong coupling rule [98, 99], the 0^- state should be the lowest in energy among states with the $(\nu g_{9/2}\pi h_{9/2})$ configuration. However, the experimental observation is different from this theoretical prediction. It was concluded by theoretical studies using empirical two-body studies that tensor-force components are needed to reproduce the ground state [94–96]. Recently, more precise calculation employed by the interaction delivered from the NN potential was performed and the good agreement with the experimental data was obtained [98]. Calculated several low-lying configurations, the $(\nu g_{9/2}\pi h_{9/2})$, $(\nu i_{11/2}\pi f_{7/2})$, $(\nu i_{11/2}\pi h_{9/2})$, $(\nu g_{9/2}\pi f_{7/2})$, and $(\nu j_{15/2}\pi h_{9/2})$ configurations, for ^{210}Bi, ^{212}Bi, ^{212}At, ^{216}At, and ^{216}Fr were compared with the exper-

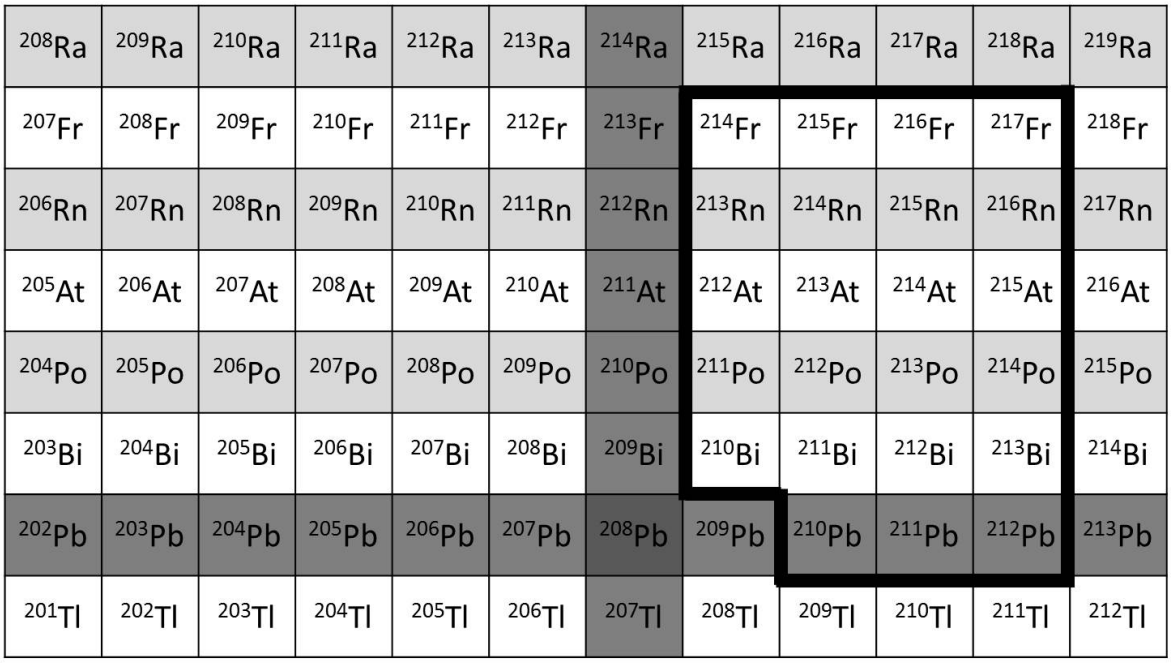

Figure 4.1: The nuclei discussed in this Chapter (nuclei framed by a bold line). The shaded nuclei are nuclei which have the magic number 82 protons and 126 neutrons.

imental results [100]. The energy levels and transition rates of the low-lying states in ^{210}Pb and ^{210}Bi ware calculated using a conventional shell-model approach with a central Gaussian-shaped interaction [56]. Although orders of energies of several states were reversely predicted, calculations predicted transition rates and $M1$-$E2$ branching ratios well.

As shown in the above, some nuclei in this mass region have been analyzed theoretically. However, most of studies calculated only a few nuclei and there are no systematic calculation in this mass region.

In this Chapter, even-even, odd-mass, and doubly-odd nuclei for of Pb, Bi, Po, At Rn, and Fr isotopes with up to four neutron-particles and five proton-particles systems are treated assuming ^{208}Pb as a doubly magic core. The nuclei discussed in this Chapter are figured in Fig. 4.1. The energy spectra and electromagnetic properties are calculated and compared with the experimental data. Isomeric states are analyzed in terms of the shell-model configurations. Furthermore, several nuclei are analyzed in detail at the end of this Chapter.

4.2 Theoretical framework for nuclei around mass 220

For single-particle levels, seven orbitals above the magic number 126, $1g_{9/2}$, $0i_{11/2}$, $0j_{15/2}$, $2d_{5/2}$, $3s_{1/2}$, $2g_{7/2}$, and $2d_{3/2}$ are taken for neutrons. For protons, all the six $0h_{9/2}$, $1f_{7/2}$, $0i_{13/2}$, $2p_{3/2}$, $1f_{5/2}$, and $2p_{1/2}$ orbitals in the major shell between the magic numbers 82 and 126 are taken. Both neutrons and protons are treated as particles. The single-particle

Table 4.1: Adopted single-particle energies ε_τ ($\tau = \nu$ or π) for neutrons and protons (in units of MeV). The energies for the neutron $0j_{15/2}$ orbital and the proton $0i_{13/2}$ and $1f_{7/2}$ orbitals are changed linearly with numbers of valence neutrons (N_ν) and protons (N_π). Definitions of $\epsilon_\nu(0j_{15/2})$, $\epsilon_\pi(i_{13/2})$, and $\epsilon_\pi(f_{7/2})$ are given in the text.

j	$1g_{9/2}$	$0i_{11/2}$	$0j_{15/2}$	$2d_{5/2}$	$3s_{1/2}$	$2g_{7/2}$	$2d_{3/2}$
ε_ν	0.000	0.779	$\epsilon_\nu(j_{15/2})$	1.567	2.032	2.491	2.538
j	$2p_{1/2}$	$1f_{5/2}$	$2p_{3/2}$	$0i_{13/2}$	$1f_{7/2}$	$0h_{9/2}$	
ε_π	3.634	2.826	3.119	$\epsilon_\pi(i_{13/2})$	$\epsilon_\pi(f_{7/2})$	0.000	

energies ε_τ ($\tau = \nu$ or π) employed in the present calculations are listed in Table 4.1. The single-particle energies for protons are the same as used in the calculation for nuclei around mass 210. Single-particle energies of neutrons are adopted from the experimental energy levels of ^{209}Pb. The particle number dependences on single-particle energies are assumed for the neutron $0j_{15/2}$ orbital and the proton $0i_{13/2}$ and $1f_{7/2}$ orbitals as follows in units of MeV:

$$\epsilon_\nu(0j_{15/2}) = 0.20N_\nu - 0.150N_\pi + 1.223, \tag{4.1}$$
$$\epsilon_\pi(0i_{13/2}) = -0.050N_\pi + 1.659, \tag{4.2}$$
$$\epsilon_\pi(1f_{7/2}) = 0.031N_\nu + 0.869, \tag{4.3}$$

where N_ν and N_π represent the number of valence neutrons and valence protons, respectively. Here, the adopted number dependence for the proton $0i_{13/2}$ orbital is the same as used for the calculation of nuclei around mass 210.

The adopted Hamiltonian is the same as described in Sec. 2.3. The adopted two-body interaction strengths are listed in Table 4.2. Here adopted strengths for protons are the same as ones used in nuclei around mass 210. The MP-8 interaction is also used with the same strength of $G^{(8)}_{\pi h_{9/2} f_{7/2}} = 0.50$. Only one set of strengths is adopted for all the nuclei for this mass region.

For $E2$ transition rates and quadrupole moments, the effective charges are taken as $e_\nu = 1.0e$ for neutrons and $e_\pi = 1.50e$ for protons. For magnetic moments, the adopted gyromagnetic ratios for orbital angular momenta are $g_{\ell\nu} = 0.00$, $g_{\ell\pi} = 1.00$, and those for spin are $g_{s\nu} = -2.87$ and $g_{s\pi} = 2.79$. These effective charges and gyromagnetic ratios are adjusted to reproduce the experimental data in single-closed nuclei.

4.3 Theoretical results for nuclei around mass 220

In this section, the theoretical results are given for each nucleus. The energy spectra, $E2$ transition rates, magnetic moments, and quadrupole moments are calculated. For energy spectra, up to four observed energy levels are shown from the yrast state for each spin and parity in experiment. As for the theoretical states, two levels for each spin and

Table 4.2: Strengths of adopted two-body interactions between neutrons (ν-ν) and those between protons (π-π). G_0 and G_2 indicate the strengths of the monopole (MP) and quadrupole-pairing (QP) interactions between like nucleons. G_L ($L = 4, 6, 8, 10$) denote the strengths for higher multipole-pairing (HMP) interactions between like nucleons. The strength of the proton two-body interaction between the $0h_{9/2}$ and $1f_{7/2}$ orbitals (MP-8) is taken as $G^{(8)}_{\pi h_{9/2} f_{7/2}} = 0.50$. The strength of the $Q_\nu Q_\pi$ interaction between neutrons and protons is taken as $\kappa_{\nu\pi} = 0.080$. The strengths of the MP, HMP, and MP-8 interactions are given in units of MeV. The strengths of the QP and QQ interactions are given in units of MeV/b^4 using the oscillator parameter $b = \sqrt{\hbar/M\omega}$.

	G_0	G_2	G_4	G_6	G_8	G_{10}
ν-ν	0.102	0.008	0.400	0.300	0.000	0.450
π-π	0.145	0.013	0.400	0.400	−0.600	0.000

parity from the lowest level are shown in general. If third or fourth states are observed in experiment, third or fourth energy levels are shown in theory.

4.3.1 Pb isotopes

Here $^{210-212}$Pb isotopes are discussed. Figure 4.2 shows the theoretical energy spectra for even-even Pb isotopes in comparison with the experimental data [63, 73, 76]. ^{210}Pb is a system of two neutron particles outside the doubly magic core ^{208}Pb. This nucleus gives us information about the interaction between two neutrons. The calculation reproduces energy levels of the yrast 0^+_1, 2^+_1, $\cdots$, 10^+_1 states well. The narrow energy gaps between the 4^+_1 and 6^+_1 states and the 6^+_1 and 8^+_1 states are well reproduced. This indicates that the adjustment of strengths of the interaction is appropriate. The 6^+_1 and 8^+_1 states are isomers with half lives of 49 ns and 201 ns, respectively [63]. As shown later, the transition rates from these isomeric states, namely the $B(E2; 8^+_1 \rightarrow 6^+_1)$ and $B(E2; 6^+_1 \rightarrow 4^+_1)$ values, are not small. These two states become isomers due to the narrow energy gaps of 0.097 MeV (between the 4^+_1 and 6^+_1 states) and 0.083 MeV (between the 4^+_1 and 6^+_1 states), respectively. The experimentally unobserved 12^+_1 state is calculated at 4.484 MeV. The degenerate negative parity states, the 3^-_1, 4^-_1, $\cdots$, 12^-_1 states at around 2.9 MeV consist of the $(\nu g_{9/2} j_{15/2})$ configuration. The degenerate 2^-_1, 3^-_2, $\cdots$, 13^-_1 states at around 3.7 MeV consist of the $(\nu i_{11/2} j_{15/2})$ configuration. The degenerate 5^-_3, 6^-_3, $\cdots$, 10^-_3 states at around 4.5 MeV consist of the $(\nu j_{15/2} d_{5/2})$ configuration.

In ^{212}Pb, spins of only several positive parity states are assigned in experiment. The yrast band is well reproduced in this calculation. The unobserved 10^+_1 state is calculated at 1.642 MeV. The experimental 3^-_1 states are located at 1.870 MeV and 1.820 MeV in ^{210}Pb and ^{212}Pb, respectively. The 3^-_1 state in ^{210}Pb has a large component of the two-phonon state $|3^-_1(^{208}\mathrm{Pb}) \otimes \mathrm{g.s.}(^{210}\mathrm{Pb})\rangle$ [101], which is beyond the present framework. The low-lying 3^- states associated with the 3^-_1 state in ^{208}Pb are also seen in Pb isotopes in

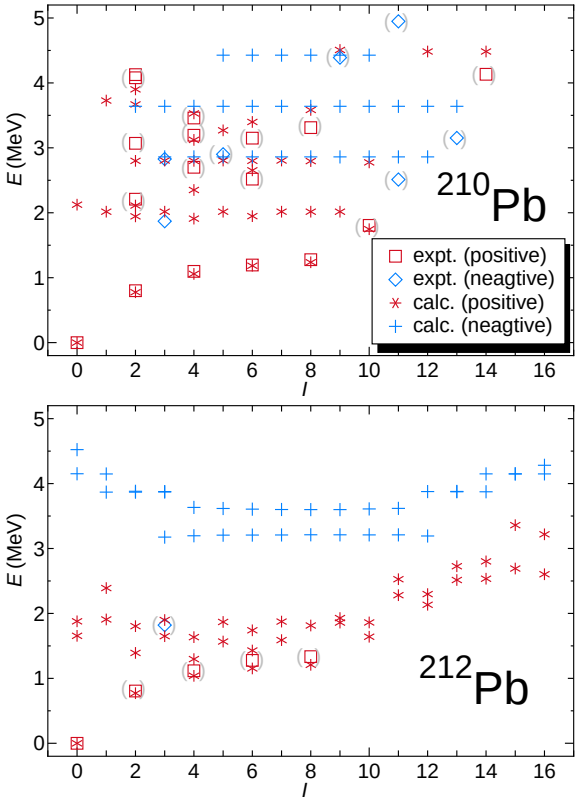

Figure 4.2: Theoretical energy spectra for even-even Pb isotopes in comparison with the experimental data [63, 73, 76]. The squares and diamonds represent experimental positive and negative parity states, respectively. Ambiguous states are shown with parentheses. The asterisks and crosses represent theoretical positive and negative parity states, respectively.

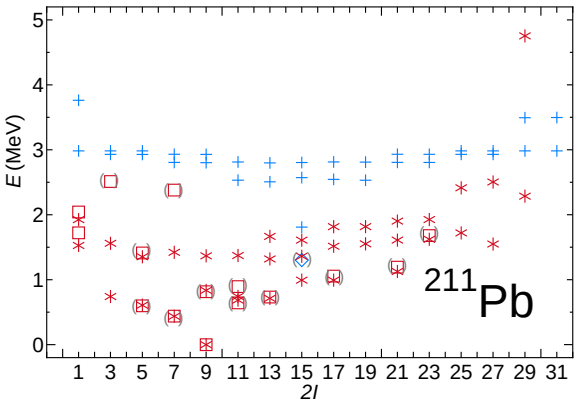

Figure 4.3: Theoretical energy spectra for odd-mass Pb isotopes in comparison with the experimental data [63,74]. The squares and diamonds represent experimental positive and negative parity states, respectively. Ambiguous states are shown with parentheses. The asterisks and crosses represent theoretical positive and negative parity states, respectively.

Table 4.3: Comparison between the experimental $B(E2)$ values (expt.) and the theoretical results (calc.) for Pb isotopes (in W.u.). The experimental data are taken from Refs. [63, 73, 74, 76, 92].

	$B(E2)$	
^{210}Pb	expt.	calc.
$2_1^+ \to 0_1^+$	1.4(4)	3.113
$4_1^+ \to 2_1^+$	4.8(9)	3.307
$6_1^+ \to 4_1^+$	2.1(8)	2.109
$8_1^+ \to 6_1^+$	0.7(3)	0.759
$10_1^+ \to 8_1^+$		0.018
^{212}Pb	expt.	calc.
$2_1^+ \to 0_1^+$		4.961
$4_1^+ \to 2_1^+$		0.565
$6_1^+ \to 4_1^+$		0.339
$8_1^+ \to 6_1^+$		0.119
$10_1^+ \to 8_1^+$		0.082
^{211}Pb	expt.	calc.
$5/2_1^+ \to 9/2_1^+$		2.355
$7/2_1^+ \to 9/2_1^+$		5.130
$11/2_1^+ \to 9/2_1^+$		0.529
$13/2_1^+ \to 9/2_1^+$		2.994
$21/2_1^+ \to 17/2_1^+$	1.36(23)	1.724
$27/2_1^+ \to 23/2_1^+$	1.0^{+2}_{-3} *	0.859

*Using theoretical transition energy of 29 keV [92].

the mass region 210 as discussed in Sec. 3.3.1.

Figure 4.2 shows the theoretical energy spectra for ^{211}Pb in comparison with the experimental data [63, 74]. The energy levels of low-lying positive parity states are well reproduced. The $(27/2_1^+)$ state with a half life of 159 ns is observed at least above 1.679 MeV [63]. The $27/2_1^+$ state is calculated at 1.549 MeV and consists of the $(\nu g_{9/2}^2 i_{11/2})$ configuration. This assignment of the configuration is consistent with the results in Ref. [92]. The $(21/2_1^+)$ state with a half life of 42(7) ns decays to the $(17/2_1^+)$ state [63]. These two states consist of the $(\nu g_{9/2}^3)$ configuration. As shown in Table 4.3, the measured $B(E2; 21/2_1^+ \to 17/2_1^+)$ value is 1.36(23) W.u. [63], which is not so small. This state becomes an isomer due to the small energy gap (0.137 MeV) between the $21/2_1^+$ and $17/2_1^+$ states.

Calculated results of the $B(E2)$ values, magnetic moments, and quadrupole moments for Pb isotopes are given in Tables 4.3 and 4.4 in comparison with the experimental data [63, 73, 74, 76, 92]. Most of experimental values are well reproduced in the calculation. The largest discrepancy between the experimental value and the theoretical one is seen in the $B(E2; 2_1^+ \to 0_1^+)$ value of ^{210}Pb. The calculated result is 2.2 times larger than the experimental one. The calculated $B(E2; 10_1^+ \to 8_1^+)$ values of ^{210}Pb and ^{212}Pb are much

Table 4.4: Comparison of the magnetic dipole moments μ (in μ_N) and the electric quadrupole moments Q (in eb) obtained by the shell model (calc.) to the experimental data (expt.) for Pb isotopes. The experimental data are taken from Refs. [63, 73, 74, 76].

	μ		Q	
^{210}Pb	expt.	calc.	expt.	calc.
2_1^+		-0.360		$+0.021$
4_1^+		-1.026		$+0.035$
6_1^+	$-1.872(90)$	-1.811		-0.104
8_1^+	$-2.496(64)$	-2.551		-0.436
10_1^+		-0.208		-0.678
^{212}Pb	expt.	calc.	expt.	calc.
2_1^+		-0.425		$+0.068$
4_1^+		-1.067		$+0.071$
6_1^+		-1.785		$+0.066$
8_1^+		-2.469		$+0.130$
10_1^+		-0.211		$+0.505$
^{211}Pb	expt.	calc.	expt.	calc.
$5/2_1^+$		-0.910		$+0.034$
$7/2_1^+$		-1.130		$+0.023$
$9/2_1^+$	$-1.4037(8)$	-1.406	$+0.087(62)$	$+0.161$
$11/2_1^+$		$+0.794$		$+0.310$
$13/2_1^+$		-1.786		$+0.211$

smaller than other transition rates among yrast states. The $0_1^+, 2_1^+, \cdots, 8_1^+$ states consist of neutrons in the $1g_{9/2}$ orbital. However, one neutron in the $1g_{9/2}$ orbital needs to be excited to the $0i_{11/2}$ orbital to make the 10_1^+ state. Namely, configurations are changed between the 8_1^+ and 10_1^+ states. Thus the $B(E2; 10_1^+ \to 8_1^+)$ values become small. The $E2$ transition rate from the isomeric $21/2_1^+$ state to the $17/2_1^+$ state in ^{211}Pb, the $B(E2; 21/2_1^+ \to 17/2_1^+)$ value, is well reproduced. As for the magnetic moments, the calculation successfully reproduces the experimental data. As for the quadrupole moments, only that of the $9/2_1^+$ state in ^{211}Pb is measured. The experimental and calculated values are $+0.87(62)$ eb and $+0.161$ eb, respectively. Here the experimental error bar is large.

4.3.2 Bi isotopes

Here $^{210-213}$Bi isotopes are discussed. Figure 4.4 shows the theoretical energy spectra for odd-mass Bi isotopes in comparison with the experimental data [63, 74, 77]. In ^{211}Bi, energy levels of low-lying states are well reproduced. The isomeric $(25/2_1^-)$ state at 1.257 MeV with a half life of 1.4 μs decays to the $(21/2^-)$ state at 1.227 MeV by the $E2$ transition [63]. Both the $25/2_1^-$ and $21/2_1^-$ states consist of the $(\nu g_{9/2}^2 \pi h_{9/2})$ configuration. Here in the $25/2_1^-$ state, spin of two neutrons in the $1g_{9/2}$ orbital is stretched to spin 8. Spin and parity of the experimental state at 0.767 MeV is most likely either $9/2^-$ or

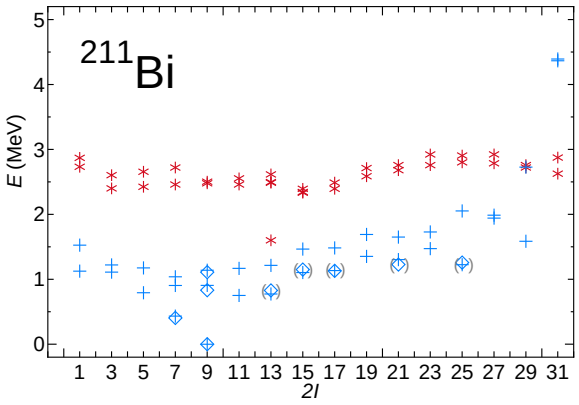

Figure 4.4: Same as fig. 4.2, but for odd-mass Bi isotopes. The experimental data are taken from Refs. [63, 74, 77].

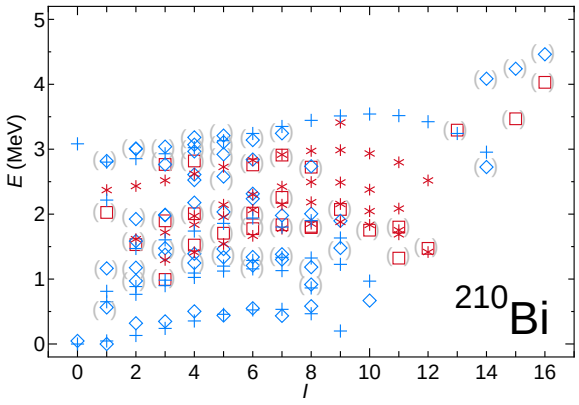

Figure 4.5: Same as fig. 4.2, but for doubly-odd Bi isotopes. The experimental data are taken from Refs. [63, 73, 76].

$11/2^-$ [63]. Spin and parity of the state at 0.767 MeV is inferred as $11/2^-$ since the $11/2^-_1$ state is calculated at 0.751 MeV. The $9/2^-_2$ state, which corresponds to the experimental $9/2^-_2$ state at 0.832 MeV, is calculated at 0.906 MeV. Spin of the negative parity state at 0.793 MeV is not assigned. The $5/2^-_1$ and $7/2^-_2$ states are calculated at 0.793 MeV and 0.905 MeV, respectively. Thus spin of the state at 0.793 MeV is 5/2 in our prediction, although we can not denied a possibility that the spin of this state is 7/2. In ^{213}Bi, spin and parity of only the $9/2^-_1$ and $7/2^-_1$ states is assigned in experiment. The states at 0.593 MeV (possible spin and parity is either $5/2^-$, $7/2^-$, or $9/2^-$) and 0.759 MeV (possible spin and parity is either $5/2^-$ or $13/2^-$) are observed in addition to two assigned states. The $5/2^-_1$ and $13/2^-_1$ states are calculated at 0.618 and 0.733 MeV, respectively. Thus spin and parity of the states at 0.593 MeV and 0.759 MeV are inferred as $5/2^-$ and $13/2^-$, respectively.

Figure 4.5 shows the theoretical energy spectra for doubly-odd Bi isotopes in comparison with the experimental data [63, 73, 76]. ^{210}Bi is a system of one neutron particle and one proton particle with the doubly magic nucleus ^{208}Pb. This nucleus gives us information of the interaction between the neutron and proton. Experimental 15^+_1, 16^+_1, 14^-_2, 15^-_1, and 16^-_1 states cannot be made one neutron in the $1g_{9/2}$, $0i_{11/2}$, $0j_{15/2}$, $2d_{5/2}$, $3s_{1/2}$, $2g_{7/2}$, or $2d_{3/2}$ orbitals and one proton in the $0h_{9/2}$, $1f_{7/2}$, $0i_{13/2}$, $2p_{3/2}$, $1f_{5/2}$, or $2p_{1/2}$ orbitals. Thus these states are beyond the present framework. These states are supposed to be

Table 4.5: Same as table 4.3, but for Bi isotopes. The experimental data are taken from Refs. [63, 73, 74, 76, 77].

	$B(E2)$	
^{211}Bi	expt.	calc.
$7/2_1^- \to 9/2_1^-$	1.07(10)	0.602
$9/2_2^- \to 7/2_1^-$	>0.00015	0.438
$9/2_2^- \to 9/2_1^-$	>0.0031	1.982
$11/2_1^- \to 9/2_1^-$		3.516
$13/2_1^- \to 9/2_1^-$		4.030
$21/2_1^- \to 17/2_1^-$	1.44(11)	3.824
$25/2_1^- \to 21/2_1^-$		1.984
^{213}Bi	expt.	calc.
$7/2_1^- \to 9/2_1^-$		0.862
$9/2_2^- \to 7/2_1^-$		1.722
$9/2_2^- \to 9/2_1^-$		1.893
$11/2_1^- \to 9/2_1^-$		5.601
$13/2_1^- \to 9/2_1^-$		7.775
^{210}Bi	expt.	calc.
$3_1^- \to 1_1^-$		3.487
$3_1^- \to 2_1^-$		0.014
$0_1^- \to 2_1^-$		14.393
^{212}Bi	expt.	calc.
$3_1^- \to 2_1^-$		2.698
$0_1^- \to 2_1^-$		5.178

made by particle-hole excitations across the shell gap. In ^{212}Bi, negative parity states are degenerately observed below 0.5 MeV, which are well reproduced. The lowest members of the 0_1^-, 1_1^-, $\cdots$, 9_1^- states consist of the $(\nu g_{9/2}^3 \pi h_{9/2})$ configuration. The second lowest members of the 1_2^-, 2_2^-, $\cdots$, 8_2^- states consist of the $(\nu g_{9/2}^3 \pi f_{7/2})$ configuration. Positive parity states are calculated above 1.5 MeV.

Calculated results of the $B(E2)$ values, magnetic moments, and quadrupole moments for Bi isotopes are given in Tables 4.5 and 4.6 in comparison with the experimental data [63, 73, 74, 76, 77]. As for $B(E2)$ transition rates, they are measured only in ^{211}Bi. The calculated $B(E2)$ value from the isomeric $25/2_1^-$ state to the $21/2_1^-$ state in ^{211}Bi, the $B(E2; 25/2_1^- \to 21/2_1^-)$ value, is 1.984 W.u. As for magnetic moments, most of experimental values are well reproduced. However, the small experimental magnetic moment of the 1_1^- state in ^{210}Bi is not reproduced. In the nuclei around jj-closed shell, it is known that the core polarization and the pion exchange are important to explain the experimental magnetic moments (e.g. see Refs. [102, 103]). Here, nuclei in which one of the spin-orbit partner $j = \ell + \frac{1}{2}$ is opened are called jj-closed shell nuclei, whereas nuclei in which the spin-orbit partners $j = \ell \pm \frac{1}{2}$ are completely occupied are called LS-closed shell nuclei. The 1_1^- state in ^{208}Bi consists of the $(\nu g_{9/2} \pi h_{9/2})$ configuration. The $0h_{11/2}$

Table 4.6: Same as table 4.3, but for Bi isotopes. The experimental data are taken from Refs. [63, 73, 74, 76, 77].

	μ		Q	
^{211}Bi	expt.	calc.	expt.	calc.
$7/2_1^-$	+4.5(7)	+4.142		−0.630
$9/2_1^-$	(+)3.79(7)	+3.635		−0.695
$11/2_1^-$		+2.721		−0.459
$13/2_1^-$		+2.985		−0.552
^{213}Bi	expt.	calc.	expt.	calc.
$7/2_1^-$		+4.044		−0.778
$9/2_1^-$	+3.717(13)	+3.560	−0.60(5)	−0.856
$11/2_1^-$		+2.803		−0.584
$13/2_1^-$		+3.035		−0.841
^{210}Bi	expt.	calc.	expt.	calc.
1_1^-	−0.04451(6)	+0.217	+0.136(1)	+0.198
5_1^-	+1.530(45)	+1.285		−0.034
7_1^-	+2.114(49)	+1.834		−0.349
9_1^-	2.728(42)	+2.336	−0.471(59)	−0.754
^{212}Bi	expt.	calc.	expt.	calc.
1_1^-	0.41(5)	+0.648	0.1(3)	+0.103
2_1^-		+0.894		+0.238
3_1^-		+0.961		+0.280
5_1^-		+1.256		+0.011
7_1^-		+1.769		−0.464
9_1^-		+2.246		−0.771

orbital, the spin-orbit partner of the $0h_{9/2}$ orbital, is located under the shell gap of the magic number 82, where this orbital is not introduced in the present calculation. One might need to consider the effect of the spin-orbit partner for the explanation of the small experimental magnetic moment of the 1_1^- state in ^{210}Bi.

4.3.3 Po isotopes

Here $^{211-214}$Po isotopes are discussed. Figure 4.6 shows the theoretical energy spectra for even-even Po isotopes in comparison with the experimental data [63, 76, 104–106]. ^{212}Po is a system with two valence neutrons and two valence protons. The narrow energy gap between the 6_1^+ and 8_1^+ states is well reproduced. The I_1^+ ($I = 0, 2, \cdots, 8$) states mainly consist of the $[\nu(g_{9/2}^2)_{I^+}\pi(h_{9/2})_{0^+}^2]$ configuration, whereas the 10_1^+ state consists of the $[\nu(g_{9/2}h_{11/2})_{10^+}\pi(h_{9/2})_{0^+}^2]$ configuration. As will be discussed in Sec. 4.4, these states mainly consist of the configuration mixing of neutrons. This is because the strength of the neutron monopole pairing interaction is weaker than that of protons. In recent years, negative parity states were observed below 2.5 MeV in ^{212}Po [105, 106]. It was found that

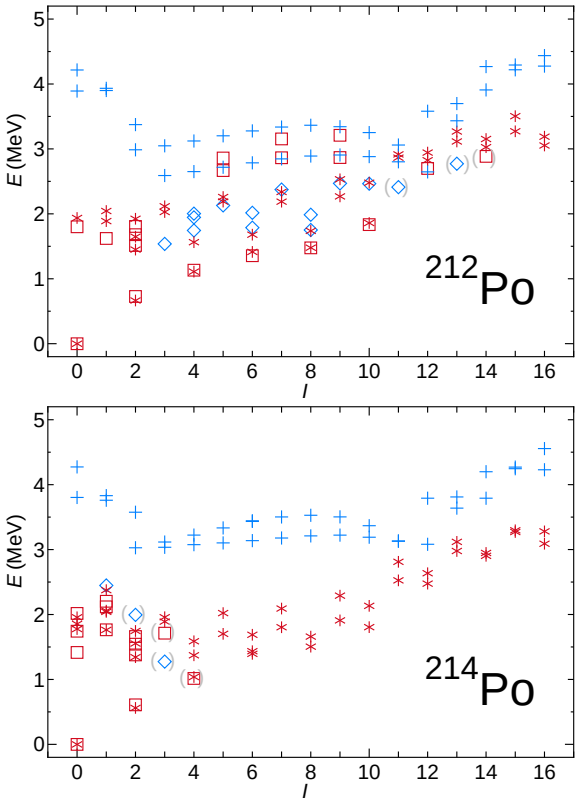

Figure 4.6: Same as fig. 4.2, but for even-even Po isotopes. The experimental data are taken from Refs. [63, 76, 104].

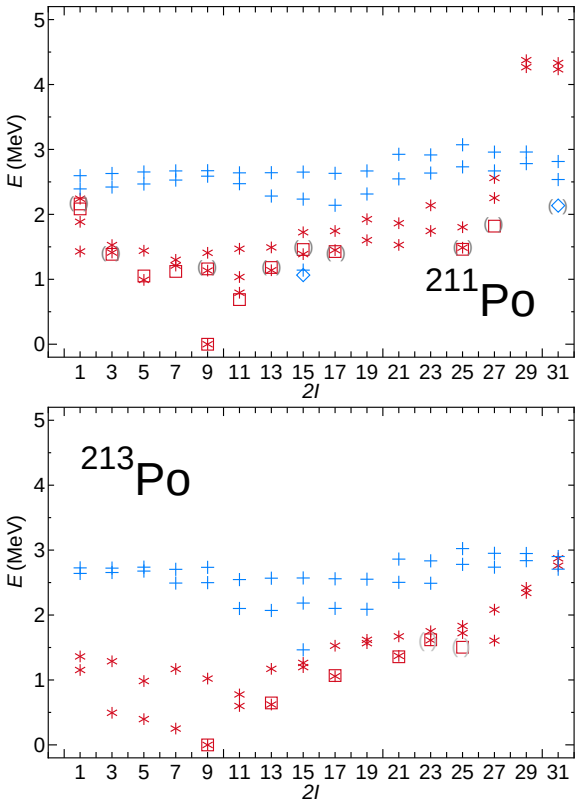

Figure 4.7: Same as fig. 4.2, but for odd-mass Po isotopes. The experimental data are taken from Refs. [63, 74, 77].

the observed 4_1^-, 6_1^-, and 8_1^- states are strongly connected to the corresponding 4_1^+, 6_1^+, and 8_1^+ states by the $E1$ transitions. In Ref. [107], it was suggested that these negative parity states are constructed by the α-particle coupled to the 3_1^- state of ^{208}Pb (the coupled-channels of $\alpha + 3_1^-(^{208}\mathrm{Pb})$. The other description of these negative parity states was suggested in Ref. [108], and they showed a possibility that these negative parity states consist of two-neutron excitations in ^{210}Pb coupled to the collective 3^- state in ^{208}Pb times the ground state in ^{210}Po ($|[J^+(^{210}\mathrm{Pb}) \otimes 3_1^-(^{208}\mathrm{Pb})]_{I^-} \otimes \mathrm{g.s.}(^{210}\mathrm{Po})\rangle$), where J and I indicate angular momenta of states in ^{210}Pb and ^{212}Po, respectively. In our calculation, these negative parity states are not reproduced, thus it is inferred that these states are not constructed by the normal configuration mixing. The negative parity states which are predicted at around 2.5 MeV in our calculation are members of the $(\nu h_{9/2}^2 \pi g_{9/2} i_{13/2})$ configuration.

In ^{214}Po, only the 0_1^+, 2_1^+, and 4_1^+ states are observed in yrast states. The 6_1^+, 8_1^+, and 10_1^+ states are calculated at 1.395, 1.505, and 1.806 MeV, respectively. The state at 1.275 MeV is assigned as (3^-) [110]. This (3^-) state is supposed to be an octupole state [110]. The state at 1.995 MeV which is assigned as (2^-) is also considered to be the coupling state of the octupole state and the quadrupole phonon state since the $E2$ transition rate from the (3^-) state to the (2^-) state is large [110]. In our calculation, negative parity states are calculated above 3.0 MeV. The 3_1^- state calculated at 3.036 MeV

Table 4.7: Same as table 4.3, but for Po isotopes. The experimental data are taken from Refs. [63, 74, 76, 77, 104].

	$B(E2)$	
^{212}Po	expt.	calc.
$2_1^+ \to 0_1^+$		10.806
$4_1^+ \to 2_1^+$		12.966
$6_1^+ \to 4_1^+$	3.9(11)	9.689
$8_1^+ \to 6_1^+$	2.30(9)	3.895
$10_1^+ \to 8_1^+$	2.2(6)	0.138
$10_2^+ \to 8_1^+$		1.218
^{214}Po	expt.	calc.
$2_1^+ \to 0_1^+$		17.583
$4_1^+ \to 2_1^+$		23.208
$6_1^+ \to 4_1^+$		18.290
$8_1^+ \to 6_1^+$		7.825
$10_1^+ \to 8_1^+$		0.560
$0_2^+ \to 2_1^+$	0.159(10)	0.714
^{211}Po	expt.	calc.
$5/2_1^+ \to 9/2_1^+$		10.390
$7/2_1^+ \to 9/2_1^+$		2.401
$9/2_2^+ \to 9/2_1^+$		3.308
$11/2_1^+ \to 9/2_1^+$		0.517
$13/2_1^+ \to 9/2_1^+$		3.882
^{213}Po	expt.	calc.
$5/2_1^+ \to 9/2_1^+$		13.181
$7/2_1^+ \to 9/2_1^+$		14.392
$7/2_1^+ \to 11/2_1^+$		0.333
$11/2_1^+ \to 9/2_1^+$		0.544
$13/2_1^+ \to 9/2_1^+$		12.665

Table 4.8: Same as table 4.4, but for Po isotopes. The experimental data are taken from Refs. [63, 74, 76, 77, 104, 111].

	μ		Q	
^{212}Po	expt.	calc.	expt.	calc.
2_1^+		+0.246		−0.085
4_1^+		−0.096		−0.157
6_1^+		−1.092		−0.326
8_1^+		−2.299		−0.765
10_1^+		−0.080		−1.144
^{214}Po	expt.	calc.	expt.	calc.
2_1^+		+0.273		−0.405
4_1^+		+0.268		−0.703
6_1^+		−0.513		−0.983
8_1^+		−1.939		−0.422
10_1^+		−0.059		−0.988
^{211}Po	expt.	calc.	expt.	calc.
$7/2_1^+$		−0.944		−0.497
$9/2_1^+$	−1.197(85)	−1.344	−0.77(8)	−0.587
$11/2_1^+$		+1.235		−0.616
$13/2_1^+$		+0.893		−0.362
$15/2_1^-$	−0.38(15)	−1.384		−0.759
^{213}Po	expt.	calc.	expt.	calc.
$7/2_1^+$		−0.997		−0.523
$9/2_1^+$		−1.268		−0.394
$11/2_1^+$		+1.152		−0.838
$13/2_1^+$		−1.055		−0.486

is not an octupole state which is associated with the 3_1^- state in ^{208}Pb, and mainly consists of the $(\nu g_{9/2} j_{15/2} \pi h_{9/2}^2)$ configuration.

Figure 4.7 shows the theoretical energy spectra for odd-mass Po isotopes in comparison with the experimental data [63, 74, 77, 91]. Low-lying states are well reproduced in both ^{211}Po and ^{213}Po. The $25/2_1^+$ state at 1.462 MeV in ^{211}Po is an isomer with a half life of 25.2(6) s [74]. This state decays by the α-decay or decays to the $17/2_1^+$ state at 1.428 MeV by the $E4$ transition [74]. The $19/2_1^+$, $21/2_1^+$, and $23/2_1^+$ states, which are easily connected to the $25/2^+$ state by the $E2$ or $M1$ transitions, are not observed. These states are calculated higher in energy than the $25/2_1^+$ state. This isomer is classified as the spin-gap isomer. In ^{213}Po, only positive parity states are observed. The lowest negative parity state, the $15/2_1^-$ state is calculated at 1.464 MeV.

The calculated $B(E2)$ values, magnetic moments, and quadrupole moments for Po isotopes are given in Tables 4.7 and 4.8 in comparison with the experimental data [63, 74, 76, 77, 104, 111]. In ^{212}Po, the calculated $B(E2; 10_1^+ \rightarrow 8_1^+)$ value (0.138 W.u.) is much smaller than the experimental value (2.2(6) W.u.). The $B(E2; 10_1^+ \rightarrow 8_1^+)$ value

was also calculated using a shell model [109]. Their result was 0.002 W.u., which is also quite smaller than the experimental value. The experimental $B(E2; 10_1^+ \to 8_1^+)$ value is of the same order with other transitions among the yrast states. In ^{213}Po, the theoretical calculation predicts large transition rates to the ground $(9/2_1^+)$ state from the $5/2_1^+$, $7/2_1^+$ and $13/2_1^+$ states. The magnetic moment and the quadrupole moment of the $9/2_1^+$ state in ^{211}Po are well reproduced. The measured magnetic moment of the $15/2_1^-$ state in ^{211}Po is $-0.38(15)$ μ_N, whereas that of the calculated value is -1.384 μ_N. In the neighboring nucleus ^{209}Pb, it was suggested that the $15/2_1^-$ state consists of not only the pure $(\nu j_{15/2})$ configuration, but also the $[3_1^-(^{208}\mathrm{Pb}) \otimes \nu g_{9/2}]_{15/2^-}$ configuration [112,113]. Similar to the $15/2_1^-$ state in ^{209}Pb, it is supposed that the $15/2_1^-$ state in ^{211}Po consists of the coupling of the $[\nu j_{15/2} \pi(h_{9/2}^2)_{0^+}]$ and the $[3^-(^{208}\mathrm{Pb}) \otimes \nu g_{9/2}]_{15/2^-}$ configurations. In our calculation, however, the $15/2_1^-$ state in ^{211}Po consists only of the $[\nu j_{15/2} \pi(h_{9/2}^2)_{0^+}]$ configuration. The admixture of the $[3_1^-(^{208}\mathrm{Pb}) \otimes \nu g_{9/2}]_{15/2^-}$ configuration might be necessary for the explanation of the experimental magnetic moment. To study the effect of the $[3_1^-(^{208}\mathrm{Pb}) \otimes \nu g_{9/2}]_{15/2^-}$ configuration to the magnetic moment, the magnetic moment of the $15/2_1^-$ state in ^{209}Pb should be measured.

4.3.4 At isotopes

Here $^{212-215}$At isotopes are discussed. Figure 4.8 shows the theoretical energy spectra for odd-mass At isotopes in comparison with the experimental data [63, 77, 114]. The spin and parity of the state at 0.341 MeV in ^{213}At is most likely either $7/2^-$ or $9/2^-$ [115]. The $7/2_1^-$, $7/2_2^-$, and $9/2_2^-$ states are calculated at 0.239, 0.440, and 0.883 MeV, respectively. Thus our calculation suggests that the spin and parity of the state at 0.341 MeV is $7/2^-$.

The spin and parity of the state at 0.364 MeV in ^{215}At is assigned as $(13/2_1^+)$ [116], whereas the $13/2_1^+$ state is predicted at 1.345 MeV in our calculation. This state mainly consists of the $(\nu g_{9/2}^3 h_{9/2}^2 i_{13/2})$ configuration and the feature of this state is mainly determined by one proton in the $0i_{13/2}$ orbital. The excitation energy of the $13/2_1^+$ state in ^{209}Bi, which indicates the single-particle energy of the proton $0i_{13/2}$ orbital, is 1.609 MeV. The excitation energy of the $13/2_1^+$ state in ^{215}At of 0.364 MeV is quite lower than that in ^{209}Bi. In odd-mass nuclei in this mass region, the effect of the octupole 3^- state for the low-lying single-particle states has been studied [112,113,117,118]. For example, it is suggested the $13/2_1^+$ state in ^{209}Bi consists of the admixture of the pure $(\pi i_{13/2})$ configuration and the $[3_1^-(^{208}\mathrm{Pb}) \otimes \pi f_{7/2}]_{13/2^+}$ configuration [117]. The coupling of the $3_1^-(^{208}\mathrm{Pb})$ state might explain the small excitation energy of the $13/2_1^+$ state in ^{215}At. The coupling of the $3_1^-(^{208}\mathrm{Pb})$ state to the normal configuration mixing state should be investigated much more in a future work.

In ^{215}At, configurations of low-lying states were studied using a shell model [116]. It was suggested that the observed $9/2_1^-$, $5/2_1^-$, $7/2_2^-$, $13/2_1^-$, and $3/2_1^-$ states consist of the $[\nu(g_{9/2})_{0^+}^4 \pi h_{9/2}^3]$ configuration. In that study, only the $1g_{9/2}$ orbital was considered for neutrons. However, our calculation predicts that these states consist of not only neutrons in the $1g_{9/2}$ orbital and protons in the $0h_{9/2}$ orbital, but also nucleons in other high-lying single-particle orbitals. The occupation numbers of the ground state $(9/2_1^-)$ in ^{215}At are calculated as 2.80 and 0.61 for the neutron $1g_{9/2}$ and $0i_{11/2}$ orbitals, respectively, and 2.11 and 0.58 for the proton $0h_{9/2}$ and $1f_{7/2}$ orbitals, respectively.

Figure 4.9 shows the theoretical energy spectra for doubly-odd At isotopes in comparison with the experimental data [63, 76, 104]. The (9_1^-) state in ^{212}At is an isomer with

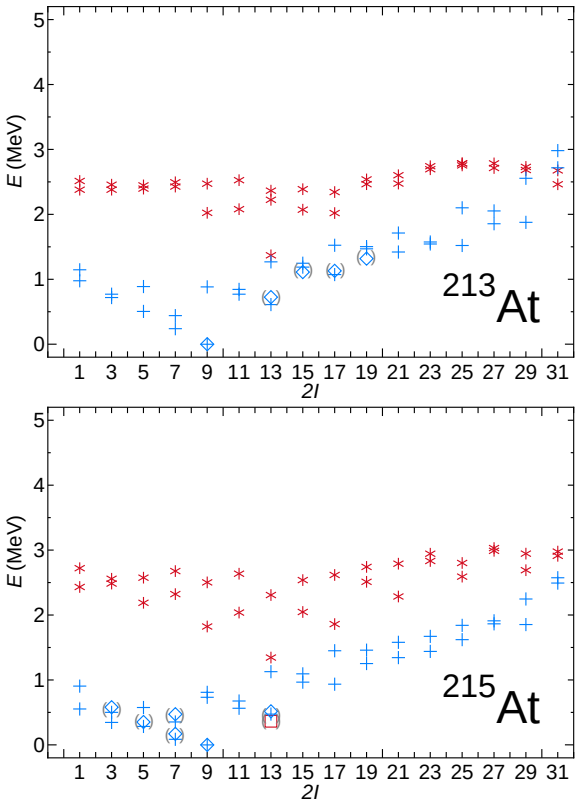

Figure 4.8: Same as fig. 4.2, but for odd-mass At isotopes. The experimental data are taken from Refs. [63, 77, 114].

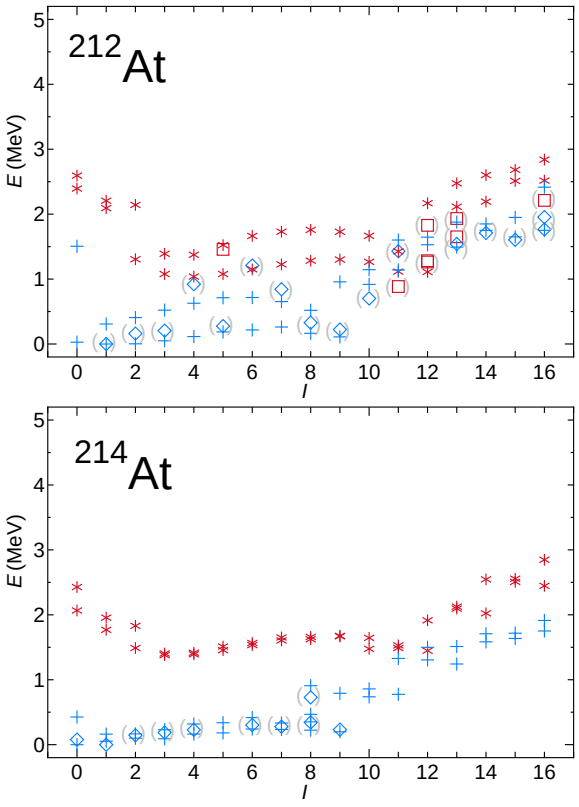

Figure 4.9: Same as fig. 4.2, but for doubly-odd At isotopes. The experimental data are taken from Refs. [63, 76, 104].

a half life of 0.119(3) s [63]. The 0^-_1, 1^-_1, $\cdots$, 9^-_1 states are members of the $(\nu g_{9/2}\pi h^3_{9/2})$ configuration, where two protons in the $0h_{9/2}$ orbital are coupled to 0^+. The calculation represents the situation such that the energy of the 9^-_1 state is lower than that of the 8^-_1 state. The members of the second negative parity band, the 1^-_1, 2^-_1, $\cdots$, 8^-_1 states, consist of the $[\nu g_{9/2}\pi(h_{9/2})^2_{0^+} f_{7/2}]$ configuration. The 11^+_1 state is an isomer with a half life of 18.7(7) ns and decays to the 10^-_1 state by the $E1$ transition [63]. The 11^+_1 state mainly consists of the $[\nu g_{9/2}\pi(h_{9/2})^2_{0^+} i_{13/2}]$ configuration. Our calculation shows that the 10^+, 9^+, $\cdots$ states with the same configuration are located higher than the 11^+_1 state. In ^{214}At, only negative parity states are observed and densely located below 0.5 MeV. These states consist of the $[\nu(g_{9/2}i_{11/2})^3\pi(h_{9/2}f_{7/2})^3]$ configuration.

Calculated results of the $B(E2)$ values, magnetic moments, and quadrupole moments for At isotopes are given in Tables 4.9 and 4.10 in comparison with the experimental data [63, 76, 77, 104, 114]. As for the $E2$ transitions, only two transition rates are measured in these nuclei. The $B(E2; 5^-_1 \to 3^-_1)$ value (3.3(3) W.u. in experiment) and the $B(E2; 15^-_1 \to 13^-_1)$ value (3.1(3) W.u. in experiment) in ^{212}At are calculated as 4.691 and 4.046 W.u., respectively. The calculation predicts large $E2$ transition rates to the ground $9/2^-_1$ state in odd-mass At isotopes (e.g. the $B(E2; 5/2^-_1 \to 9/2^-_1)$ value is calculated as 17.896 W.u. in ^{213}At). As for electromagnetic moments, only magnetic moments of the 15^-_1 and 11^+_1 states in ^{214}At are measured. The measured magnetic moment of the 15^-_1

Table 4.9: Same as table 4.3, but for At isotopes. The experimental data are taken from Refs. [63, 76, 77, 104, 114].

	$B(E2)$	
^{213}At	expt.	calc.
$5/2_1^- \rightarrow 9/2_1^-$		17.896
$7/2_1^- \rightarrow 9/2_1^-$		0.474
$7/2_2^- \rightarrow 9/2_1^-$		14.204
$13/2_1^- \rightarrow 9/2_1^-$		14.706
$15/2_1^- \rightarrow 13/2_1^-$		3.085
$17/2_1^- \rightarrow 13/2_1^-$		18.022
$19/2_1^- \rightarrow 17/2_1^-$		0.684
^{215}At	expt.	calc.
$5/2_1^- \rightarrow 9/2_1^-$		34.399
$7/2_1^- \rightarrow 9/2_1^-$		0.001
$7/2_2^- \rightarrow 9/2_1^-$		17.623
$13/2_1^- \rightarrow 9/2_1^-$		26.698
^{212}At	expt.	calc.
$5_1^- \rightarrow 3_1^-$	3.3(3)	4.691
$8_1^- \rightarrow 9_1^-$		1.895
$15_1^- \rightarrow 13_1^-$	3.1(3)	4.046
^{214}At	expt.	calc.
$3_1^- \rightarrow 1_1^-$		1.916
$5_1^- \rightarrow 3_1^-$		9.258

state is 9.46(8) μ_N and the theoretical result is +7.371 μ_N. The measured magnetic moment of the 11_1^+ state is 5.94(11) μ_N and the theoretical result is +1.886 μ_N, which is 3.1 times smaller than the experimental one. The 11_2^+ state is calculated 0.312 MeV higher than the 11_1^+ state. The magnetic moment of the 11_2^+ state is calculated as +6.069 μ_N. Thus the 11_1^+ and 11_2^+ states might be reversely calculated compared to the experimental states. In our calculation, the 11_1^+ and 11_2^+ states consist of the $[\nu j_{15/2}\pi(h_{9/2}f_{7/2})^3]$ and the $[\nu g_{9/2}\pi(h_{9/2}f_{7/2}i_{13/2})^3]$ configurations, respectively.

4.3.5 Rn isotopes

Here $^{213-216}$Rn isotopes are discussed. Figure 4.10 shows the theoretical energy spectra for even-even Rn isotopes in comparison with the experimental data [63, 104, 119]. The yrast states are well reproduced for both ^{214}Rn and ^{216}Rn. Spin and parity of the state at 1.332 MeV in ^{214}Rn is not assigned. This state decays to the 2_1^+ state at 0.695 MeV. The 2_2^+ state is calculated at 1.563 MeV. Through our calculation and in comparison with neighboring nuclei, the spin and parity of the state at 1.332 MeV is inferred as 2^+. Spin and parity of the state at 1.838 MeV in ^{214}Rn is most likely either 8^+, 9^+, or 10^+. The 8_2^+, 9_1^+, and 10_2^+ states are calculated at 1.820, 2.072, and 2.283 MeV, respectively. Thus our

Table 4.10: Same as table 4.4, but for At isotopes. The experimental data are taken from Refs. [63, 76, 77, 104, 114].

	μ		Q	
^{213}At	expt.	calc.	expt.	calc.
$5/2_1^-$		+2.681		−0.184
$7/2_1^-$		+4.090		−0.793
$9/2_1^-$		+3.662		−0.528
$11/2_1^-$		+3.378		−0.399
$13/2_1^-$		+4.007		−0.573
$15/2_1^-$		+2.642		−0.483
$17/2_1^-$		+3.873		−0.615
$19/2_1^-$		+4.278		−0.821
^{215}At	expt.	calc.	expt.	calc.
$5/2_1^-$		+2.569		−0.421
$7/2_1^-$		+3.961		−1.028
$9/2_1^-$		+3.518		−0.860
$11/2_1^-$		+4.238		−1.069
$13/2_1^-$		+3.831		−1.023
^{212}At	expt.	calc.	expt.	calc.
1_1^-		+0.134		+0.131
2_1^-		+0.394		+0.227
3_1^-		+0.733		+0.192
15_1^-	9.46(8)	+7.371		−0.833
11_1^+	5.94(11)	+1.886		−0.959
11_2^+		+6.069		−1.075
^{214}At	expt.	calc.	expt.	calc.
1_1^-		+0.233		+0.094
2_1^-		+0.565		+0.264
3_1^-		+0.959		+0.431

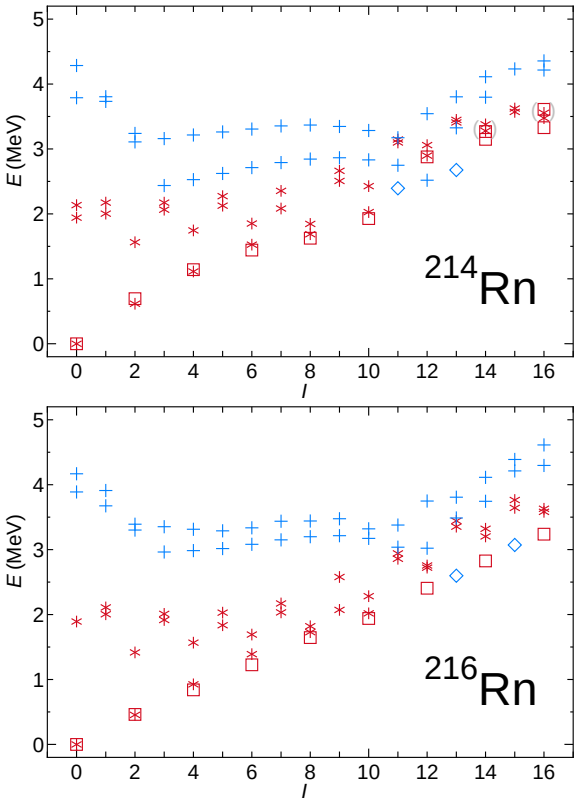

Figure 4.10: Same as fig. 4.2, but for even-even Rn isotopes. The experimental data are taken from Refs. [63, 104, 119].

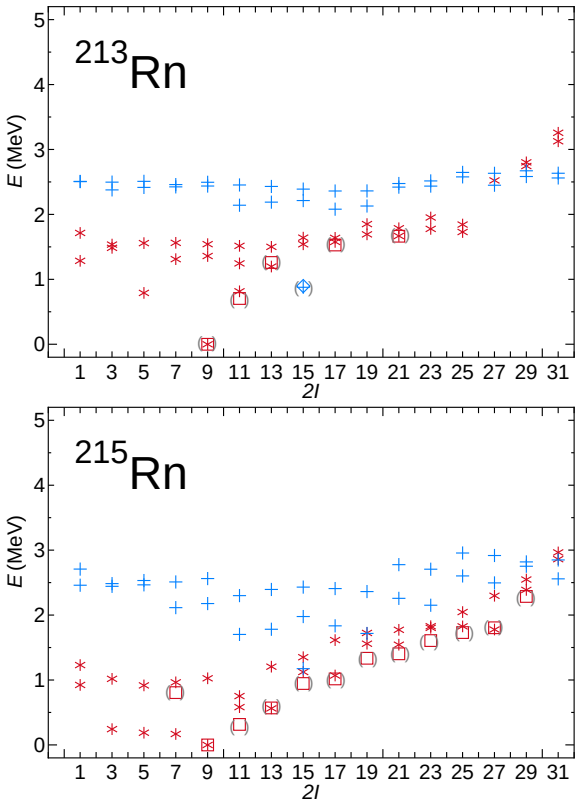

Figure 4.11: Same as fig. 4.2, but for odd-mass Rn isotopes. The experimental data are taken from Refs. [63, 77, 114].

calculation suggests that the spin and parity of the state at 1.838 MeV is 8^+. A specific feature of even-even nuclei in this region is the narrow energy gap between the 6_1^+ and 8_1^+ state. In ^{216}Rn, however, the narrow energy gap between the 6_1^+ and 8_1^+ state is not seen in experiment anymore and the calculation reproduces this feature. As the number of neutrons increases, the narrow energy gap between the 6_1^+ and 8_1^+ states disappears. This feature is discussed later in Sec. 4.4.

Figure 4.11 shows the theoretical energy spectra for odd-mass Rn isotopes in comparison with the experimental data [63, 77, 114]. The yrast states with positive parity are well reproduced. In ^{213}Rn, the $(25/2^+)$ state is observed at least above 1.664 MeV from the ground state. The $25/2_1^+$ state is calculated at 1.729 MeV. The occupation numbers in the main orbitals for the ground state $(9/2_1^+)$ is as follows: for neutrons $\nu 1g_{9/2}$: 0.96, for protons $\pi 0h_{9/2}$: 2.73, $\pi 1f_{7/2}$: 0.72, $\pi 0i_{13/2}$: 0.42. The result suggests that the ground state is not just constructed by protons in the lowest orbital $(0h_{9/2})$ for the proton part. In ^{215}Rn, spin of the positive parity state at 0.214 MeV is most likely either 7/2 or 9/2. Spin of this state is suggested as 7/2 since the $7/2_1^+$ state is calculated at 0.169 MeV. Spin of the negative parity state at 0.291 MeV is most likely either 7/2, 9/2, or 11/2. However, the calculation predicts no negative parity states below 1.0 MeV. The $15/2_1^-$ state, which is not observed in experiment, is calculated at 1.175 MeV.

Calculated results of the $B(E2)$ values, magnetic moments, and quadrupole moments

Table 4.11: Same as table 4.3, but for Rn isotopes. The experimental data are taken from Refs. [63, 77, 104, 114, 119].

	$B(E2)$	
^{214}Rn	expt.	calc.
$2_1^+ \to 0_1^+$	>0.032	18.023
$4_1^+ \to 2_1^+$	>0.28	23.924
$6_1^+ \to 4_1^+$	3.8^{+17}_{-9}	20.273
$8_1^+ \to 6_1^+$	3.3^{+3}_{-1}	10.148
$10_1^+ \to 8_1^+$	2.9(7)	0.602
$12_1^+ \to 10_1^+$	>0.0064	0.008
$14_1^+ \to 12_1^+$		18.93
$16_1^+ \to 14_1^+$	≤4.4(3)	7.412
$18_1^+ \to 16_1^+$	0.71(5)	0.530
$13_1^- \to 11_1^-$	0.93(8)	0.126
^{216}Rn	expt.	calc.
$2_1^+ \to 0_1^+$		27.982
$4_1^+ \to 2_1^+$		39.596
$6_1^+ \to 4_1^+$		38.507
$8_1^+ \to 6_1^+$		20.939
$10_1^+ \to 8_1^+$		2.137
^{213}Rn	expt.	calc.
$7/2_1^+ \to 9/2_1^+$		3.963
$11/2_1^+ \to 9/2_1^+$		0.562
$13/2_1^+ \to 9/2_1^+$		9.081
$17/2_1^+ \to 13/2_1^+$		4.157
$21/2_1^+ \to 17/2_1^+$	1.68(16)	2.155
^{215}Rn	expt.	calc.
$7/2_1^+ \to 9/2_1^+$		22.017
$11/2_1^+ \to 9/2_1^+$		0.271
$13/2_1^+ \to 9/2_1^+$		24.570

Table 4.12: Same as table 4.4, but for Rn isotopes. The experimental data are taken from Refs. [63, 77, 104, 114, 119].

	μ		Q	
^{214}Rn	expt.	calc.	expt.	calc.
2_1^+		+0.421		−0.395
4_1^+		+0.294		−0.561
6_1^+		−0.684		−0.663
8_1^+		−2.018		−0.960
10_1^+		+0.021		−1.391
^{216}Rn	expt.	calc.	expt.	calc.
2_1^+		+0.443		−0.721
4_1^+		+0.616		−1.022
6_1^+		+0.256		−1.194
8_1^+		−1.295		−0.800
10_1^+		+0.089		−1.289
^{213}Rn	expt.	calc.	expt.	calc.
$5/2_1^+$		−1.944		−0.531
$7/2_1^+$		−0.945		−0.438
$9/2_1^+$		−1.293		−0.722
$11/2_1^+$		+0.451		−0.756
$21/2_1^+$	4.73(11)	+3.702		−0.833
$25/2_1^+$	7.63(25)	+5.401		−0.697
$15/2_1^-$		−1.373		−0.833
$31/2_1^-$	9.90(8)	+5.373		−0.847
^{215}Rn	expt.	calc.	expt.	calc.
$7/2_1^+$		−0.803		−0.803
$9/2_1^+$		−1.109		−1.109
$11/2_1^+$		+1.237		+1.237
$13/2_1^+$		−0.681		−0.681

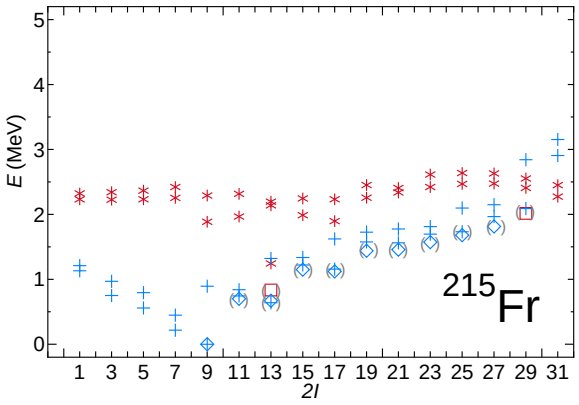

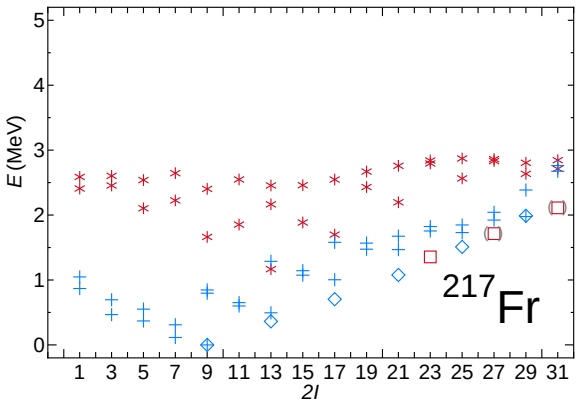

Figure 4.12: Same as fig. 4.2, but for odd-mass Fr isotopes. The experimental data are taken from Refs. [63, 114, 120].

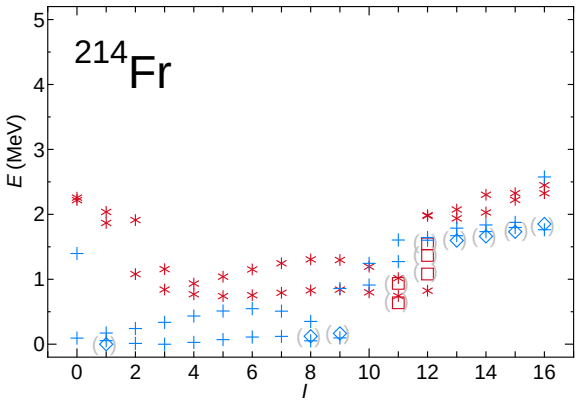

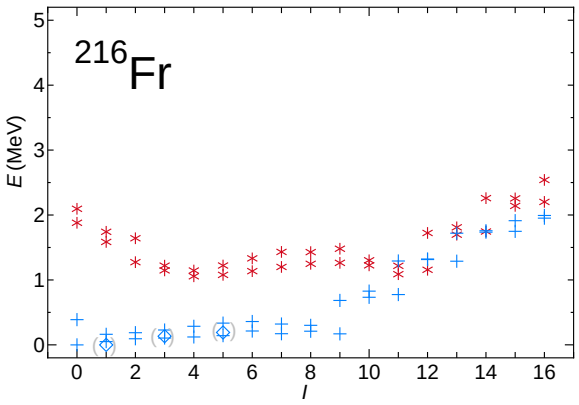

Figure 4.13: Same as fig. 4.2, but for doubly-odd Fr isotopes. The experimental data are taken from Refs. [63, 104, 119].

for Rn isotopes are given in Tables 4.11 and 4.12 in comparison with the experimental data [63, 77, 104, 114, 119]. The calculation predicts large $B(E2)$ values between the yrast states in even-even Rn isotopes. However, the measured $B(E2; 6_1^+ \to 4_1^+)$ and $B(E2; 8_1^+ \to 6_1^+)$ values are much smaller than the experimental values. In ^{214}Rn, the calculated results are 5.5 and 3.1 times larger than the experimental ones, respectively. The theoretical calculation reproduces the magnetic moments well in ^{213}Rn.

4.3.6 Fr isotopes

Here $^{214-217}$Fr isotopes are discussed. Figure 4.12 shows the theoretical energy spectra for odd-mass Fr isotopes in comparison with the experimental data [63, 114, 120]. In ^{215}Fr, energy levels of low-lying negative parity states are well reproduced. The $(13/2_1^+)$ state is observed at 0.835 MeV in experiment. The $13/2_1^+$ state is calculated at 1.224 MeV, which is 0.409 MeV higher than the experimental one.

In ^{217}Fr, spin and parity of the states at 0.209 and 0.275 MeV are not assigned. The $7/2_1^-$, $7/2_2^-$, and $5/2_1^-$ states are calculated at 0.115, 0.310, and 0.369 MeV, respectively. Two of them might correspond to the experimental states at 0.209 and 0.275 MeV. Energies of high-spin states with negative parity are calculated slightly higher than the experimental data. However, the one-to-one correspondence between all calculated states and the experimental data is seen. The $23/2^+$, $27/2^+$, and $31/2^+$ states are observed at

Table 4.13: Same as table 4.3, but for Fr isotopes. The experimental data are taken from Refs. [63, 104, 114].

	$B(E2)$	
^{215}Fr	expt.	calc.
$5/2_1^- \to 9/2_1^-$		18.941
$7/2_1^- \to 9/2_1^-$		0.475
$7/2_2^- \to 9/2_1^-$		22.717
$13/2_1^- \to 9/2_1^-$		18.096
$19/2_1^- \to 15/2_1^-$	0.6(4)	13.691
$19/2_1^- \to 15/2_2^-$		0.018
$23/2_1^- \to 19/2_1^-$	12(5)	8.893
$27/2_1^- \to 23/2_1^-$	1.1(8)	0.392
^{217}Fr	expt.	calc.
$5/2_1^- \to 9/2_1^-$		29.589
$7/2_1^- \to 9/2_1^-$		1.278
$7/2_2^- \to 9/2_1^-$		31.463
$13/2_1^- \to 9/2_1^-$		28.778
^{214}Fr	expt.	calc.
$5_1^- \to 3_1^-$		3.519
$8_1^- \to 9_1^-$		3.978
$15_1^- \to 13_1^-$	0.68(24)	0.073
^{216}Fr	expt.	calc.
$3_1^- \to 1_1^-$		0.467
$5_1^- \to 3_1^-$		6.835

1.355, 1.714, and 2.111 MeV, respectively [121]. In our calculation, $23/2_1^+$, $27/2_1^+$, and $31/2_1^+$ states are calculated at 2.795, 2.832, and 2.845 MeV, respectively, which are much higher than the experimental data. These states might be reproduced by introducing the octupole interaction. Otherwise, parity of these states might be negative. In the neighboring nucleus ^{215}Fr, the $23/2_1^-$, $27/2_1^-$, and $31/2_1^-$ states are observed at energies close to the $21/2_1^-$, $25/2_1^-$, and $29/2_1^-$ states. The $23/2_1^-$, $27/2_1^-$, and $31/2_1^-$ states in ^{217}Fr are calculated at 1.755, 1.923, and 2.675 MeV, respectively.

Figure 4.13 shows the theoretical energy spectra for doubly-odd Fr isotopes in comparison with the experimental data [63,104,119]. In ^{214}Fr, low-lying negative parity states are well reproduced. The (8_1^-) state at 0.122 MeV is a spin-gap isomer with a half life of 3.35(5) ms [63]. The 6_1^-, 7_1^-, and 9_1^- states, which are easily connected to the 8^- state by the $E2$ or $M1$ transitions, are calculated higher in energy than the 8_1^- state. Thus the 8_1^- state disintegrates only by α-decay. In ^{216}Fr, many states are observed below 0.6 MeV. However, spin and parity of these states are not assigned. Spin and parity of only 1_1^-, 3_1^- and 5_1^- states are assigned, which are well reproduced in this calculation. The excitation energy of the (9_1^-) state is unknown. The 9_1^- state is calculated at 0.170 MeV.

Calculated results of the $B(E2)$ values, magnetic moments, and quadrupole moments

Table 4.14: Same as table 4.4, but for Fr isotopes. The experimental data are taken from Refs. [63, 104, 114].

	μ		Q	
^{215}Fr	expt.	calc.	expt.	calc.
$7/2_1^-$		+4.205		−0.652
$9/2_1^-$		+3.694		−0.289
$11/2_1^-$		+3.521		−0.369
$13/2_1^-$		+4.031		−0.446
$19/2_1^-$	3.1(9)	+1.922		−0.692
$23/2_1^-$	3.8(12)	+1.196		−0.969
^{217}Fr	expt.	calc.	expt.	calc.
$7/2_1^-$		+4.066		−0.856
$9/2_1^-$		+3.621		−0.537
$11/2_1^-$		+4.168		−0.956
$13/2_1^-$		+4.057		−0.729
^{214}Fr	expt.	calc.	expt.	calc.
1_1^-		+0.200		+0.130
8_1^-		+2.157		−0.627
9_1^-		+2.474		−0.653
14_1^-	+8.5(4)	+8.091		−1.286
11_1^+	+5.62(7)	+1.917	0.82(22)	−0.902
^{216}Fr	expt.	calc.	expt.	calc.
1_1^-		+0.270		+0.151
3_1^-		+0.873		+0.340
5_1^-		+1.471		−0.059

for Fr isotopes are given in Tables 4.13 and 4.14 in comparison with the experimental data [63, 104, 114]. The experimental $B(E2; 19/2_1^- \rightarrow 15/2_1^-)$ value in ^{215}Fr is 0.6(4) W.u. [114]. The calculated $B(E2)$ value of the same transition is 13.691 W.u., which is 23 times larger than the experimental one. The second $15/2^-$ state is calculated slightly (0.115 MeV) higher than the first $15/2^-$ state. The $B(E2)$ value from the $19/2_1^-$ state to the $15/2_2^-$ state, the $B(E2; 19/2_1^- \rightarrow 15/2_2^-)$ value, is calculated as 0.018 W.u. Therefore, the calculated $15/2_1^-$ and $15/2_2^-$ states might be largely admixed. The measured magnetic moments of the $19/2_1^-$ and $23/2_1^-$ states in ^{215}Fr are 3.1(9) and 3.8(12) μ_N, respectively [114]. The calculated values of the same states are +1.922 and +1.196 μ_N, which are 1.6 and 3.2 times smaller than the experimental values, respectively. The absolute value of the quadrupole moment of the 11_1^+ state in ^{214}Fr is well reproduced. Our calculation suggests that the sign of this value is negative.

4.4 Discussions for nuclei around mass 220

In this section, structure of even-even nuclei is investigated. The expectation numbers of pairs for the yrast states are calculated using the pair-truncated shell model (PTSM) introduced in Sec. 2.4. In this calculation, following two types of noncollective neutron pairs are introduced in addition to the collective S-, D-, and G-pairs:
1. noncollective pair of two neutrons in the $1g_{9/2}$ orbital
2. noncollective pair of one neutron in the $1g_{9/2}$ orbital and one neutron in the $0i_{11/2}$ orbital

Figure 4.14 shows expectation numbers of pairs for the yrast states in ^{212}Po. This nucleus is a system with two neutrons and two protons outside ^{208}Pb. It is seen that the proton part mainly consists of the S-pair for all spins. There are small contributions of the D-pair for all spins, but even the maximum contribution of the D-pair is 0.31 (the 4_1^+ state). The total spin is mainly determined by the neutron part. Up to the 8_1^+ state, the state consists of the $(\nu g_{9/2})^2_{I^+}$ $(I = 0, 2, \cdots, 8)$ configuration. One neutron needs to be excited to the $0i_{11/2}$ orbital to make the 10^+ state since the maximum spin of two neutrons in the $1g_{9/2}$ orbital is eight. Therefore, the 10_1^+ state consists of the $(\nu g_{9/2} i_{11/2})_{10^+}$ configuration. In this mass region, the strength of the neutron monopole-pairing is smaller than that of protons. Thus the configuration mixing of neutrons is preferred.

Figure 4.15 shows expectation numbers of pairs for the yrast states in ^{214}Po. This nucleus is a system with four neutrons and two protons outside ^{208}Pb. Similar to ^{212}Po, the proton part mainly consists of the S-pair for all spins. For the neutron part, the 0_1^+ state consists of two neutron S-pairs. For the 2_1^+, 6_1^+, 8_1^+, and 10_1^+ states, two neutrons are coupled to the S-pair and two neutrons are coupled to the state with spin I. For the 2_1^+ state, the expectation numbers of the neutron D-pair and the proton D-pair are 0.825 and 0.318, respectively, which means that the state with spin two mainly consists of the neutron D-pair. For the 4_1^+ state, the expectation numbers of the neutron D-pair, the neutron D-pair, and the proton D-pair are 0.788, 0.425, and 0.318, respectively. Namely, it is inferred that the state with spin four consists of mixture of two types of pair structures. The first one is the pair structure which consists of one neutron S-pair, one neutron D-pair, and one proton D-pair which coupled to spin four $[S_\nu(D_\nu D_\pi)_{4^+}]$. The second one is the pair structure which consists of one neutron S-pair, one neutron G-pair, two proton S-pairs $(S_\nu G_\nu S_\pi)$.

Figure 4.16 shows expectation numbers of pairs for the yrast states in ^{214}Rn. This nucleus is a system with two neutrons and four protons outside ^{208}Pb. For all spins, four protons are coupled to the S-pairs and spins are mainly determined by the neutron part. Similar to ^{212}Po, yrast states consist of the $(\nu g_{9/2})^2_{I^+}$ configuration up to the 8_1^+ state and the 10_1^+ state consists of the $(\nu g_{9/2} i_{11/2})_{10^+}$ configuration.

Figure 4.17 shows expectation numbers of pairs for the yrast states in ^{216}Rn. This nucleus is a system with for neutrons and four protons outside ^{208}Pb. Similar to other even-even nuclei in this mass region, the 0_1^+ state consists of two neutron S-pairs and two proton S-pairs and the 2_1^+ state mainly consists of one neutron S-pair, one neutron D-pair, and two proton S-pairs. For the 4_1^+ state, the expectation numbers of the neutron D-pair, the neutron D-pair, and the proton D-pair are 0.881, 0.303, and 0.551, respectively. The 4_1^+ state has a similar structure with the 4_1^+ state in ^{214}Po. The structure of the 6_1^+ state, however, is different from even-even nuclei in this mass region. The expectation numbers

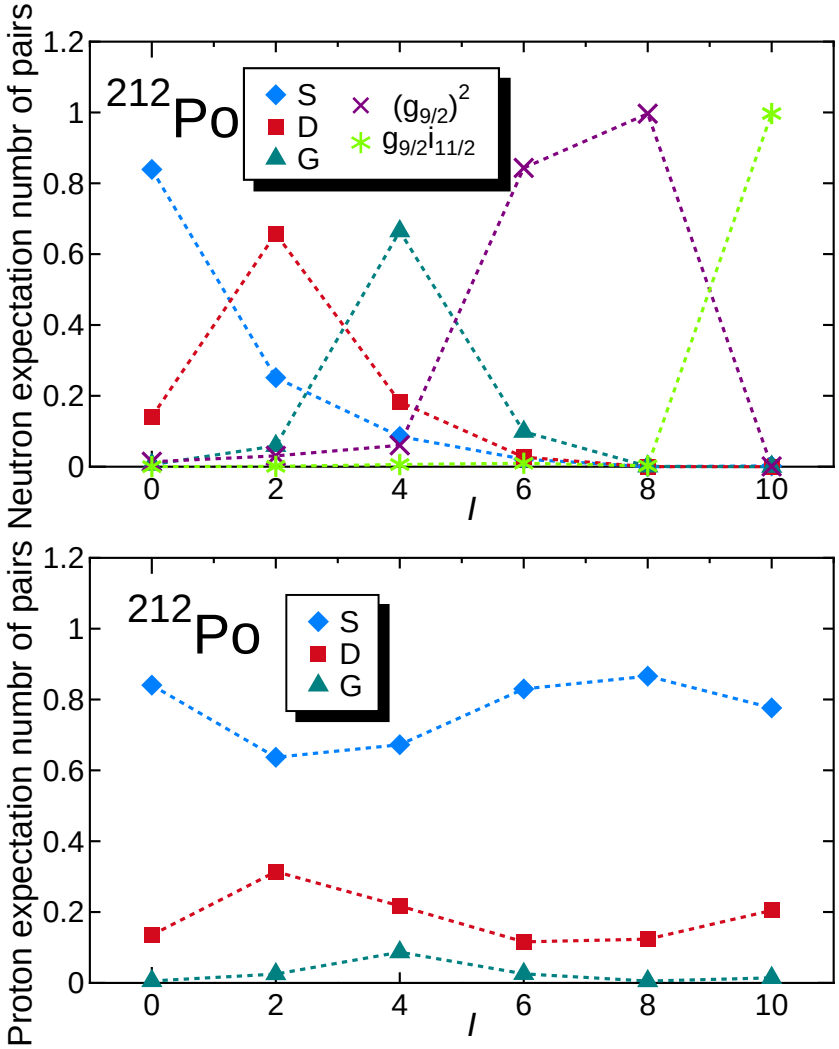

Figure 4.14: The upper panel shows the neutron expectation number of pairs for ^{212}Po. The S, D, and G indicate S-pair, D-pair, and G-pair, respectively. As for noncollective pairs, $(g_{9/2})^2$-pair $[(g_{9/2})^2]$ and $g_{9/2}i_{11/2}$-pair $(g_{9/2}i_{11/2})$ are introduced. The detailed of noncollective pairs are written in the text. The lower panel shows the proton expectation number of pairs for ^{212}Po.

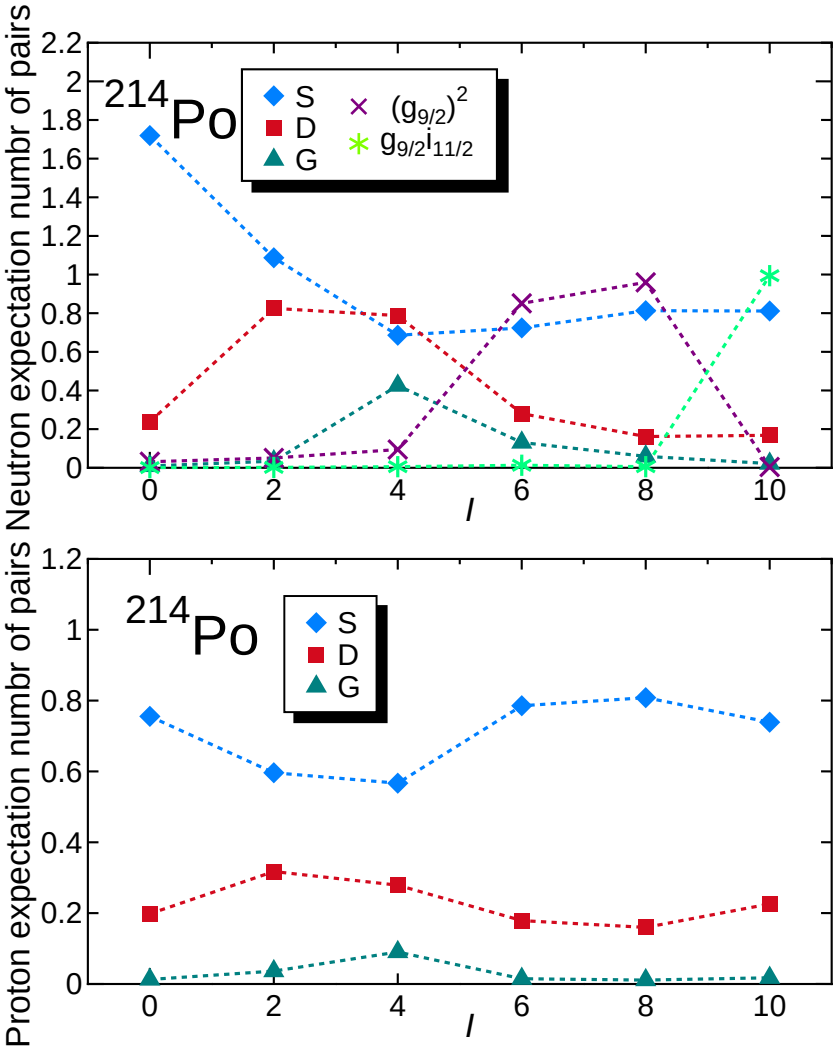

Figure 4.15: The same as Fig. 4.14, but for ^{214}Po.

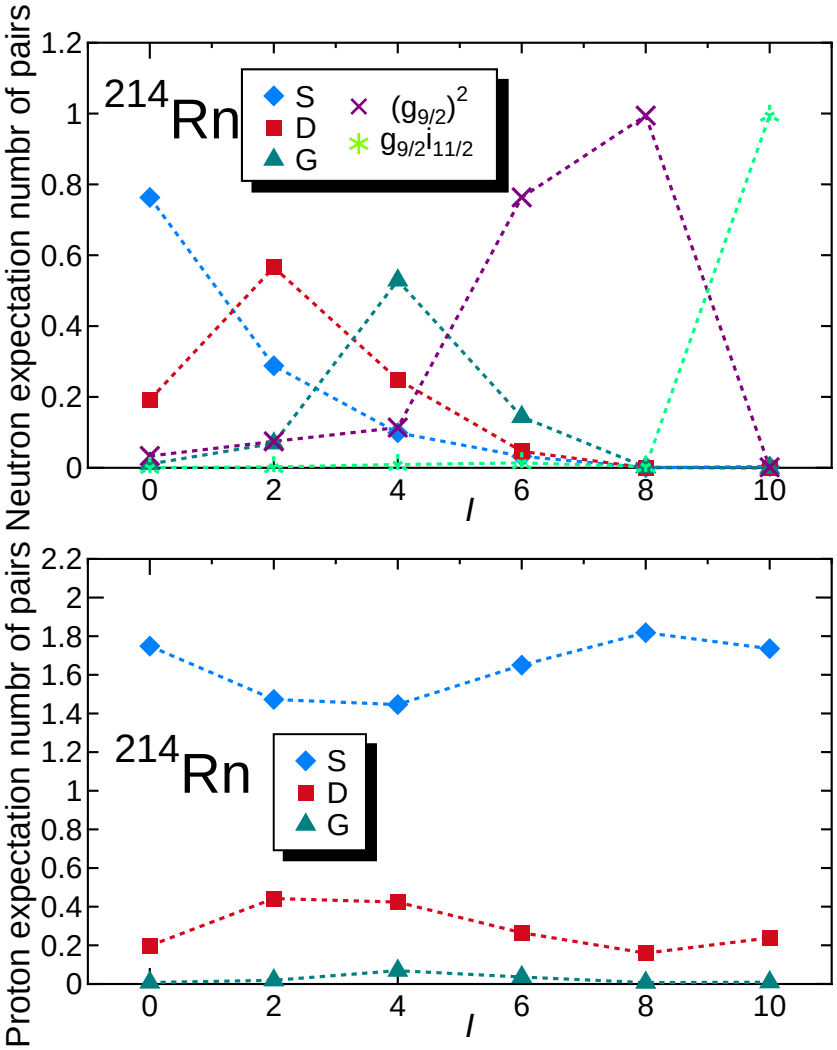

Figure 4.16: The same as Fig. 4.14, but for ^{214}Rn.

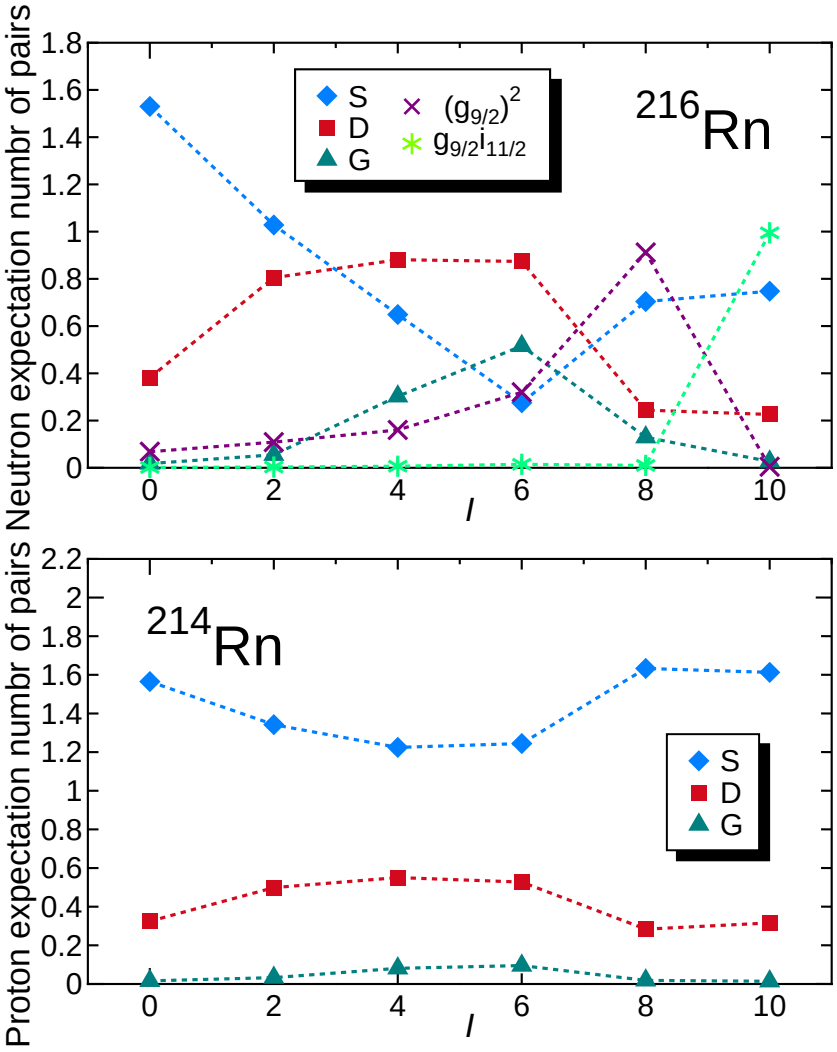

Figure 4.17: The same as Fig. 4.14, but for ^{216}Rn.

of the neutron D-pair, the neutron G-pair, and the neutron $(g_{9/2})^2_{6^+}$-pair are 0.874, 0.516, and 0.320, respectively. The expectation number of the neutron $(g_{9/2})^2_{6^+}$-pair is small and that of the neutron D-pair is large compared to other even-even nuclei in this mass region. This indicates that the nucleus shows an aspect of a collective feature. The low-lying nuclear structure of nuclei with few nucleons outside a doubly magic nucleus is generally determined by independent motions of several nucleons outside a doubly magic nucleus. However, as the number of valence nucleons increases, a collective feature appears. The collectivity of ^{216}Rn is also seen in the energy spectrum as discussed in Sec. 4.3.5. The specific feature of even-even nuclei in this mass region is the narrow energy gap between the 6^+_1 and 8^+_1 states (e.g. see ^{210}Pb in Fig. 4.2). This small energy gap occurs due to the alignment of two neutrons in the $1g_{9/2}$ orbital. In this mass region, the yrast states up to the 8^+_1 state consist of the two neutrons in the $1g_{9/2}$ orbital. In the 8^+_1 state, spin of two neutrons in the $1g_{9/2}$ orbital is stretched and the energy of the 8^+_1 state is lowered. However, the narrow energy gap between the 6^+_1 and 8^+_1 states is not seen in ^{216}Rn anymore (see Fig. 4.10).

Chapter 5

Summary

In this thesis, the systematic study has been performed for even-even, odd-mass, and doubly-odd nuclei which have more than 82 protons around ^{208}Pb using the large-scale shell-model. Nuclei which have less than 126 neutrons (nuclei around mass 210) and nuclei which have more than 126 neutrons (nuclei around mass 220) have been studied. For nuclei around mass 210, structure of $^{203-206}$Pb, $^{204-208}$Bi, $^{205-210}$Po, $^{206-211}$At, $^{207-212}$Rn, and $^{208-213}$Fr nuclei has been studied. For nuclei around mass 220, structure of $^{210-212}$Pb, $^{210-213}$Bi, $^{211-214}$Po, $^{212-215}$At, $^{213-216}$Rn, and $^{214-217}$Fr nuclei has been studied.

In the shell-model framework, we have adopted a method of diagonalization where firstly the neutron and the proton systems are separately diagonalized and secondly the neutron-proton system is diagonalized. By cutting off dimensions of the neutron and proton systems, it is now possible to treat nuclei which are far from the doubly-magic core by the shell-model approach. The validity of this method has been checked to be confirmed that this method is efficient and useful.

As for the model space of the shell-model calculations, for nuclei around mass 210, all the six orbitals in the major shell between the magic numbers 82 and 126 ($0h_{9/2}$, $1f_{7/2}$, $0i_{13/2}$, $2p_{3/2}$, $1f_{5/2}$, and $2p_{1/2}$) have been taken for both neutrons and protons. For nuclei around mass 220, seven single-particle orbitals above the magic number 126 ($1g_{9/2}$, $0i_{11/2}$, $0j_{15/2}$, $2d_{5/2}$, $3s_{1/2}$, $2g_{7/2}$, and $2d_{3/2}$) have been taken for neutrons and six orbitals in the major shell between the magic numbers 82 and 126 ($0h_{9/2}$, $1f_{7/2}$, $0i_{13/2}$, $2p_{3/2}$, $1f_{5/2}$, and $2p_{1/2}$) have been taken for protons. The linear particle number dependences on the $\nu 0j_{15/2}$, $\nu 0i_{13/2}$, $\pi 1f_{7/2}$, and $\pi 0i_{13/2}$ single-particle energies have been assumed. These particle number dependences have been introduced for a better description of energy levels. As for the effective two-body interaction, the phenomenological interaction which consists of the pairing plus quadrupole-quadrupole and multipole interactions has been employed. Only one set of the strengths has been assumed for each mass region. The additional interaction with spin 8 (the MP-8 interaction) has been introduced between the proton $0h_{9/2}$ and $0f_{7/2}$ orbitals for the proton part.

The energy spectra, $E2$ transition rates, magnetic moments, and quadrupole moments have been calculated and compared with the experimental data. Good agreements with the experimental data have been obtained not only for even-even nuclei, but also for odd-mass and doubly-odd nuclei.

The systematic feature of each mass region and specific features of each nucleus have been investigated. In particular, structure and configurations of isomeric states have been analyzed in detail. The effects of the particle number dependence for single-particle

energies on energy spectra have been discussed. It has been found that the nuclear structure is well reproduced by introducing the particle number dependence on the single-particle energies. It is known that the single-particle energies are shifted by the monopole and tensor interactions in nuclei in light mass regions. In this thesis we have not introduced monopole and tensor interactions and phenomenologically varied single-particle energies. As for a future study, it is necessary to introduce the monopole and/or tensor interactions in nuclei with medium and heavy mass region. Also the effect of the MP-8 interaction has been investigated. It has been found that the introduction of the MP-8 interaction is meaningful. However, the origin of the MP-8 interaction has not been revealed. The necessity of other kinds of interactions for low-lying states has been discussed. It has been found that the hexadecapole interaction between neutrons and protons is necessary for a better description of low-lying negative parity states in ^{208}Bi.

In this thesis, we have found the following phenomenon; the calculated magnetic moment of a state agrees with the experimental data, but the quadrupole moment of the same state does not agree with the experimental data. The reason why this phenomenon occurs has been studied and two possibilities of explaining this phenomenon have been presented; the mixing of two wavefunctions and a difference in the effective charge of each orbital. This phenomenon should be investigated more in future.

Acknowledgments

First of all, I would like to express my sincere gratitude to my supervisor, Prof. N. Yoshinaga. Thanks to his patient, precise, and thoughtful direction, I was able to finish writing my thesis. I also greatly thank to Prof. K. Higashiyama for significant advices and discussions. Further I would like to thank Prof. A. Odahara, Prof. T. Shimoda, and Prof. A. Umeya for helpful discussions, and also Prof. K. Asahi, and Dr. K. Yamanaka regarding the study of the electric dipole moment. I also thank all members of our group. This work is supported by Grant-in-Aid for Japan Society for the Promotion of Science (JSPS) Fellows Grant Number 2610429.

List of publications

1. E. Teruya, N. Yoshinaga, K. Higashiyama, and K. Asahi, *Effects of particle-hole excitations to nuclear Schiff moments in Xe isotopes*, to be published for Physical Review C.

2. A. Vogt, B. Birkenbach, P. Reiter, A. Blazhev, M. Siciliano, K. Hadyńska-Kek, J. J. Valiente-Dobón, C. Wheldon, E. Teruya, N. Yoshinaga, *et. al*, *Isomers and high-spin structures in the $N = 81$ isotones ^{135}Xe and ^{137}Ba*, Physical Review C **95**, 024316 (2017).

3. E. Teruya, N. Yoshinaga, K. Higashiyama, H.Nishibata, A. Odahara, and T. Shimoda, *Large-scale shell-model study of the newly found isomer in ^{136}La*, Physical Review C **94**, 014317 (2016).

4. E. Teruya, N. Yoshinaga, and K. Higashiyama, *Large-scale shell-model calculation of nuclei around mass 210*, Physical Review C **93**, 064327 (2016).

5. E. Teruya, N. Yoshinaga, K. Higashiyama, and A. Odahara, *Shell-model calculations of nuclei around mass 130*, Physical Review C **92**, 034320 (2015).

6. K. Higashiyama, N. Yoshinaga, and E. Teruya, *Generator coordinate method analysis of Xe and Ba isotopes*, JPS Conference Proceedings 6, 030050 (2015).

7. E. Teruya, N. Yoshinaga, and K. Higashiyama, *Shell model estimate of electric dipole moments for Xe isotopes*, JPS Conference Proceedings 6, 030069 (2015).

8. N. Yoshinaga, K. Higashiyama, D. Taguchi and E. Teruya, *Neutrinoless double beta nuclear matrix elements around mass 80 in the nuclear shell-model*, EPJ Web of Conferences 93, 01055 (2015).

9. N. Yoshinaga, K. Higashiyama, D. Taguchi and E. Teruya, *Neutrinoless Double Beta Nuclear Matrix Elements Around Mass 80 in the Nuclear Shell Model*, JPS Conf. Proc. 6, 030072 (2015).

10. E. Teruya, N. Yoshinaga and K. Higashiyama, *Shell model estimate of electric dipole moments in medium and heavy nuclei*, EPJ Web of Conferences 93, 01008 (2015).

11. N. Yoshinaga, K. Higashiyama, R. Arai, and E. Teruya, *Nuclear electric dipole moments for the lowest $1/2^+$ states in Xe and Ba isotopes*, Physical Review C **89**, 045501 (2014).

12. E. Teruya, N. Yoshinaga, and K. Higashiyama, *Shell model estimate of electric dipole moments in medium and heavy nuclei*, EPJ Web of Conferences 66, 05023 (2014).

13. N. Fotiades, J. A. Cizewski, K. Higashiyama, N. Yoshinaga, E. Teruya, R. Krucken, R. M. Clark, P. Fallon, I. Y. Lee, A. O. Macchiavelli, and W. Younes, *Medium-spin states in* ^{135}Cs, Physical Review C **88**, 064315 (2013).

14. N. Yoshinaga, K. Higashiyama, R. Arai, and E. Teruya, *Nuclear Schiff moments for the lowest* $1/2^+$ *states in Xe isotopes*, Physical Review C **87**, 044332 (2013).

Presentations at academic conferences

Oral presentations

1. E. Teruya, N. Yoshinaga, and K. Higashiyama, *Shell model calculations of nuclei around ^{208}Pb*, International Nuclear Physics Conference INPC2016, Adelaide, Australia, September 2016.

2. E. Teruya, N. Yoshinaga and K. Higashiyama, *Shell model calculations of nuclei around mass 200*, Computational Advances in Nuclear and Hadron Physics CANHP2015, Kyoto University, Kyoto, Japan, October 2015.

3. E. Teruya, N. Yoshinaga and K. Higashiyama, *Estimation of Schiff moments using the nuclear shell model*, Bulletin of the American Physical Society 4th Joint Meeting of the APS Division of Nuclear Physics and the Physical Society of Japan, Hawaii, USA, October 2014.

4. E. Teruya, N. Yoshinaga, and K. Higashiyama, *Shell model estimate of electric dipole moments in medium and heavy nuclei*, Fifteenth International Symposium on Capture Gamma-Ray Spectroscopy and Related Topics CGS15, Dresden, Germany, August 2014.

Poster presentations

1. E. Teruya, N. Yoshinaga, K. Higashiyama, *Theoretical estimation of the nuclear Schiff moment*, 9th International conference on Fundamental Physics Using Atoms FPUA 2017, Kyoto University, Kyoto, Japan, January 2017.

2. E. Teruya, N. Yoshinaga, K. Higashiyama, *Shell model estimate of nuclear Schiff moments fo Xe isotopes*, 8th International conference on Fundamental Physics Using Atoms FPUA 2015, Riken, Saitama, Japan, November 2015.

3. E. Teruya, N. Yoshinaga, K. Higashiyama, *Shell model estimate of electric dipole moments for Xe isotopes*, Advances in Radioactive Isotopes Science ARIS2014, University of Tokyo, Tokyo, Japan, June 2014.

4. E. Teruya, N. Yoshinaga, K. Higashiyama, *Shell model estimate of Schiff moments in Xe isotopes*, 7th International conference on Fundamental Physics Using Atoms FPUA 2014, Miraikan, Tokyo, Japan, March 2014.

5. E. Teruya, N. Yoshinaga, K. Higashiyama, *Shell model estimate of electric dipole moment in medium and heavy nuclei*, International Nuclear Physics Conference INPC2013, Firenze, Italy, June 2013.

Presentations at the physical society of Japan

1. 照屋絵理，吉永尚孝，東山幸司，原子核シッフモーメントの理論的評価，日本物理学会第 72 回年次大会，大阪大学，2017 年 3 月
2. 照屋絵理，吉永尚孝，東山幸司，^{208}Pb 周辺核の八重極相関，日本物理学会第 2016 回年次大会，宮崎大学，2016 年 9 月
3. 照屋絵理，吉永尚孝，東山幸司，^{208}Pb 周辺核の殻模型計算，日本物理学会第 71 回年次大会，東北学院大学，2016 年 3 月
4. 照屋絵理，吉永尚孝，東山幸司，殻模型を用いた質量数 200 領域の解析，日本物理学会 2015 年秋季大会，大阪市立大学，2015 年 9 月
5. 照屋絵理，吉永尚孝，東山幸司，コアの励起を考慮した原子核のシッフモーメント，日本物理学会第 70 回年次大会，早稲田大学，2015 年 3 月
6. 照屋絵理，吉永尚孝，東山幸司，殻模型によるシッフモーメントの評価，日本物理学会第 69 回年次大会，東海大学，2014 年 3 月
7. 照屋絵理，吉永尚孝，東山幸司，Xe アイソトープのシッフモーメント，日本物理学会 2013 年秋季大会，高知大学，2013 年 9 月
8. 照屋絵理，吉永尚孝，東山幸司，質量数 130 領域における高スピン状態の殻模型計算，日本物理学会第 68 回年次大会，広島大学，2013 年 3 月

Others

1. 照屋絵理，　殻模型による ^{208}Pb 周辺核の構造解析，研究会：クラスター・平均場の両側面からみる原子核構造の多様性とそのダイナミクス，大阪市立大学，2017 年 1 月

Appendix A

Hamiltonian

A.1 Matrix elements of two-body shell-model interactions

Here we explicitly give the two-body matrix elements $\langle i_1 i_2; J|\hat{H}|i_3 i_4; J\rangle$ for two-body interactions between like nucleons in terms of their interaction strengths. Here in generic $i_k, (k = 1, 2, 3, 4)$ represents isotropic harmonic oscillator quantum numbers (n, ℓ, j) with spin degrees of freedom. The matrix element $\langle i_1 i_2; J|\hat{H}|i_3 i_4; J\rangle$ is evaluated between the normalized, but not antisymmetrized wavefunctions $|i_1 i_2; J\rangle$ and $|i_3 i_4; J\rangle$. The antisymmetrized matrix element should be calculated as

$$\begin{aligned}\langle i_1 i_2; J|\hat{H}|i_3 i_4; J\rangle_A &= \frac{1}{4}\Big[\langle i_1 i_2; J|\hat{H}|i_3 i_4; J\rangle \\ &\quad -(-1)^{i_1+i_2-J}\langle i_2 i_1; J|\hat{H}|i_3 i_4; J\rangle \\ &\quad -(-1)^{i_3+i_4-J}\langle i_1 i_2; J|\hat{H}|i_4 i_3; J\rangle \\ &\quad +(-1)^{i_1+i_2+i_3+i_4}\langle i_2 i_1; J|\hat{H}|i_4 i_3; J\rangle\Big]. \end{aligned} \tag{A.1}$$

In the following two-body matrix elements are given term by term:

The monopole pairing interaction, $\hat{H} = -G_0\hat{P}^{\dagger(0)}\hat{P}^{(0)}$, becomes

$$\langle i_1 i_2; J|\hat{H}|i_3 i_4; J\rangle = -G_0\delta_{J0}\sqrt{\left(j_1+\frac{1}{2}\right)\left(j_3+\frac{1}{2}\right)}\delta_{i_1 i_2}\delta_{i_3 i_4}. \tag{A.2}$$

The quadrupole-pairing interaction, $\hat{H} = -G_2\hat{P}^{\dagger(2)}\cdot\hat{\tilde{P}}^{(2)}$, becomes

$$\langle i_1 i_2; J|\hat{H}|i_3 i_4; J\rangle = -4G_2\delta_{J2}\frac{1}{\sqrt{(1+\delta_{i_1 i_2})(1+\delta_{i_3 i_4})}}Q^{(2)}_{i_1 i_2}\cdot Q^{(2)}_{i_3 i_4}. \tag{A.3}$$

Here the matrix element $Q^{(2)}_{i_1 i_2}$ is given by

$$Q^{(2)}_{i_1 i_2} = \langle n_1\ell_1|r^2|n_2\ell_2\rangle T, \tag{A.4}$$

with

$$T = -\sqrt{\frac{2j_2+1}{4\pi}}(j_2\tfrac{1}{2}20|j_1\tfrac{1}{2})(-1)^{j_2-j_1}\frac{(-1)^{\ell_1+\ell_2}+1}{2}. \tag{A.5}$$

Here the phase convention $(-1)^{n_1+n_2}$ is adopted for the calculation of $\langle n_1\ell_1|r^2|n_2\ell_2\rangle$.

The quadrupole-quadrupole interaction, $\hat{H} = -\kappa\hat{Q}\cdot\hat{Q}$, becomes

$$\langle i_1 i_2; J|\hat{H}|i_3 i_4; J\rangle = \frac{-20\kappa(-1)^{j_2+j_3}}{\sqrt{(1+\delta_{i_1 i_2})(1+\delta_{i_3 i_4})}} \left\{ \begin{array}{ccc} j_1 & j_4 & 2 \\ j_3 & j_2 & J \end{array} \right\} Q^{(2)}_{i_1 i_4}\cdot Q^{(2)}_{i_2 i_3}, \tag{A.6}$$

where $\left\{ \begin{array}{ccc} j_1 & j_4 & 2 \\ j_3 & j_2 & J \end{array} \right\}$ represents a six-j coefficient.

The multipole-pairing interaction, $\hat{H} = -G_K \hat{P}^{\dagger(K)}\cdot\hat{\tilde{P}}^{(K)}$ $(K = 4, 6, 8, 10)$, becomes

$$\langle i_1 i_2; J|\hat{H}|i_3 i_4; J\rangle = -4G_K\delta_{JK}\frac{1}{\sqrt{(1+\delta_{i_1 i_2})(1+\delta_{i_3 i_4})}} Q^{(K)}_{i_1 i_2}\cdot Q^{(K)}_{i_3 i_4}. \tag{A.7}$$

The matrix element $Q^{(K)}_{i_1 i_2}$ $(K = 4, 6, 8, 10)$ is given by

$$Q^{(K)}_{i_1 i_2} = -\sqrt{\frac{2j_2+1}{4\pi}}(-1)^{n_1+n_2+j_2-j_1}(j_2\tfrac{1}{2}K0|j_1\tfrac{1}{2})\frac{(-1)^{\ell_1+\ell_2}+1}{2}. \tag{A.8}$$

Here $\langle n_1\ell_1|r^K|n_2\ell_2\rangle = (-1)^{n_1+n_2}$ is employed for simplicity. Namely, no radial dependence is considered except for the phase dependence. Detailed derivations of two-body matrix elements are given in the following Section.

A.2 Derivation of the shell model Hamiltonian

A.2.1 Quadrupole-pairing interaction

We define the creation operator of the quadrupole pairing interaction as $\hat{P}^{\dagger(2)}_M = \sum_{ij} Q_{ij}\left[c^\dagger_i c^\dagger_j\right]^{(2)}_M$. The annihilation operator of the quadrupole pairing interaction is given as follows,

$$\begin{aligned}
\hat{P}^{(2)}_M &= \left(\hat{P}^{\dagger(2)}_M\right)^\dagger = \left(\sum_{ij} Q_{ij}\left[c^\dagger_i c^\dagger_j\right]^{(2)}_M\right)^\dagger \\
&= \sum_{i\mu j\nu} Q_{ij}(i\mu j\nu|2M)c_{j\nu}c_\mu \\
&= \sum_{i\mu j\nu} Q_{ij}(i\mu j\nu|2M)(-1)^{j+\nu}\tilde{c}_{j-\nu}(-1)^{i+\mu}\tilde{c}_{j-\mu} \\
&= \sum_{i\mu j\nu} Q_{ij}(i-\mu j-\nu|2M)(-1)^{j-\nu}\tilde{c}_{j\nu}(-1)^{i-\mu}\tilde{c}_{j\mu} \\
&= \sum_{i\mu j\nu} Q_{ij}(i\mu j\nu|2-M)(-1)^{i+j-M}\tilde{c}_{j\nu}\tilde{c}_{j\mu} \\
&= \sum_{i\mu j\nu} Q_{ij}(-1)^{i+j-M}\left[\tilde{c}_j\tilde{c}_j\right]^{(2)}_{-M} \\
&= -\sum_{i\mu j\nu} Q_{ij}(-1)^{M}\left[\tilde{c}_j\tilde{c}_j\right]^{(2)}_{-M}.
\end{aligned} \tag{A.9}$$

The quadrupole pairing interaction, $\sum_M \hat{P}^{\dagger(2)}_M \hat{P}^{(2)}_M$, is written as

$$\begin{aligned}\sum_M \hat{P}^{\dagger(2)}_M \hat{P}^{(2)}_M &= \sum_M \hat{P}^{\dagger(2)}_M (-1)\hat{\tilde{P}}^{(2)}_M \\ &= \left(\hat{P}^{\dagger(2)}_M \cdot \hat{\tilde{P}}^{(2)}_M\right) \\ &= -\sum_{ijk\ell} Q_{ij}Q_{k\ell}\left(\left[c^\dagger_i c^\dagger_j\right]^{(2)} \cdot \left[\tilde{c}_k\tilde{c}_\ell\right]^{(2)}\right), \end{aligned} \tag{A.10}$$

where

$$\hat{\tilde{P}}^{(2)}_M \equiv (-1)^M \left(P^{\dagger(2)}_{-M}\right)^\dagger = -\sum_{ij} Q_{ij}\left[\tilde{c}_i\tilde{c}_j\right]^{(2)}_M . \tag{A.11}$$

The matrix element of the wavefunction $|i_3i_4; JM\rangle = A^{\dagger(J)}_M(i_3i_4)|0\rangle$ is given as

$$\begin{aligned}\left\langle i_1i_2; JM \left| \sum_M \hat{P}^{\dagger(2)}_M \hat{P}^{(2)}_M \right| i_3i_4; JM \right\rangle &= 2\cdot 2 \sum_{i_1i_2i_3i_4} \frac{Q_{i_1i_2}Q_{i_3i_4}}{\sqrt{(1+\delta_{i_1i_2})(2+\delta_{i_3i_4})}}\delta_{J2} \\ &= 4 \sum_{i_1i_2i_3i_4} \frac{Q_{i_1i_2}Q_{i_3i_4}}{\sqrt{(1+\delta_{i_1i_2})(2+\delta_{i_3i_4})}}\delta_{J2}. \end{aligned} \tag{A.12}$$

A.2.2 Quadrupole-quadrupole interaction

The two-body part of the quadrupole-quadrupole interaction, $:\left(\hat{Q}^{(2)}_M \cdot \hat{Q}^{(2)}_M\right):$, is written as

$$\begin{aligned}:\left(\hat{Q}^{(2)}_M \cdot \hat{Q}^{(2)}_M\right): &= \sum_{ijk\ell} Q_{ij}Q_{k\ell} :\left(\left[c^\dagger_i\tilde{c}_j\right]^{(2)} \cdot \left[c^\dagger_k\tilde{c}_\ell\right]^{(2)}\right): \\ &= \sum_{ijk\ell} Q_{ij}Q_{k\ell}(-1)^2\sqrt{5} :\left[\left[c^\dagger_i\tilde{c}_j\right]^{(2)}\left[c^\dagger_k\tilde{c}_\ell\right]^{(2)}\right]^{(0)}: \\ &= \sum_{ijk\ell} Q_{ij}Q_{k\ell}\sqrt{5}\sum_K(-1)\sqrt{5}\sqrt{5}\hat{K}\hat{K}\left\{\begin{array}{ccc} i & j & 2 \\ k & \ell & 2 \\ K & K & 0 \end{array}\right\}\left[\left[c^\dagger_i c^\dagger_k\right]^{(K)}\left[\tilde{c}_j\tilde{c}_\ell\right]^{(K)}\right]^{(0)}. \end{aligned} \tag{A.13}$$

Here, using

$$\left\{\begin{array}{ccc} i & j & 2 \\ k & \ell & 2 \\ K & K & 0 \end{array}\right\} = \frac{(-1)^{2+K+j+k}}{\sqrt{5}\hat{K}}\left\{\begin{array}{ccc} i & j & 2 \\ \ell & k & K \end{array}\right\}, \tag{A.14}$$

the above equation is written as

$$\begin{aligned}:\left(\hat{Q}^{(2)}_M \cdot \hat{Q}^{(2)}_M\right): &= \sum_{ijk\ell} Q_{ij}Q_{k\ell}\sqrt{5}\sum_K(-1)5\hat{K}\hat{K}\frac{(-1)^{K+j+k}}{\sqrt{5}\hat{K}} \\ &\qquad \times\left\{\begin{array}{ccc} i & j & 2 \\ \ell & k & K \end{array}\right\}\left[\left[c^\dagger_i c^\dagger_k\right]^{(K)}\left[\tilde{c}_j\tilde{c}_\ell\right]^{(K)}\right]^{(0)} \\ &= \sum_{ijk\ell} Q_{ij}Q_{k\ell}\sum_K 5(-1)^{K+j+k+1}\hat{K} \end{aligned}$$

$$
\begin{aligned}
&\times \left\{ \begin{array}{ccc} i & j & 2 \\ \ell & k & K \end{array} \right\} (-1)^{j+\ell-K+1} \left[\left[c_i^\dagger c_k^\dagger \right]^{(K)} \left[\tilde{c}_\ell \tilde{c}_j \right]^{(K)} \right]^{(0)} \\
= & \sum_{ijk\ell} Q_{ij} Q_{k\ell} \sum_K 5(-1)^{k+\ell+1} \hat{K} \\
&\times \left\{ \begin{array}{ccc} i & j & 2 \\ \ell & k & K \end{array} \right\} \left[\left[c_i^\dagger c_k^\dagger \right]^{(K)} \left[\tilde{c}_\ell \tilde{c}_j \right]^{(K)} \right]^{(0)} . \qquad \text{(A.15)}
\end{aligned}
$$

Considering the orthogonalized and symmetrized wavefunction, $|i_3 i_4; JM\rangle = A_M^\dagger(i_3, i_4)\,|0\rangle$ with $A_M^\dagger(i_3, i_4) = \frac{1}{\sqrt{1+\delta_{i_3 i_4}}} \left[c_{i_3}^\dagger c_{i_4}^\dagger \right]_M^{(J)}$,

$$
\begin{aligned}
&\left[\left[c_i^\dagger c_k^\dagger \right]^{(K)} \left[\tilde{c}_\ell \tilde{c}_j \right]^{(K)} \right]^{(0)} |i_3 i_4; JM\rangle = \left[\left[c_i^\dagger c_k^\dagger \right]^{(K)} \left[\tilde{c}_\ell \tilde{c}_j \right]^{(K)} \right]^{(0)} \frac{1}{\sqrt{1+\delta_{i_3 i_4}}} \left[c_{i_3}^\dagger c_{i_4}^\dagger \right]_M^{(J)} |0\rangle \\
&= \frac{1}{\sqrt{1+\delta_{i_3 i_4}}} \left[\left[\left[c_i^\dagger c_k^\dagger \right]^{(K)} \left[\tilde{c}_\ell \tilde{c}_j \right]^{(K)} \right]^{(0)} \left[c_{i_3}^\dagger c_{i_4}^\dagger \right]^{(J)} \right]^{(J)} |0\rangle \\
&= \frac{1}{\sqrt{1+\delta_{i_3 i_4}}} \sqrt{1} \hat{J} \hat{J} \left\{ \begin{array}{ccc} K & K & 0 \\ 0 & J & J \\ J & 0 & J \end{array} \right\} \left[\left[\left[c_i^\dagger c_k^\dagger \right]^{(K)} \times 1 \right]^{(J)} \left[\left[\tilde{c}_\ell \tilde{c}_j \right]^{(K)} \left[c_{i_3}^\dagger c_{i_4}^\dagger \right]^{(J)} \right]^{(0)} \right]^{(J)} |0\rangle . \qquad \text{(A.16)}
\end{aligned}
$$

Here we have assumed contraction of $\left[\tilde{c}_\ell \tilde{c}_j \right]^{(K)}$ and $\left[c_{i_3}^\dagger c_{i_4}^\dagger \right]^{(J)}$. Here, using

$$
\left\{ \begin{array}{ccc} J & J & 0 \\ 0 & J & J \\ J & 0 & J \end{array} \right\} = \left\{ \begin{array}{ccc} 0 & J & J \\ J & 0 & J \\ J & J & 0 \end{array} \right\} = \frac{(-1)^{4J}}{\hat{J}\hat{J}} \left\{ \begin{array}{ccc} 0 & J & J \\ 0 & J & J \end{array} \right\} = \frac{1}{\hat{J}\hat{J}} \frac{(-1)^{2J}}{\hat{J}\hat{J}}, \qquad \text{(A.17)}
$$

the above equation is written as

$$
\begin{aligned}
&\left[\left[c_i^\dagger c_k^\dagger \right]^{(K)} \left[\tilde{c}_\ell \tilde{c}_j \right]^{(K)} \right]^{(0)} |i_3 i_4; JM\rangle \\
&= \frac{1}{\sqrt{1+\delta_{i_3 i_4}}} \hat{J}\hat{J} \frac{1}{\hat{J}\hat{J}} \frac{1}{\hat{J}\hat{J}} \left[\left[c_i^\dagger c_k^\dagger \right]^{(J)} \left[\left[\tilde{c}_\ell \tilde{c}_j \right]^{(J)} \left[c_{i_3}^\dagger c_{i_4}^\dagger \right]^{(J)} \right]^{(0)} \right]^{(J)} |0\rangle \\
&= \frac{1}{\sqrt{1+\delta_{i_3 i_4}}} \frac{1}{\hat{J}\hat{J}} (-1) \hat{J}\hat{J} \left\{ \begin{array}{ccc} \ell & j & J \\ i_3 & i_4 & J \\ 0 & 0 & 0 \end{array} \right\} \left[\left[c_i^\dagger c_k^\dagger \right]^{(J)} \left[\left[\tilde{c}_\ell c_{i_3}^\dagger \right]^{(0)} \left[\tilde{c}_j c_{i_4}^\dagger \right]^{(0)} \right]^{(0)} \right]^{(J)} |0\rangle . \qquad \text{(A.18)}
\end{aligned}
$$

Here we have assumed contractions between ℓ and i_3, and j and i_4. Using

$$
\begin{aligned}
\left\{ \begin{array}{ccc} i_3 & i_4 & J \\ i_3 & i_4 & J \\ 0 & 0 & 0 \end{array} \right\} &= \frac{(-1)^{J+0+i_4+i_3}}{\hat{J}} \left\{ \begin{array}{ccc} i_3 & i_4 & J \\ i_4 & i_3 & 0 \end{array} \right\} = \frac{(-1)^{J+i_4+i_3}}{\hat{J}} \left\{ \begin{array}{ccc} J & i_3 & i_4 \\ 0 & i_4 & i_3 \end{array} \right\} \\
&= \frac{(-1)^{J+i_4+i_3}}{\hat{J}} \frac{(-1)^{J+i_3+i_4}}{\hat{i}_3 \hat{i}_4}, \qquad \text{(A.19)}
\end{aligned}
$$

$$
\begin{aligned}
&\left[\left[c_i^\dagger c_k^\dagger\right]^{(K)}\left[\tilde{c}_\ell \tilde{c}_j\right]^{(K)}\right]^{(0)}|i_3 i_4; JM\rangle \\
&= \frac{1}{\sqrt{1+\delta_{i_3 i_4}}}\frac{1}{\hat{J}\hat{J}}(-1)\hat{J}\hat{J}\frac{(-1)^{J+i_4+i_3}}{\hat{J}}\frac{(-1)^{J+i_3+i_4}}{\hat{i}_3\hat{i}_4}\hat{i}_3\hat{i}_4\left[c_i^\dagger c_k^\dagger\right]^{(J)}\delta_{\ell i_3}\delta_{j i_4}|0\rangle \\
&= \frac{-1}{\sqrt{1+\delta_{i_3 i_4}}}\frac{1}{\hat{J}}\left[c_i^\dagger c_k^\dagger\right]^{(J)}\delta_{\ell i_3}\delta_{j i_4}|0\rangle\,. \qquad \text{(A.20)}
\end{aligned}
$$

Considering contractions between ℓ and i_4, and j and i_3, the result become 2 times of Eq. (A.20)[1],

$$
\left[\left[c_i^\dagger c_k^\dagger\right]^{(K)}\left[\tilde{c}_\ell \tilde{c}_j\right]^{(K)}\right]^{(0)}|i_3 i_4; JM\rangle = \frac{-2}{\sqrt{1+\delta_{i_3 i_4}}}\frac{1}{\hat{J}}\left[c_i^\dagger c_k^\dagger\right]^{(J)}\delta_{\ell i_3}\delta_{j i_4}|0\rangle\,. \qquad \text{(A.21)}
$$

Then the matrix element of the quadrupole-quadrupole moment is given as

$$
\begin{aligned}
&\left\langle i_1 i_2; JM\right|:\left(\hat{Q}_M^{(2)}\cdot\hat{Q}_M^{(2)}\right):\left|i_3 i_4; JM\right\rangle \\
&= \sum_{ijk\ell} Q_{ij}Q_{k\ell}5(-1)^{k+\ell+1}\hat{J} \\
&\qquad \times\left\{\begin{array}{ccc} i & j & 2 \\ \ell & k & J\end{array}\right\}\left\langle i_1 i_2; JM\left|\left[\left[c_i^\dagger c_k^\dagger\right]^{(K)}\left[\tilde{c}_\ell\tilde{c}_j\right]^{(K)}\right]^{(0)}\right|i_3 i_4; JM\right\rangle \\
&= \sum_{ijk\ell} Q_{i_j}Q_{k\ell}5(-1)^{k+\ell+1}\hat{J} \\
&\qquad \times\left\{\begin{array}{ccc} i & j & 2 \\ \ell & k & J\end{array}\right\}\frac{-2}{\sqrt{1+\delta_{i_3 i_4}}}\frac{-2}{\sqrt{1+\delta_{i_1 i_2}}}\frac{1}{\hat{J}}\delta_{i i_1}\delta_{k i_2}\delta_{\ell i_3}\delta_{j i_4} \\
&= 20Q_{i_1 i_4}Q_{i_2 i_3}\frac{1}{\sqrt{1+\delta_{i_3 i_4}}}\frac{1}{\sqrt{1+\delta_{i_1 i_2}}}(-1)^{i_2+i_3}\left\{\begin{array}{ccc} i_1 & i_4 & 2 \\ i_3 & i_2 & J\end{array}\right\}. \qquad \text{(A.22)}
\end{aligned}
$$

A.2.3 Octupole-pairing interaction

In this study, we have not introduced any octpole interactions. However, the importance of the octupole interaction is suggested in experiments as discussed in the text, so as for a future study we need to introduce octupole interactions. In the following, we note the definition of the octupole interaction between like nucleons.

We define the creation operator of the octupole interaction as $\hat{P}_M^{\dagger(3)} = \sum_{ij} O_{ij}[c_i^\dagger c_j^\dagger]_M^{(3)}$. The annihilation operator of the octupole pairing interaction is given as follows,

$$
\begin{aligned}
\hat{P}_M^{(3)} &= \left(\hat{P}_M^{\dagger(3)}\right)^\dagger = \left(\sum_{ij} O_{ij}\left[c_i^\dagger c_j^\dagger\right]_M^{(3)}\right)^\dagger \\
&= \sum_{i\mu j\nu} O_{ij}(i\mu j\nu|3M)c_{j\nu}c_\mu \\
&= \sum_{i\mu j\nu} O_{ij}(i\mu j\nu|3M)(-1)^{j+\nu}\tilde{c}_{j-\nu}(-1)^{i+\mu}\tilde{c}_{j-\mu}
\end{aligned}
$$

[1]The result does not become 2 times of Eq. (A.20) to be precise. Here it is assumed that the antisymmetrization is carried out in the shell model program.

$$
\begin{aligned}
&= \sum_{i\mu j\nu} O_{ij}(i-\mu j-\nu|3M)(-1)^{j-\nu}\tilde{c}_{j\nu}(-1)^{i-\mu}\tilde{c}_{j\mu} \\
&= \sum_{i\mu j\nu} O_{ij}(i\mu j\nu|3-M)(-1)^{i+j-M}\tilde{c}_{j\nu}\tilde{c}_{j\mu} \\
&= \sum_{ij\nu} O_{ij}(-1)^{i+j-M}\left[\tilde{c}_j\tilde{c}_j\right]^{(3)}_{-M} \\
&= -\sum_{ij\nu} O_{ij}(-1)^{M}\left[\tilde{c}_j\tilde{c}_j\right]^{(3)}_{-M}. \qquad \text{(A.23)}
\end{aligned}
$$

Defining $\hat{\tilde{P}}^{(3)}_M \equiv (-1)^M\left(P^{\dagger(3)}_{-M}\right)^\dagger = -\sum_{ij} O_{ij}[\tilde{c}_i\tilde{c}_j]^{(3)}_M$, the octupole pairing interaction, $\sum_M \hat{P}^{\dagger(3)}_M\hat{P}^{(3)}_M$, is written as

$$
\begin{aligned}
\sum_M \hat{P}^{\dagger(3)}_M\hat{P}^{(3)}_M &= \sum_M \hat{P}^{\dagger(3)}_M(-1)\hat{\tilde{P}}^{(3)}_M \\
&= \left(\hat{P}^{\dagger(3)}_M\cdot\hat{\tilde{P}}^{(3)}_M\right) \\
&= -\sum_{ijk\ell} O_{ij}O_{k\ell}\left(\left[c^\dagger_i c^\dagger_j\right]^{(3)}\cdot\left[\tilde{c}_k\tilde{c}_\ell\right]^{(3)}\right), \qquad \text{(A.24)}
\end{aligned}
$$

The matrix element of the wavefunction $|i_3i_4;JM\rangle = A^{\dagger(J)}_M(i_3i_4)|0\rangle$ is given as[2]

$$
\begin{aligned}
\left\langle i_1i_2;JM\left|\sum_M \hat{P}^{\dagger(3)}_M\hat{P}^{(3)}_M\right|i_3i_4;JM\right\rangle &= 2\cdot 2\sum_{i_1i_2i_3i_4}\frac{O_{i_1i_2}O_{i_3i_4}}{\sqrt{(1+\delta_{i_1i_2})(2+\delta_{i_3i_4})}}\delta_{J3} \\
&= 4\sum_{i_1i_2i_3i_4}\frac{O_{i_1i_2}O_{i_3i_4}}{\sqrt{(1+\delta_{i_1i_2})(2+\delta_{i_3i_4})}}\delta_{J3}. \qquad \text{(A.25)}
\end{aligned}
$$

A.2.4 Octupole-octupole interaction

The two-body part of the octupole-octupole interaction, $:\left(\hat{O}^{(2)}_M\cdot\hat{O}^{(2)}_M\right):$, is written as

$$
\begin{aligned}
:\left(\hat{O}^{(3)}_M\cdot\hat{O}^{(3)}_M\right): &= \sum_{ijk\ell} O_{ij}O_{k\ell}:\left(\left[c^\dagger_i\tilde{c}_j\right]^{(3)}\cdot\left[c^\dagger_k\tilde{c}_\ell\right]^{(3)}\right): \\
&= \sum_{ijk\ell} O_{ij}O_{k\ell}(-1)^3\sqrt{7}:\left[\left[c^\dagger_i\tilde{c}_j\right]^{(3)}\left[c^\dagger_k\tilde{c}_\ell\right]^{(3)}\right]^{(0)}: \\
&= -\sum_{ijk\ell} O_{ij}O_{k\ell}\sqrt{7}\sum_K(-1)\sqrt{7}\sqrt{7}\hat{K}\hat{K} \\
&\qquad\times\left\{\begin{array}{ccc} i & j & 3 \\ k & \ell & 3 \\ K & K & 0\end{array}\right\}\left[\left[c^\dagger_i c^\dagger_k\right]^{(K)}\left[\tilde{c}_j\tilde{c}_\ell\right]^{(K)}\right]^{(0)}. \qquad \text{(A.26)}
\end{aligned}
$$

Here, using

$$
\left\{\begin{array}{ccc} i & j & 3 \\ k & \ell & 3 \\ K & K & 0\end{array}\right\} = \frac{(-1)^{3+K+j+k}}{\sqrt{7}\hat{K}}\left\{\begin{array}{ccc} i & j & 3 \\ \ell & k & K\end{array}\right\}, \qquad \text{(A.27)}
$$

[2]This equation is not correctly antisymmetrized. The antisymmetrization is carried out in the shell model program.

the above equation is written as

$$
\begin{aligned}
:\left(\hat{O}^{(3)}_M\cdot\hat{O}^{(3)}_M\right): &= -\sum_{ijk\ell}O_{ij}O_{k\ell}\sqrt{7}\sum_K(-1)7\hat{K}\hat{K}\frac{(-1)^{K+j+k+1}}{\sqrt{7}\hat{K}}\\
&\qquad\times\left\{\begin{array}{ccc} i & j & 3\\ \ell & k & K\end{array}\right\}\left[\left[c^\dagger_i c^\dagger_k\right]^{(K)}\left[\tilde{c}_j\tilde{c}_\ell\right]^{(K)}\right]^{(0)}\\
&= \sum_{ijk\ell}O_{ij}O_{k\ell}\sum_K 7(-1)^{K+j+k+1}\hat{K}\\
&\qquad\times\left\{\begin{array}{ccc} i & j & 3\\ \ell & k & K\end{array}\right\}(-1)^{j+\ell-K+1}\left[\left[c^\dagger_i c^\dagger_k\right]^{(K)}\left[\tilde{c}_\ell\tilde{c}_j\right]^{(K)}\right]^{(0)}\\
&= -\sum_{ijk\ell}O_{ij}O_{k\ell}\sum_K 7(-1)^{k+\ell}\hat{K}\\
&\qquad\times\left\{\begin{array}{ccc} i & j & 3\\ \ell & k & K\end{array}\right\}\left[\left[c^\dagger_i c^\dagger_k\right]^{(K)}\left[\tilde{c}_\ell\tilde{c}_j\right]^{(K)}\right]^{(0)}. \qquad \text{(A.28)}
\end{aligned}
$$

Using the same relation of Eq. (A.21), the matrix element of the wavefunction $|i_3i_4;JM\rangle = A^{\dagger(J)}_M(i_3i_4)|0\rangle$ is given as[3]

$$
\begin{aligned}
&\left\langle i_1i_2;JM\right|:\left(\hat{O}^{(3)}_M\cdot\hat{O}^{(3)}_M\right):\left|i_3i_4;JM\right\rangle\\
&= -\sum_{ijk\ell}O_{ij}O_{k\ell}7(-1)^{k+\ell}\hat{J}\\
&\qquad\times\left\{\begin{array}{ccc} i & j & 3\\ \ell & k & J\end{array}\right\}\left\langle i_1i_2;JM\left|\left[\left[c^\dagger_i c^\dagger_k\right]^{(K)}\left[\tilde{c}_\ell\tilde{c}_j\right]^{(K)}\right]^{(0)}\right|i_3i_4;JM\right\rangle\\
&= -7\sum_{ijk\ell}O_{ij}O_{k\ell}(-1)^{k+\ell}\hat{J}\\
&\qquad\times\left\{\begin{array}{ccc} i & j & 3\\ \ell & k & J\end{array}\right\}\frac{-2}{\sqrt{1+\delta_{i_3i_4}}}\frac{-2}{\sqrt{1+\delta_{i_1i_2}}}\frac{1}{\hat{J}}\delta_{ii_1}\delta_{ki_2}\delta_{\ell i_3}\delta_{ji_4}\\
&= -28Q_{i_1i_4}Q_{i_2i_3}\frac{1}{\sqrt{1+\delta_{i_3i_4}}}\frac{1}{\sqrt{1+\delta_{i_1i_2}}}(-1)^{i_2+i_3}\left\{\begin{array}{ccc} i_1 & i_4 & 3\\ i_3 & i_2 & J\end{array}\right\}. \qquad \text{(A.29)}
\end{aligned}
$$

A.3 Neutron-proton interactions for single-j shells

We define the effective interactions between one neutron in the single j_ν shell and one proton in the single j_π shell. They are given as

$$\hat{H}_{\nu\pi}=\sum_{J=0}^{J_{max}}\chi^{(J)}\hat{U}^{(J)}(j_\nu)\cdot\hat{U}^{(J)}(j_\pi), \qquad \text{(A.30)}$$

where J_{max} is the highest spin and the $\chi^{(J)}$'s indicate strengths of interactions to be determined. The multipole particle-hole operator $\hat{U}^{(J)}_M(j)$ with the total spin J and its

[3]This equation is not correctly antisymmetrized. The antisymmetrization is carried out in the shell model program.

projection M is defined as

$$\begin{aligned} \hat{U}^{(J)}_M(j) &= \frac{1}{\sqrt{2j+1}} \sum_{m_1 m_2} (j m_1 j m_2 | JM) c^\dagger_{jm_1} \tilde{c}_{jm_2} \\ &= \frac{1}{\sqrt{2j+1}} \left[c^\dagger_j \tilde{c}_j \right]^{(J)}_M . \end{aligned} \tag{A.31}$$

The two-body matrix element for the state $|j_\nu j_\pi; L\rangle$ is given as

$$\begin{aligned} &\langle j_\nu j_\pi; L \,| H_{\nu\pi} |\, j_\nu j_\pi; L \rangle \\ &= (-1)^{L+j_\nu+j_\pi} \sum_{J=0}^{J_{max}} \chi^{(J)} \left\{ \begin{array}{ccc} j_\nu & j_\pi & L \\ j_\pi & j_\nu & J \end{array} \right\} . \end{aligned} \tag{A.32}$$

Appendix B

Operators

B.1 The $E2$ transition rate

The $E2$ transition rate is calculated as

$$B(E2; I_i \to I_f) = \frac{1}{2I_i + 1} |\langle \Phi(I_f; f) || \hat{T}(E2) || \Phi(I_i; i) \rangle|^2, \tag{B.1}$$

where $|\Phi(I_i; i)\rangle$ and $|\Phi(I_f; f)\rangle$ represent eigen-wavefunctions of the initial and final states, respectively. Here, the $E2$ transition operator is defined as

$$\hat{T}(E2) = e_\nu \hat{Q}_\nu + e_\pi \hat{Q}_\pi, \tag{B.2}$$

where e_τ ($\tau = \nu$ or π) represents the effective charge of the nucleon, and the operator $\hat{Q}_\tau$ is the quadrupole operator defined as

$$\hat{Q}_{M\tau} = \sum_{j_1 j_2} Q_{j_1 j_2} [c^\dagger_{j_1 \tau} \tilde{c}_{j_2 \tau}]^{(2)}_M, \tag{B.3}$$

where the matrix element $Q_{j_1 j_2}$ is given in Eq. (A.4). Effective charges are adjusted to reproduce experimental $B(E2)$ values in single-closed nuclei.

B.2 The $M1$ transition rate

The $M1$ transition rate is calculated as

$$B(M1, I_i \to I_f) = \frac{1}{2I_i + 1} |\langle \Phi(I_f; f) || \hat{T}(M1) || \Phi(I_i; i) \rangle|^2. \tag{B.4}$$

Here, the $M1$ transition operator is defined as

$$\hat{T}(M1) = \mu_N \sqrt{\frac{3}{4\pi}} \sum_\tau [g_{\ell\tau} \hat{j}_\tau + (g_{s\tau} - g_{\ell\tau}) \hat{s}_\tau], \tag{B.5}$$

where μ_N is the nuclear magneton. The $g_{\ell\nu}$ and $g_{\ell\pi}$ ($g_{s\nu}$ and $g_{s\pi}$) represent the gyromagnetic ratios for orbital angular momenta (spins) for neutrons and protons, respectively. The operators $\hat{j}_\tau$ and $\hat{s}_\tau$ stand for the angular momentum and spin operators, respectively.

B.3 The magnetic dipole moment

The magnetic dipole moment is calculated as

$$\mu(I_i) = \langle \Phi(I_i, M = I_i; i) | \hat{\mu}_0 | \Phi(I_i, M = I_i; i) \rangle. \tag{B.6}$$

The $\hat{\mu}_0$ represents the third-component of the magnetic dipole operator, which is written as

$$\hat{\mu}_M = \mu_N \sum_\tau [g_{\ell\tau} \hat{j}_{M\tau} + (g_{s\tau} - g_{\ell\tau}) \hat{s}_{M\tau}], \tag{B.7}$$

where the operators $\hat{j}_\tau$ and $\hat{s}_\tau$, and the gyromagnetic ratios are taken to be the same as used in the $M1$ transition rates.

B.4 The electric quadrupole moment

The electric quadrupole moment is calculated as

$$Q(I_i) = \left\langle \Phi(I_i, M = I_i; i) \left| \hat{Q}_0 \right| \Phi(I_i, M = I_i; i) \right\rangle. \tag{B.8}$$

Here the electric quadrupole operator is given by

$$\hat{Q}_M = \sqrt{\frac{16\pi}{5}} (e_\nu \hat{Q}_{M\nu} + e_\pi \hat{Q}_{M\pi}). \tag{B.9}$$

The quadrupole operator $\hat{Q}_{M\tau}$ and the effective charge e_τ are taken to be the same as used for the $E2$ transition rates.

B.5 The occupation number

The occupation number in the single-particle orbital j for the state $|\Phi(I_i; i)\rangle$ is evaluated as

$$v^2(j) = \langle \Phi(I_i; i) | \hat{n}_j | \Phi(I_i; i) \rangle, \tag{B.10}$$

where the particle number operator $\hat{n}_j$ in the j orbital is defined as

$$\hat{n}_j = \sum_m c^\dagger_{jm} c_{jm} = -\sqrt{2j+1} \left[c^\dagger_j \tilde{c}_j \right]^{(0)}. \tag{B.11}$$

B.6 The ladder operator

Using the raising operator $\hat{J}^{(1)}_1 = -\frac{1}{\sqrt{2}} \hat{J}^+ = -\frac{1}{\sqrt{2}} (J_x + iJ_y)$, the following relations are given,

$$\hat{J}^+ | \Phi(I_i, M; i) \rangle = \sqrt{I_i(I_i+1) - M(M+1)} | \Phi(I_i, M+1; i) \rangle \tag{B.12}$$

and

$$\hat{J}^{(1)}_1 = \sum_j \frac{1}{\sqrt{3}} \langle j \| \hat{J}^{(1)} \| j \rangle \left[c^\dagger_j \tilde{c}_j \right]^{(1)}_1, \tag{B.13}$$

with

$$\langle j \| \hat{J}^{(1)} \| j \rangle = \sqrt{j(j+1)(2j+1)}. \tag{B.14}$$

Similarly, using the lowering operator $\hat{J}^{(1)}_{-1} = \frac{1}{\sqrt{2}}\hat{J}^{-} = \frac{1}{\sqrt{2}}(J_x - iJ_y)$, the following relations are given,

$$\hat{J}^{-}|\Phi(I_i, M; i)\rangle = \sqrt{I_i(I_i+1) - M(M-1)}|\Phi(I_i, M-1; i)\rangle \tag{B.15}$$

and

$$\hat{J}^{(1)}_{-1} = \sum_j \frac{1}{\sqrt{3}} \langle j \| \hat{J}^{(1)} \| j \rangle \left[c^{\dagger}_j \tilde{c}_j \right]^{(1)}_{-1}. \tag{B.16}$$

Appendix C

Particle-hole conversion

In the following, we use the formulation of Lawson [122]. We define the particle-hole conversion operator Γ for particles in a single j shell as

$$\Gamma\Psi_{IM}(\mathrm{n-particles}) = \Psi_{IM}(\mathrm{n-holes}), \tag{C.1}$$

and Γ is a unitary operator:

$$\Gamma^\dagger\Gamma = \Gamma\Gamma^\dagger = 1. \tag{C.2}$$

Here, we define $|0\rangle$ as the vacuum of particle system. Then $\Gamma|0\rangle$ is a state that the hole system are completely occupied by holes and written as

$$\Gamma|0\rangle = \frac{1}{\Omega!}\{S_+\}^\Omega|0\rangle\,, \tag{C.3}$$

where factor $1/\Omega!$ represents a normalization factor and $\Omega = (2j+1)/2$ is a degeneracy. Here, S_+ is defined as

$$S_+ = \sum_{m>0}(-1)^{j-m}a_m^\dagger a_{-m}^\dagger, \tag{C.4}$$

where $a_m^\dagger$ represents the particle creation operator with the angular momentum j and its projection m. Next, we consider the following single-particle state: $\Gamma a_m^\dagger|0\rangle$. This state is a $2\Omega-1$ particle system with seniority one and uniquely written as

$$\Gamma a_m^\dagger|0\rangle = \frac{1}{(\Omega-1)!}a_m^\dagger\{S_+\}^{(\Omega-1)}|0\rangle\,. \tag{C.5}$$

Here, we use the fact that S_+ makes only a state with seniority zero. We define S_- as

$$S_- = (S_+)^\dagger = \sum_{m>0}(-1)^{j-m}a_{-m}^\dagger a_m^\dagger, \tag{C.6}$$

then it is verified for $p \le q \le \Omega$ that

$$\{S_-\}^p\{S_+\}^q|0\rangle = \frac{q!(\Omega-q+p)!}{(q-p)!(\Omega-q)!}\{S_+\}^{q-p}|0\rangle\,. \tag{C.7}$$

For $q=\Omega$ and $p=1$, it is shown that

$$\{S_+\}^{\Omega-1}|0\rangle = \frac{1}{\Omega}S_-\{S_+\}^\Omega|0\rangle\,, \tag{C.8}$$

and

$$\begin{aligned}\Gamma a_m^\dagger |0\rangle &= \frac{1}{(\Omega-1)!} a_m^\dagger \{S_+\}^{(\Omega-1)} |0\rangle \\ &= \frac{1}{(\Omega-1)!} a_m^\dagger \frac{1}{\Omega} S_- \{S_+\}^{\Omega} |0\rangle \\ &= \frac{1}{\Omega!} a_m^\dagger S_- \{S_+\}^{\Omega} |0\rangle = a_m^\dagger S_- \Gamma |0\rangle . \end{aligned} \tag{C.9}$$

Also,

$$[a_m^\dagger, S_-] = a_m^\dagger S_- - S_- a_m^\dagger = (-1)^{j+m} a_{-m}^\dagger = -\tilde{a}_m, \tag{C.10}$$

and $a_m^\dagger \Gamma |0\rangle = 0$, since particles completely occupy in $\Gamma |0\rangle$. Then

$$\Gamma a_m^\dagger |0\rangle = a_m^\dagger S_- \Gamma |0\rangle = \left(-\tilde{a}_m + S_- a_m^\dagger\right) \Gamma |0\rangle = -\tilde{a}_m |0\rangle . \tag{C.11}$$

By comparing the equation $\Gamma a_m^\dagger |0\rangle = \Gamma a_m^\dagger \Gamma^\dagger \Gamma |0\rangle$,

$$\Gamma a_m^\dagger \Gamma^\dagger = -\tilde{a}_m \tag{C.12}$$

is concluded as for a sufficient condition. Taking the Hermite conjugate of this equation,

$$\Gamma a_m \Gamma^\dagger = (-1)^{j+m} a_{-m}^\dagger. \tag{C.13}$$

is obtained. By operating Γ and $\Gamma^\dagger$,

$$a_m^\dagger = -\Gamma^\dagger \tilde{a}_m \Gamma, \tag{C.14}$$

$$a_m = \Gamma^\dagger (-1)^{j+m} a_{-m}^\dagger \Gamma. \tag{C.15}$$

C.1 Definition of the hole-operator

We define the hole-creation operator as

$$b_m^\dagger \equiv \Gamma a_m^\dagger \Gamma^\dagger = -\tilde{a}_m = (-1)^{j+m} a_{-m}. \tag{C.16}$$

By taking the Hermite conjugate, the hole-annihilation operator is given as

$$b_m \equiv \left(\Gamma a_m^\dagger \Gamma^\dagger\right)^\dagger = \Gamma a_m \Gamma^\dagger = (-1)^{j+m} a_{-m}^\dagger. \tag{C.17}$$

The anti-commutation relation of the creation and annihilation operators is written as

$$\{b_m^\dagger, b_{m'}\} = (-1)^{j+m}(-1)^{j+m'} \{a_{-m}, a_{-m'}^\dagger\} = \delta_{mm'}. \tag{C.18}$$

Namely, the relation between the particle and the hole is written as

$$\tilde{a}_m = -b_m^\dagger, \tag{C.19}$$

$$a_m^\dagger = (-1)^{j-m} b_{-m} = \tilde{b}_m. \tag{C.20}$$

Example 1: $[b_i^\dagger \tilde{b}_j]_M^{(J)}$

Using $b_{im}^\dagger = (-1)^{j+m} a_{j-m}$ and $b_{im} = (-1)^{i+m} a_{i-m}^\dagger$,

$$\begin{aligned}
[b_i^\dagger \tilde{b}_j]_M^{(J)} &= \sum_{m_i m_j} (i m_i j m_j | JM) b_{im_i}^\dagger \tilde{b}_{jm_j} \\
&= \sum_{m_i m_j} (i m_i j m_j | JM)(-1)^{j+m_j} b_{im_i}^\dagger b_{jm_j} \\
&= \sum_{m_i m_j} (i m_i j m_j | JM)(-1)^{j+m_j}(-1)^{i+m_i}(-1)^{j-m_j} a_{i-m_i} a_{jm_j}^\dagger \\
&= \sum_{m_i m_j} (i - m_i j m_j | JM)(-1)^{i+m_i} \left(-a_{jm_j}^\dagger a_{i-m_i} + \delta_{ji}\delta_{m_j - m_i} \right). \qquad \text{(C.21)}
\end{aligned}$$

Example 2: $[\tilde{b}_i \tilde{b}_j]_M^{(J)}$

Using $b_{im} = (-1)^{i+m} a_{i-m}^\dagger$,

$$\begin{aligned}
[\tilde{b}_i \tilde{b}_j]_M^{(J)} &= \sum_{m_i m_j} (i m_i j m_j | JM) \tilde{b}_{im_i} \tilde{b}_{jm_j} \\
&= \sum_{m_i m_j} (i m_i j m_j | JM)(-1)^{i-m_i}(-1)^{j-m_j} b_{i-m_i} b_{j-m_j} \\
&= \sum_{m_i m_j} (i m_i j m_j | JM)(-1)^{i-m_i}(-1)^{j-m_j}(-1)^{i-m_i}(-1)^{j-m_j} a_{im_i}^\dagger a_{jm_j}^\dagger \\
&= \sum_{m_i m_j} (i m_i j m_j | JM)(-1)^{2(i+j)-2(m_i+m_j)} a_{im_i}^\dagger a_{jm_j}^\dagger \\
&= \sum_{m_i m_j} (i m_i j m_j | JM) a_{im_i}^\dagger a_{jm_j}^\dagger. \qquad \text{(C.22)}
\end{aligned}$$

C.2 Matrix elements of the hole-operator

Using the creation-annihilation operator of a particle system, a one -body operator with rank-L is generally written as

$$\begin{aligned}
\hat{O}_M^{(L)} &= \sum_{j_1 j_2} \sum_{m_1 m_2} O_{j_1 j_2}^{(L)} [a_{j_1}^\dagger \tilde{a}_{j_2}]_M^{(L)} \\
&= \sum_{j_1 j_2} \sum_{m_1 m_2} O_{j_1 j_2}^{(L)} (j_1 m_1 j_2 m_2 | LM) a_{j_1 m_1}^\dagger \tilde{a}_{j_2 m_2}. \qquad \text{(C.23)}
\end{aligned}$$

Using the creation-annihilation operator of a hole system, the above equation is written as

$$\begin{aligned}
\hat{O}_M^{(L)} &= \sum_{j_1 j_2} \sum_{m_1 m_2} O_{j_1 j_2}^{(L)} (j_1 m_1 j_2 m_2 | LM) a_{j_1 m_1}^\dagger \tilde{a}_{j_2 m_2} \\
&= \sum_{j_1 j_2} \sum_{m_1 m_2} O_{j_1 j_2}^{(L)} (j_1 m_1 j_2 m_2 | LM)(-1)^{j_1 - m_1} b_{j_1 - m_1} (-1) b_{j_2 m_2}^\dagger. \qquad \text{(C.24)}
\end{aligned}$$

Since the contraction part vanishes except for $L = 0$, then

$$\hat{O}_M^{(L)} = -\sum_{j_1 j_2} \sum_{m_1 m_2} O_{j_1 j_2}^{(L)} (j_1 m_1 j_2 m_2 | LM)(-1)^{j_1 - m_1} b_{j_1 - m_1} b_{j_2 m_2}^\dagger$$

$$
\begin{aligned}
&= \sum_{j_1 j_2} \sum_{m_1 m_2} O^{(L)}_{j_1 j_2} (-1)^{j_1+j_2-L} (j_2 m_2 j_1 m_1 | LM) (-1)^{j_1-m_1} b^\dagger_{j_2 m_2} b_{j_1 -m_1} \\
&= \sum_{j_1 j_2} \sum_{m_1 m_2} O^{(L)}_{j_1 j_2} (-1)^{j_1+j_2-L} (j_2 m_2 j_1 m_1 | LM) (-1)^{j_1-m_1} (-1)^{j_1-m_1} b^\dagger_{j_2 m_2} \tilde{b}_{j_1 m_1} \\
&= \sum_{j_1 j_2} O^{(L)}_{j_1 j_2} (-1)^{j_1+j_2-L} [b^\dagger_{j_2} \tilde{b}_{j_1}]^{(L)}_M \\
&= \sum_{j_1 j_2} O^{(L)}_{j_2 j_1} (-1)^{j_2+j_1-L} [b^\dagger_{j_1} \tilde{b}_{j_2}]^{(L)}_M \\
&\equiv \sum_{j_1 j_2} \bar{O}^{(L)}_{j_1 j_2} [b^\dagger_{j_1} \tilde{b}_{j_2}]^{(L)}_M .
\end{aligned} \tag{C.25}
$$

Namely, the matrix element $\bar{O}^{(L)}_{j_1 j_2} = O^{(L)}_{j_2 j_1} (-1)^{j_1+j_2-L}$ is used for the hole system.

C.3 Particle-hole conversions of operators

C.3.1 Electromagnetic operators

The $M1$ operator
In the $M1$ operator, $L = 1$, $j_1 = j_2$, so the following relation is confirmed:

$$
\bar{M}^{(1)}_{j_1 j_1} = M^{(1)}_{j_1 j_1} (-1)^{j_1+j_1-1} = M^{(1)}_{j_1 j_1} . \tag{C.26}
$$

The sign of the $M1$ operator is not changed by the particle-hole conjugation.

The $E2$ operator
The $E2$ operator is written as

$$
Q^{(2)}_{j_1 j_2} = -\frac{\left\langle j_1 \| r^2 Y^{(2)} \| j_2 \right\rangle}{\sqrt{5}} = C\sqrt{2j_2+1} (-1)^{j_2-j_1} (j_2 \tfrac{1}{2} 20 | j_1 \tfrac{1}{2}), \tag{C.27}
$$

where C is a constant which does not depend on j_1 and j_2. Here, $Q^{(2)}_{j_1 j_2}$ is written as

$$
\begin{aligned}
Q^{(2)}_{j_1 j_2} &= C\sqrt{2j_2+1} (-1)^{j_2-j_1} (j_2 \tfrac{1}{2} 20 | j_1 \tfrac{1}{2}) \\
&= C\sqrt{2j_2+1} (-1)^{j_2-j_1} \sqrt{\frac{2j_1+1}{2j_2+1}} (-1)^{2+0} (j_1 -\tfrac{1}{2} 20 | j_2 -\tfrac{1}{2}) \\
&= C\sqrt{2j_1+1} (-1)^{j_2-j_1} (-1)^{j_1+2-j_2} (j_1 \tfrac{1}{2} 20 | j_2 \tfrac{1}{2}) \\
&= (-1)^{j_1+2-j_2} C\sqrt{2j_1+1} (-1)^{j_1-j_2} (j_1 \tfrac{1}{2} 20 | j_2 \tfrac{1}{2}) \\
&= (-1)^{j_1-j_2} Q^{(2)}_{j_2 j_1} .
\end{aligned} \tag{C.28}
$$

Therefor, $\bar{Q}^{(2)}_{j_1 j_2} = Q^{(2)}_{j_2 j_1} (-1)^{j_1+j_2-2} = (-1)^{j_2-j_1} Q^{(2)}_{j_1 j_2} (-1)^{j_1+j_2-2} = (-1)^{2j_2} Q^{(2)}_{j_1 j_2} = -Q^{(2)}_{j_1 j_2}$. Namely, the sign of the $E2$ operator is changed by the particle-hole conjugation. This is equivalent to the change of the sign of the effective charge.

C.3.2 Operators which mix neutrons and protons

Fermi operator
The Fermi operator is written as

$$\hat{O}(F) = \sum_j -\sqrt{2j+1}[a^\dagger_{j\pi}\tilde{a}_{j\nu}]^{(0)}_0. \tag{C.29}$$

Using the relation, $b^\dagger_m = -\tilde{a}_m$, the Fermi operator is rewritten as

$$\hat{O}(F) = \sum_j -\sqrt{2j+1}[a^\dagger_{j\pi}\tilde{a}_{j\nu}]^{(0)}_0 = \sum_j \sqrt{2j+1}[a^\dagger_{j\pi}\tilde{b}^\dagger_{j\nu}]^{(0)}_0. \tag{C.30}$$

Here, we assume that the operator operates a system in which protons are treated as particles and neutrons are treated as holes. In the first notation, the Fermi operator annihilates one neutron particle and creates one proton particle. In this notation, the Fermi operator creates one neutron hole and one proton particle.

Gamow-Teller operator
The Gamow-Teller operator is written as

$$\hat{O}(GT;\mu) = \sum_{jj'} -\delta_{\ell\ell'}\sqrt{2(2j'+1)(2j+1)}(-1)^{\ell+j'+\frac{3}{2}} \left\{ \begin{array}{ccc} \ell & j' & \frac{1}{2} \\ 1 & \frac{1}{2} & j \end{array} \right\} [a^\dagger_{j'\pi}\tilde{a}_{j\nu}]^{(1)}_\mu. \tag{C.31}$$

Similar to the Fermi operator, the particle-hole conjugation of the Gamow-Teller operator is written as

$$\hat{O}(GT;\mu) = \sum_{jj'} \delta_{\ell\ell'}\sqrt{2(2j'+1)(2j+1)}(-1)^{\ell+j'+\frac{3}{2}} \left\{ \begin{array}{ccc} \ell & j' & \frac{1}{2} \\ 1 & \frac{1}{2} & j \end{array} \right\} [a^\dagger_{j'\pi}b^\dagger_{j\nu}]^{(1)}_\mu. \tag{C.32}$$

Appendix D

Formulas

D.1 Matrix elements of radial part

$$\begin{aligned}
\langle n'\ell'|r|n\ell\rangle &= \sqrt{\frac{2n+2\ell+1}{2}}\delta_{n'n} - \sqrt{n+1}\delta_{n'n+1} \quad \text{for } \ell' = \ell - 1 \\
&= \sqrt{\frac{2n+2\ell+3}{2}}\delta_{n'n} - \sqrt{n}\delta_{n'n-1} \quad \text{for } \ell' = \ell + 1 \qquad \text{(D.1)} \\
\left\langle n'\ell'|r^2|n\ell\right\rangle &= \sqrt{\left(n+\ell+\frac{5}{2}\right)\left(n+\ell+\frac{3}{2}\right)}\delta_{n'n} - 2\sqrt{n\left(n+\ell+\frac{3}{2}\right)}\delta_{n'n-1} \\
&\quad +\sqrt{n(n-1)}\delta_{n'n-2} \qquad \text{for } \ell' = \ell + 2 \\
&= -\sqrt{(n+1)\left(n+\ell+\frac{3}{2}\right)}\delta_{n'n+1} + \left(2n+\ell+\frac{3}{2}\right)\delta_{n'n} \\
&\quad -\sqrt{n\left(n+\ell+\frac{1}{2}\right)}\delta_{n'n-1} \qquad \text{for } \ell' = \ell \\
&= \sqrt{(n+1)(n+2)}\delta_{n'n+2} - 2\sqrt{(n+1)\left(n+\ell+\frac{1}{2}\right)}\delta_{n'n+1} \\
&\quad +\sqrt{\left(n+\ell-\frac{1}{2}\right)\left(n+\ell+\frac{1}{2}\right)}\delta_{n'n} \qquad \text{for } \ell' = \ell - 2 \qquad \text{(D.2)} \\
\left\langle n\ell|r^2|n\ell\right\rangle &= 2n+\ell+\frac{3}{2} \qquad \text{(D.3)}
\end{aligned}$$

Here, everything is calculated in units of b where $b^2 = \frac{\hbar}{m\omega_0}$.

D.2 Clebsh Gordan coefficients

Following notations are based on the Condon-Shortley phase.

$$(j_1 m_1 00|JM) = \delta_{Jj_1Mm_1} \qquad \text{(D.4)}$$

$$(j_1 m_1 j_2 m_2|JM) = (-1)^{j_1+j_2-J}(j_2 m_2 j_1 m_1|JM)$$

$$\begin{aligned} &= (-1)^{j_1+j_2-J}(j_1 - m_1 j_2 - m_2|J-M) \\ &= (j_2 - m_2 j_1 - m_1|J-M) \end{aligned} \tag{D.5}$$

$$\begin{aligned} (j_1 m_1 j_2 m_2|JM) &= (-1)^{j_1-m_1}\sqrt{\frac{2J+1}{2j_2+1}}(j_1 m_1 J - M|j_2 - m_2) \\ &= (-1)^{j_2-m_2}\sqrt{\frac{2J+1}{2j_1+1}}(J - M j_2 m_2|j_1 - m_1) \end{aligned} \tag{D.6}$$

Table D.1: Clebsh-Gordan coefficients: $(jm1/2m'|JM)$

	$m' = 1/2$	$m' = -1/2$
$J = j + 1/2$	$\sqrt{\frac{j+M+1/2}{2j+1}}$	$\sqrt{\frac{j-M+1/2}{2j+1}}$
$J = j - 1/2$	$-\sqrt{\frac{j-M+1/2}{2j+1}}$	$\sqrt{\frac{j+M+1/2}{2j+1}}$

Table D.2: Clebsh-Gordan coefficients: $(jm1m'|JM)$

	$m' = 1$	$m' = 0$	$m' = -1$
$J = j + 1$	$\sqrt{\frac{(j+M)(j+M+1)}{(2j+1)(2j+2)}}$	$\sqrt{\frac{(j-M+1)(j+M+1)}{(2j+1)(j+1)}}$	$\sqrt{\frac{(j-M)(j-M+1)}{(2j+1)(2j+2)}}$
$J = j$	$-\sqrt{\frac{(j+M)(j-M+1)}{2j(j+1)}}$	$\frac{M}{\sqrt{j(j+1)}}$	$\sqrt{\frac{(j-M)(j+M+1)}{2j(j+1)}}$
$J = j - 1$	$\sqrt{\frac{(j-M)(j-M+1)}{2j(2j+1)}}$	$-\sqrt{\frac{(j-M)(j+M)}{j(2j+1)}}$	$\sqrt{\frac{(j+M+1)(j+M)}{2j(2j+1)}}$

D.3 Six-j and nine-j

Rotation

$$\begin{aligned} &\left\{ \begin{array}{ccc} j_1 & j_2 & j_3 \\ \ell_1 & \ell_2 & \ell_3 \end{array} \right\} = \left\{ \begin{array}{ccc} j_2 & j_3 & j_1 \\ \ell_2 & \ell_3 & \ell_1 \end{array} \right\} = \left\{ \begin{array}{ccc} j_3 & j_1 & j_2 \\ \ell_3 & \ell_1 & \ell_2 \end{array} \right\} \\ &= \left\{ \begin{array}{ccc} j_1 & j_3 & j_2 \\ \ell_1 & \ell_3 & \ell_2 \end{array} \right\} = \left\{ \begin{array}{ccc} j_2 & j_1 & j_3 \\ \ell_2 & \ell_1 & \ell_3 \end{array} \right\} = \left\{ \begin{array}{ccc} j_3 & j_2 & j_1 \\ \ell_3 & \ell_2 & \ell_1 \end{array} \right\} \end{aligned} \tag{D.7}$$

$$\left\{ \begin{array}{ccc} j_1 & j_2 & j_3 \\ \ell_1 & \ell_2 & \ell_3 \end{array} \right\} = \left\{ \begin{array}{ccc} j_1 & \ell_2 & \ell_3 \\ \ell_1 & j_2 & j_3 \end{array} \right\} = \left\{ \begin{array}{ccc} \ell_1 & j_2 & \ell_3 \\ j_1 & \ell_2 & j_3 \end{array} \right\} = \left\{ \begin{array}{ccc} \ell_1 & \ell_2 & j_3 \\ j_1 & j_2 & \ell_3 \end{array} \right\} \tag{D.8}$$

$$\left\{ \begin{array}{ccc} j_1 & j_2 & j_3 \\ k_1 & k_2 & k_3 \\ \ell_1 & \ell_2 & \ell_3 \end{array} \right\} = \left\{ \begin{array}{ccc} j_1 & k_1 & \ell_1 \\ j_2 & k_2 & \ell_2 \\ j_3 & k_3 & \ell_3 \end{array} \right\} \tag{D.9}$$

$$\left\{ \begin{array}{ccc} j_1 & j_2 & j_3 \\ k_1 & k_2 & k_3 \\ \ell_1 & \ell_2 & \ell_3 \end{array} \right\} = (-)^{\sum} \left\{ \begin{array}{ccc} k_1 & k_2 & k_3 \\ j_1 & j_2 & j_3 \\ \ell_1 & \ell_2 & \ell_3 \end{array} \right\} = \left\{ \begin{array}{ccc} k_1 & k_2 & k_3 \\ \ell_1 & \ell_2 & \ell_3 \\ j_1 & j_2 & j_3 \end{array} \right\} = \left\{ \begin{array}{ccc} \ell_1 & \ell_2 & \ell_3 \\ j_1 & j_2 & j_3 \\ k_1 & k_2 & k_3 \end{array} \right\} \tag{D.10}$$

Here, $\sum \equiv j_1 + j_2 + j_3 + k_1 + k_2 + k_3 + \ell_1 + \ell_2 + \ell_3$.

Orthogonalization

$$\sum_{j_3}(2j_3+1)(2\ell_3+1)\left\{\begin{array}{ccc} j_1 & j_2 & j_3 \\ \ell_3 & \ell_2 & \ell_3 \end{array}\right\}\left\{\begin{array}{ccc} j_1 & j_2 & j_3 \\ \ell_3 & \ell_2 & \ell_3' \end{array}\right\} = \delta_{\ell_3\ell_3'} \tag{D.11}$$

$$\sum_{J_{13}J_{24}} (2J_{12}+1)(2J_{34}+1)(2J_{13}+1)(2J_{24}+1)\left\{\begin{array}{ccc} j_1 & j_2 & J_{12} \\ j_3 & j_4 & J_{34} \\ J_{13} & J_{24} & J \end{array}\right\}\left\{\begin{array}{ccc} j_1 & j_2 & J_{12}' \\ j_3 & j_4 & J_{34}' \\ J_{13} & J_{24} & J \end{array}\right\} = \delta_{J_{12}J_{12}'}\delta_{J_{34}J_{34}'} \tag{D.12}$$

$$\sum_{J_{12}J_{34}} (2J_{12}+1)(2J_{34}+1)(2J_{13}+1)(2J_{24}+1)\left\{\begin{array}{ccc} j_1 & j_2 & J_{12} \\ j_3 & j_4 & J_{34} \\ J_{13} & J_{24} & J \end{array}\right\}\left\{\begin{array}{ccc} j_1 & j_2 & J_{12} \\ j_3 & j_4 & J_{34} \\ J_{13}' & J_{24}' & J \end{array}\right\} = \delta_{J_{13}J_{13}'}\delta_{J_{24}J_{24}'} \tag{D.13}$$

Composition

$$\sum_{J_{13}}(-)^{J_{12}+J_{23}+J_{13}}(2J_{13}+1)\left\{\begin{array}{ccc} j_1 & j_3 & J_{13} \\ j_2 & J & J_{23} \end{array}\right\}\left\{\begin{array}{ccc} j_2 & j_1 & J_{12} \\ j_3 & J & J_{13} \end{array}\right\} = \left\{\begin{array}{ccc} j_1 & j_2 & J_{12} \\ j_3 & J & J_{23} \end{array}\right\} \tag{D.14}$$

$$\sum_{k}(-)^{\ell_3+\ell_3'+k}(2k+1)\left\{\begin{array}{ccc} j_1 & j_1' & k \\ j_2' & j_2 & j_3 \end{array}\right\}\left\{\begin{array}{ccc} \ell_3 & \ell_3' & k \\ j_1' & j_1 & \ell_2 \end{array}\right\}\left\{\begin{array}{ccc} \ell_3 & \ell_3' & k \\ j_2' & j_2 & \ell_1 \end{array}\right\} = (-)^{j_1+j_2+j_1'+j_2'+\ell_1+\ell_2+j_3}\left\{\begin{array}{ccc} j_1 & j_2 & j_3 \\ \ell_1 & \ell_2 & \ell_3 \end{array}\right\}\left\{\begin{array}{ccc} j_1' & j_2' & j_3 \\ \ell_1 & \ell_2 & \ell_3' \end{array}\right\} \tag{D.15}$$

$$\sum_{J_{14}J_{23}} (-)^{2j_4+J_{23}-J_{24}-J_{34}}(2J_{14}+1)(2J_{23}+1)\left\{\begin{array}{ccc} j_1 & j_2 & J_{12} \\ j_4 & j_3 & J_{34} \\ J_{14} & J_{23} & J \end{array}\right\}\left\{\begin{array}{ccc} j_1 & j_4 & J_{14} \\ j_3 & j_2 & J_{23} \\ J_{13} & J_{24} & J \end{array}\right\} = \left\{\begin{array}{ccc} j_1 & j_2 & J_{12} \\ j_3 & j_4 & J_{34} \\ J_{13} & J_{24} & J \end{array}\right\} \tag{D.16}$$

$$\sum_{J_{25}J_{35}J_{46}} (2J_{25}+1)(2J_{35}+1)(2J_{46}+1) \times \left\{\begin{array}{ccc} J_{25} & J_{46} & J_{13} \\ j_2 & j_4 & J_{24} \\ j_5 & j_6 & J_{56} \end{array}\right\}\left\{\begin{array}{ccc} J_{35} & J_{46} & J_{12} \\ j_3 & j_4 & J_{34} \\ j_5 & j_6 & J_{56}' \end{array}\right\}\left\{\begin{array}{ccc} j_1 & j_2 & J_{12} \\ j_3 & j_5 & J_{35} \\ J_{13} & J_{25} & J_{46} \end{array}\right\} = \frac{\delta J_{56}\delta_{56}'}{2J_{56}+1}\left\{\begin{array}{ccc} j_1 & j_2 & J_{12} \\ j_3 & j_4 & J_{34} \\ J_{13} & J_{24} & J_{56} \end{array}\right\} \tag{D.17}$$

Relation

$$\sum_j (-)^{j_1+j_2+j}(2j+1)\left\{\begin{array}{ccc} j_1 & j_1 & j' \\ j_2 & j_2 & j \end{array}\right\} = \sqrt{(2j_1+1)(2j_2+1)}\delta(j'0) \tag{D.18}$$

$$\begin{aligned}&\left\{\begin{array}{ccc} j_{11} & j_{12} & j_{13} \\ j_{21} & j_{22} & j_{23} \\ j_{31} & j_{32} & j_{33} \end{array}\right\} \\ &= \sum_k (-)^{2k}(2k+1)\left\{\begin{array}{ccc} j_{11} & j_{12} & j_{13} \\ j_{23} & j_{22} & j_{23} \end{array}\right\}\left\{\begin{array}{ccc} j_{21} & j_{22} & j_{23} \\ j_{12} & k & j_{32} \end{array}\right\}\left\{\begin{array}{ccc} j_{31} & j_{32} & j_{33} \\ k & j_{11} & j_{21} \end{array}\right\}\end{aligned} \tag{D.19}$$

Reduction

$$\left\{\begin{array}{ccc} j_1 & j_2 & J \\ j_3 & j_4 & J' \\ K & K' & 0 \end{array}\right\} = \delta(JJ')\delta(KK')\frac{(-)^{J+K+j_2+j_3}}{\sqrt{2J+1}\sqrt{2K+1}}\left\{\begin{array}{ccc} j_1 & j_2 & J \\ j_4 & j_3 & K \end{array}\right\} \tag{D.20}$$

$$\left\{\begin{array}{ccc} j_1 & j_2 & J \\ 0 & j_3 & K \end{array}\right\} = \frac{(-)^{j_1+j_2+j_3}\delta(Jj_3)\delta(Kj_2)}{\sqrt{2J+1}\sqrt{2K+1}} \tag{D.21}$$

$$\left\{\begin{array}{ccc} j_1 & j_2 & j_3 \\ 1 & j_3 & j_2 \end{array}\right\} = (-)^{j_1+j_2+j_3+1}\frac{-j_1(j_1+1)+j_2(j_2+1)+j_3(j_3+1)}{2\sqrt{j_2(j_2+1)(2j_2+1)j_3(j_3+1)(2j_3+1)}} \tag{D.22}$$

D.4 Spherical tensor

$$\left[T^{(\lambda_1)} \times U^{(\lambda_2)}\right]^{(\lambda)}_{\mu} \equiv \sum_{\mu_1\mu_2} (\lambda_1\mu_1\lambda_2\mu_2|\lambda\mu) T^{(\lambda_1)}_{\mu_1} U^{(\lambda_2)}_{\mu_2} \tag{D.23}$$

$$T^{(\lambda)} \cdot U^{(\lambda)} = \sum_{\mu} (-1)^{\mu} T^{(\lambda)}_{\mu} U^{(\lambda)}_{-\mu} = \sqrt{2\lambda+1}(-1)^{\lambda}[T^{(\lambda)} \times U^{(\lambda)}]^{(0)}_0 \tag{D.24}$$

$$\langle j_1 m_1 | T^{(J)}_M | j_2 m_2 \rangle = \frac{1}{\sqrt{2j_1+1}}(j_2 m_2 JM | j_1 m_1)\langle j_1 || T^{(J)} || j_2 \rangle \tag{D.25}$$

$$\begin{aligned}&\langle \alpha' j' || \left[T^{(\lambda_1)} \times U^{(\lambda_2)}\right]^{(\lambda)} || \alpha j \rangle \\ &= \sqrt{2\lambda+1}(-1)^{j'+j+\lambda} \sum_{\alpha'' j''} \left\{\begin{array}{ccc} \lambda_1 & \lambda_2 & \lambda \\ j & j' & j'' \end{array}\right\} \langle \alpha' j' || T^{(\lambda_1)} || \alpha'' j'' \rangle \langle \alpha'' j'' || U^{(\lambda_2)} || \alpha j \rangle\end{aligned} \tag{D.26}$$

$$\langle \alpha' j' || T^{(\lambda)} \cdot U^{(\lambda)} || \alpha j \rangle = \frac{1}{\sqrt{2j+1}} \delta_{jj'} \sum_{\alpha'' j''} (-1)^{j''-j} \langle \alpha' j' || T^{(\lambda)} || \alpha'' j'' \rangle \langle \alpha'' j'' || U^{(\lambda)} || \alpha j \rangle \tag{D.27}$$

If there is no contraction between $c^\dagger_{j_2}$ and $\tilde{c}_{j_3}$,

$$\begin{aligned}
&\left[\left[c^\dagger_{j_1}c^\dagger_{j_2}\right]^{(J_{12})}\left[\tilde{c}_{j_3}\tilde{c}_{j_4}\right]^{(J_{34})}\right]^{(J)}_M \\
&= -\sum_{J_{13}J_{24}}\hat{J}_{12}\hat{J}_{34}\hat{J}_{13}\hat{J}_{24}\left\{\begin{array}{ccc} j_1 & j_2 & J_{12} \\ j_3 & j_4 & J_{34} \\ J_{13} & J_{24} & J \end{array}\right\}\left[\left[c^\dagger_{j_1}\tilde{c}_{j_3}\right]^{(J_{13})}\left[c^\dagger_{j_2}\tilde{c}_{j_4}\right]^{(J_{24})}\right]^{(J)}_M
\end{aligned} \tag{D.28}$$

If $T^{(\lambda)}_2$ and $T^{(\lambda)}_3$ are commutable,

$$\begin{aligned}
&\left[\left[T^{(\lambda_1)}_1\times T^{(\lambda_2)}_2\right]^{(\lambda_{12})}\right]\times\left[\left[T^{(\lambda_3)}_3\times T^{(\lambda_4)}_4\right]^{(\lambda_{34})}\right]^{(J)}_M \\
&=\sum_{\lambda_{13}\lambda_{24}}\hat{\lambda}_{12}\hat{\lambda}_{34}\hat{\lambda}_{13}\hat{\lambda}_{24}\left\{\begin{array}{ccc} \lambda_1 & \lambda_2 & \lambda_{12} \\ \lambda_3 & \lambda_4 & \lambda_{34} \\ \lambda_{13} & \lambda_{24} & J \end{array}\right\}\left[\left[T^{(\lambda_1)}_1\times T^{(\lambda_3)}_3\right]^{(\lambda_{13})}\right]\times\left[\left[T^{(\lambda_2)}_2\times T^{(\lambda_4)}_4\right]^{(\lambda_{24})}\right]^{(J)}_M
\end{aligned} \tag{D.29}$$

$$\begin{aligned}
&\left(\left[T^{(\lambda_1)}_1\times T^{(\lambda_2)}_2\right]^{(\lambda)}\cdot\left[\left[T^{(\lambda_3)}_3\times T^{(\lambda_4)}_4\right]^{(\lambda)}\right)\right. \\
&=(-1)^{\lambda_2+\lambda_3}(2\lambda+1)\sum_\kappa\left\{\begin{array}{ccc} \lambda_1 & \lambda_2 & \lambda \\ \lambda_4 & \lambda_3 & \kappa \end{array}\right\}\left(\left[T^{(\lambda_1)}_1\times T^{(\lambda_3)}_3\right]^{(\kappa)}\right]\cdot\left[\left[T^{(\lambda_2)}_2\times T^{(\lambda_4)}_4\right]^{(\kappa)}\right)
\end{aligned} \tag{D.30}$$

In the following, $T^{(\lambda)}_1$ is an operator which operates on system-1 and $T^{(\lambda)}_2$ is an operator which operates on system-2,

$$\begin{aligned}
&\langle\alpha'_1\alpha'_2(j'_1j'_2)j'||T^{(\lambda)}_1||\alpha_1\alpha_2(j_1j_2)j\rangle \\
&=\delta_{\alpha_2\alpha'_2}\delta_{j_2j'_2}\sqrt{(2j'+1)(2j+1)}(-)^{j_2+\lambda+j'_1+j}\left\{\begin{array}{ccc} j' & \lambda & j \\ j_1 & j_2 & j'_1 \end{array}\right\}\langle\alpha'_1j'_1||T^{(\lambda)}_1||\alpha_1j_1\rangle
\end{aligned} \tag{D.31}$$

$$\begin{aligned}
&\langle\alpha'_1\alpha'_2(j'_1j'_2)j'||T^{(\lambda)}_2||\alpha_1\alpha_2(j_1j_2)j\rangle \\
&=\delta_{\alpha_1\alpha'_1}\delta_{j_1j'_1}\sqrt{(2j'+1)(2j+1)}(-)^{j_1+\lambda+j'_2+j}\left\{\begin{array}{ccc} j' & \lambda & j \\ j_2 & j_1 & j'_2 \end{array}\right\}\langle\alpha'_2j'_2||T^{(\lambda)}_2||\alpha_2j_2\rangle
\end{aligned} \tag{D.32}$$

$$\begin{aligned}
&\langle\alpha'_1\alpha'_2(j'_1j'_2)j'||\left[T^{(\lambda_1)}_1\times T^{(\lambda_2)}_2\right]^{(\lambda)}||\alpha_1\alpha_2(j_1j_2)j\rangle \\
&=\sqrt{(2j'+1)(2\lambda+1)(2j+1)}\left\{\begin{array}{ccc} j_1 & j_2 & j \\ \lambda_1 & \lambda_2 & \lambda \\ j'_1 & j'_2 & j' \end{array}\right\}\langle\alpha'_1j'_1||T^{(\lambda)}_1||\alpha_1j_1\rangle\langle\alpha'_2j'_2||T^{(\lambda)}_2||\alpha_2j_2\rangle
\end{aligned} \tag{D.33}$$

$$\begin{aligned}
&\langle\alpha'_1\alpha'_2(j'_1j'_2)j'||(T^{(\lambda)}_1\cdot T^{(\lambda)}_2)||\alpha_1\alpha_2(j_1j_2)j\rangle \\
&=\delta_{jj'}\sqrt{2j+1}(-)^{(j+j_1+j'_2)}\left\{\begin{array}{ccc} j_1 & j & j_2 \\ j'_2 & \lambda & j'_1 \end{array}\right\}\langle\alpha'_1j'_1||T^{(\lambda)}_1||\alpha_1j_1\rangle\langle\alpha'_2j'_2||T^{(\lambda)}_2||\alpha_2j_2\rangle
\end{aligned} \tag{D.34}$$

D.5 Reduced matrix elements

For angular momentum operator $J^{(1)}$,

$$\left\langle \alpha' j' \left\| J^{(1)} \right\| \alpha j \right\rangle = \delta_{\alpha\alpha'}\delta_{jj'}\sqrt{j(j+1)(2j+1)} \tag{D.35}$$

For spin operator $\sigma^{(1)}$,

$$\left\langle \frac{1}{2} \left\| \sigma^{(1)} \right\| \frac{1}{2} \right\rangle = \sqrt{6} \tag{D.36}$$

For spherical harmonics $C^{(k)}$,

$$\begin{aligned} \left\langle \alpha' j \ell' \left\| C^{(k)} \right\| \alpha \ell \right\rangle &= \delta_{\alpha\alpha'}\sqrt{2\ell+1}(\ell 0 k 0|\ell' 0) \\ &= \delta_{\alpha\alpha'}\sqrt{(2\ell'+1)(2\ell+1)}(-1)^{\ell} \left\{ \begin{array}{ccc} \ell' & k & \ell \\ 0 & 0 & 0 \end{array} \right\} \end{aligned} \tag{D.37}$$

$$\left\langle \alpha' j \ell' \left\| \hat{1} \right\| \alpha \ell \right\rangle = \delta_{\alpha\alpha'}\delta_{\ell\ell'}\sqrt{2\ell+1} \tag{D.38}$$

$$\begin{aligned} \left\langle \alpha' j \ell' \left\| \hat{r}^{(1)} \right\| \alpha \ell \right\rangle &= \delta_{\alpha\alpha'}\sqrt{\ell+1} \quad \text{for } \ell' = \ell+1 \\ &= 0 \quad \text{for } \ell' = \ell \\ &= -\delta_{\alpha\alpha'}\sqrt{\ell} \quad \text{for } \ell' = \ell-1 \end{aligned} \tag{D.39}$$

$$\begin{aligned} \left\langle \alpha' j \ell' \left\| \hat{\nabla}^{(1)} \right\| \alpha \ell \right\rangle &= -\delta_{\alpha\alpha'}\ell\sqrt{\ell+1} \quad \text{for } \ell' = \ell+1 \\ &= 0 \quad \text{for } \ell' = \ell \\ &= -\delta_{\alpha\alpha'}(\ell+1)\sqrt{\ell} \quad \text{for } \ell' = \ell-1 \end{aligned} \tag{D.40}$$

Bibliography

[1] K. Morita, K. Morimoto, D. Kaji, T. Akiyama, S. Goto, H. Haba, E. Ideguchi, R. Kanungo, K. Katori, H. Koura, H. Kudo, T. Ohnishi, A. Ozawa, T. Suda, K. Sueki, H. Xu, T. Yamaguchi, A. Yoneda, A. Yoshida, and Y. Zhao, J. Phys. Soc. Jpn. **73**, 2593 (2004) .

[2] D. Kaji, K. Morimoto, N. Sato, T. Ichikawa, E. Ideguchi, K. Ozeki, H. Haba, H. Koura, Y. Kudou, A. Ozawa, T. Sumita, T. Yamaguchi, A. Yoneda, A. Yoshida, and K. Morita, J. Phys. Soc. Jpn. **78**, 035003 (2009).

[3] D. Kaji, K. Morimoto, H. Haba, E. Ideguchi, H. Koura, and K. Morita, J. Phys. Soc. Jpn. **85**, 015002 (2016).

[4] K. Morita, K. Morimoto, D. Kaji, H. Haba, K. Ozeki, Y. Kudou, T. Sumita, Y. Wakabayashi, A. Yoneda, K. Tanaka, S. Yamaki, R. Sakai, T. Akiyama, S. Goto, H. Hasebe, M. Huang, T. Huang, E. Ideguchi, Y. Kasamatsu, K. Katori, Y. Kariya, H. Kikunaga, H. Koura, H. Kudo, A. Mashiko, K. Mayama, S. Mitsuoka, T. Moriya, M. Murakami, H. Murayama, S. Namai, A. Ozawa, N. Sato, K. Sueki, M. Takeyama, F. Tokanai, T. Yamaguchi, and A. Yoshida J. Phys. Soc. Jpn. **81**, 103201 (2012).

[5] M. J. Martin, Nucl. Data Sheets **108**, 1583 (2007).

[6] L. P. Gaffney, P. A. Butler, M. Scheck, A. B. Hayes, F. Wenander, M. Albers, B. Bastin, C. Bauer, A. Blazhev, S. Bonig, N. Bree, J. Cederkall, T. Chupp, D. Cline, T. E. Cocolios, T. Davinson, H. De Witte, J. Diriken, T. Grahn, A. Herzan, M. Huyse, D. G. Jenkins, D. T. Joss, N. Kesteloot, J. Konki, M. Kowalczyk, Th. Kroll, E. Kwan, R. Lutter, K. Moschner, P. Napiorkowski, J. Pakarinen, M. Pfeiffer, D. Radeck, P. Reiter, K. Reynders, S. V. Rigby, L. M. Robledo, M. Rudigier, S. Sambi, M. Seidlitz, B. Siebeck, T. Stora, P. Thoele, P. Van Duppen, M. J. Vermeulen, M. von Schmid, D. Voulot, N. Warr, K. Wimmer, K. Wrzosek-Lipska, C. Y. Wu, and M. Zielinska, Nature **497**, 12073 (2013).

[7] P. Walker and G. Dracoulis, **Nature** 399, 35 (1999).

[8] E. Teruya, N. Yoshinaga, K. Higashiyama, A. Odahara, Phys. Rev. C **92**, 034320 (2015).

[9] E. Teruya, N. Yoshinaga, K. Higashiyama, H. Nishibata, A. Odahara, and T. Shimoda, Phys. Rev. C **94**, 014317 (2016).

[10] B. Graner, Y. Chen, E. G. Lindahl, and B. R. Heckel, Phys. Rev. Lett. **116**, 161601 (2016).

[11] R. H. Parker, M. R. Dietrich, M. R. Kalita, N. D. Lemke, K. G. Bailey, M. Bishof, J. P. Greene, R. J. Holt, W. Korsch, Z.-T. Lu, P. Mueller, T. P. O'Connor, and J. T. Singh, Phys. Rev. Lett. **114**, 233002 (2015).

[12] H. Kawamura, H. Arikawa, S. Ezure, K. Harada, T. Hayamizu, T. Inoue, T. Ishikawa, M. Itoh, T. Kato, T. Sato, T. Aoki, T. Furukawa, A. Hatakeyama, K. Hatanaka, K. Imai, T. Murakami, H. S. Nataraj, Y. Shimizu, T. Wakasa, H. P. Yoshida, and Y. Sakemi, Nucl. Instr. Meth. B **317**, 582 (2013).

[13] J. Baron, W. C. Campbell, D. DeMille, J. M. Doyle, G. Gabrielse, Y. V. Gurevich, P. W. Hess, N. R. Hutzler, E. Kirilov, I. Kozyryev, B. R. O ' Leary, C. D. Panda, M. F. Parsons, E. S. Petrik, B. Spaun, A. C. Vutha, and A. D. West, Science **343**, 269 (2014).

[14] M. G. Mayer, Phys. Rev. **75**, 1969 (1949).

[15] M. G. Mayer, Phys. Rev. **78**, 16 (1950).

[16] O. Haxlel, J. H. D. Jensen, and H. E. Suess, Phys. Rev. **75**, 1766 (1949).

[17] P. Navratil, and B. R. Barrett, Phys. Rev. C **57**, 562 (1998).

[18] P. Navratil, J. P. Vary, and B. R. Barrett, Phys. Rev. Lett **84**, 5728 (2000).

[19] P. Navratil, V. G. Gueorguiev, J. P. Vary, W. E. Ormand, and A. Nogga, Phys. Rev. Lett. **99**, 042501 (2007).

[20] P. Navratil, S. Quaglioni, I. Stetcu and B. R. Barrett, J. Phy. G **36**, 083101 (2009).

[21] M. Honma, T. Otsuka, B. A. Brown, and T. Mizusaki, Phys. Rev. C **69**, 034335 (2004).

[22] D. Rudolph, C. Baktash, M. J. Brinkman, M. Devlin, H.-Q. Jin, D. R. LaFosse, L. L. Riedinger, D. G. Sarantites, and C.-H. Yu, Eur. Phys. J. A **4**, 115 (1999).

[23] B. Cheal, E. Mané, J. Billowes, M. L. Bissell, L. Blaum, B. A. Brown, F. C. Charlwood, K. T. Flanagan, D. H. Forest, C. Geppert, M. Honma, A. Jokinen, M. Kowalska, A. Krieger, J. Krämer, I. D. Moore, R. Neugart, G. Neyens, W. Nörtershäuser, M. Schug, H. H. Stroke, P. Vingerhoets, D. T. Yordanov, and M. Žáková, Phys. Rev. Lett. **104**, 252502 (2010).

[24] N. Yoshinaga, K. Higashiyama and P. H. Regan, Phys. Rev. Lett. **78**, 044320 (2008).

[25] K. Sieja, F. Nowacki, K. Langanke, and G. Martinez-Pinedo, Phys. Rev. Lett. **79**, 064310 (2009).

[26] M. Honma, T. Otsuka, T. Mizusaki, and M. Hjorth-Jensen, Phys. Rev. Lett. **80**, 064323 (2009).

[27] K. Higashiyama, N. Yoshinaga, and K. Tanabe, Phys. Rev. Lett. **65**, 054317 (2002).

[28] L. Coraggio, A. Covello, A. Gargano, N. Itaco, and T. T. S. Kuo, Phys. Rev. Lett. **66**, 064311 (2002).

[29] A. Gargano, Eur. Phys. J. A **20**, 103 (2004).

[30] H. Jin, M. Hasegawa, S. Tazaki, K. Kaneko, and Y. Sun, Phys. Rev. C **84**, 044324 (2011).

[31] A. Astier, M.-G. Porquet, Ts. Venkova, D. Verney, Ch. Theisen, G. Duchêne, F. Azaiez, G. Barreau, D. Curien, I. Deloncle, O. Dorvaux, B. J. P. Gall, M. Houry, R. Lucas, N. Redon, M. Rousseau, and O. Stézowski, Phys. Rev. C **85**, 064316 (2011).

[32] H. K. Wang, Y. Sun, H. Jin, K. Kaneko, and S. Tazaki, Phys. Rev. C **88**, 054310 (2013).

[33] G. H. Lang, C. W. Johnson, S. E. Koonin, and W. E. Ormand, Phys. Rev. C **48**, 1518 (1993).

[34] M. Honma, T. Mizusaki, and T. Otsuka, Phys. Rev. Lett **75**, 1284 (1995).

[35] N. Yoshinaga and A. Arima, Phys. Rev. C **81**, 044316 (2010).

[36] N. Shimizu, Y. Utsuno, T. Mizusaki, M. Honma, Y. Tsunoda, and T. Otsuka, Phys. Rev. C **85**, 054301 (2012).

[37] A. Bohr and B. R. Mottelson, Nuclear Structure (Addison Wesley Publishing Company, 1962).

[38] P. Ring and P. Schuck, The Nuclear Many-Body Problem (Springer, 1980).

[39] N. Yoshinaga and K. Higashiyama, Phys. Rev. C **69**, 054309 (2004).

[40] K. Higashiyama and N. Yoshinaga, Phys. Rev. C **83**, 034321 (2011).

[41] K. Higashiyama and N. Yoshinaga, Phys. Rev. C **88**, 034315 (2013).

[42] S. Bayer, A. P. Byrne, G. D. Dracoulis, A. M. Baxter, T. Kibedi, and F. G. Kondev, Nucl. Phys. A **694**, 3 (2001).

[43] J. J. Ressler, C. W. Beausang, H. Ai, H. Amro, M. A. Caprio, R. F. Casten, A. A. Hecht, S. D. Langdown, E. A. McCutchan, D. A. Meyer, P. H. Regan, M. J. S. Sciacchitano, A. Yamamoto, and N. V. Zamfir, Phys. Rev. C **69**, 034331 (2004).

[44] F. P. Hessberger, S. Hofmann, I. Kojouharov, and D. Ackermann, Eur. Phys. J. A **22**, 253 (2004).

[45] G. D. Dracoulis, G. J. Lane, A. P. Byrne, P. M. Davidson, T. Kibédi, P. Nieminen, K. H. Maier, H. Watanabe, and A. N. Wilson, Phys. Rev. C **77**, 034308 (2008).

[46] G. D. Dracoulis, P. M. Davidson, G. J. Lane, A. P. Byrne, T. Kibédi, P. Nieminen, A. N. Wilson, and H. Watanabe, Eur. Phys. J. A **127**, 127 (2009).

[47] N. Cieplicka, K. H. Maier, B. Fornal, B. Szpak, R. V. F. Janssens, M. Alcorta, R. Broda, M. P. Carpenter, C. J. Chiara, C. R. Hoffman, B. P. Kay, F. G. Kondev, W. Królas, T. Lauritsen, C. J. Lister, E. A. McCutchan, T. Pawlat, A. M. Rogers, D. Seweryniak, N. Sharp, W. B. Walters, J. Wrzesiński, and S. Zhu, Phys. Rev. C **86**, 054322 (2012).

[48] C. Fry and M. Thoennessen, At. Data Nucl. Data Tables **99**, 365 (2013).

[49] C. Fry and M. Thoennessen, At. Data Nucl. Data Tables **99**, 497 (2013).

[50] V. Margerin, G. J. Lane, G. D. Dracoulis, N. Palalani, M. L. Smith, and A. E. Stuchbery, Phys. Rev. C **93**, 064309 (2016).

[51] J. B. Mcgrory and T. T. S. Kuo, Nucl. Phys. A **247**, 283 (1975).

[52] D. Zwarts and P. W. M. Glaudemans, Z. Phys. A **320**, 487 (1985).

[53] L. Coraggio, A. Covello, A. Gargano, N. Itaco, and T. T. S. Kuo, Phys. Rev. C **58**, 3346 (1998).

[54] L. Coraggio, A. Covello, A. Gargano, N. Itaco, and T. T. S. Kuo, Phys. Rev. C **60**, 064306 (1999).

[55] E. Caurier, M. Rejmund and H. Grawe, Phys. Rev. C **67**, 054310 (2003).

[56] C. W. Ma and W. W. True, Phys. Rev. C **8**, 2313 (1973).

[57] T. R. McGoram, G. D. Dracoulis, A. P. Byrne, A. R. Poletti, and S. Bayer, Nucl. Phys. A **637**, 469 (1998).

[58] K. H. Maier, D. J. Decman, H. Grawe, H. Haas, and W.-D. Zeitz, Hyperfine Interact. **9**, 87 (1981).

[59] Z. Y. Xu, Y. Lei, Y. M. Zhao, S. W. Xu, Y. X. Xie, and A. Arima, Phys. Rev. C **79**, 054315 (2009).

[60] K. Higashiyama and N. Yoshinaga, EPJ Web of Conferences **66**, 02050 (2014).

[61] A. Zemel, and J. Dobes, Phys. Rev. C **27**, 2311 (1983).

[62] N. Yoshida, A. Arima and T. Otsuka, Phys. Lett. B **114**, 86 (1982).

[63] Evaluated Nuclear Structure Data File (ENSDF), [http://www.nndc.bnl.gov/ensdf/].

[64] F. G. Kondev, Nucl. Data Sheets **105**, 1 (2005).

[65] C. J. Chiara, and F. G. Kondev, Nucl. Data Sheets **111**, 141 (2010).

[66] F. G. Kondev, Nucl. Data Sheets **101**, 521 (2004).

[67] F. G. Kondev, Nucl. Data Sheets **109**, 1527 (2008).

[68] F. C. Zawislak, and J. D. Bowman, Nucl. Phys. A **146**, 215 (1970).

[69] F.G. Kondev and S. Lalkovski, Nucl. Data Sheets **112**, 707 (2011).

[70] P. K. Hopke, R. A. Naumann, and K. H. Spejewski, Phys. Rev. **187**, 1709 (1969).

[71] G. Astner, and M. Alpsten, Nucl. Phys. A **140**, 643 (1970).

[72] J. Chena and F. G. Kondeva, Nucl. Data Sheets **126**, 373 (2015).

[73] M. S. Basunia, Nucl. Data Sheets **121**, 561 (2014).

[74] B. Singh, D. Abriola, C. Baglin, V. Demetriou, and T. Johnson, Nucl. Data Sheets **114**, 661 (2013).

[75] I. Bergström, C. J. Herrlander, Th. Lindblad, V. Rahkonen, K.-G. Rensfelt, and K. Westerberg, Z. Phys. A **273**, 291 (1975).

[76] E. Browne, Nucl. Data Sheets **104**, 427 (2005).

[77] M. S. Basunia, Nucl. Data Sheets **108**, 633 (2007).

[78] E. Recknagel, Y. Yamazaki, O. Hashimoto, S. Nagamiya, and K. Nakai, Phys. Lett. B **52**, 414 (1974).

[79] A. P. Byrne, G. D. Dracoulis, C. Fahlander, H. Hubel, A. R. Poletti, A. E. Stuchbery, J. Gerl, and R. F. Davie, Nucl. Phys. A **448**, 137 (1986).

[80] I. Talmi, *Simple Models of Complex Nuclei* (Harwood, Chur, 1993).

[81] T. Otsuka, R. Fujimoto, Y. Utsuno, B. A. Brown, M. Honma, and T. Mizusaki, Phys. Rev. Lett. **87**, 082502 (2001).

[82] T. Otsuka, T. Suzuki, R. Fujimoto, H. Grawe, and Y. Akaishi, Phys. Rev. Lett. **95**, 232502 (2005).

[83] T. Otsuka, T. Suzuki, M. Honma, Y. Utsuno, N. Tsunoda, K. Tsukiyama, and M. Hjorth-Jensen, Phys. Rev. Lett. **104**, 012501 (2010).

[84] K. Kaneko, T. Mizusaki, Y. Sun, and S. Tazaki, Phys. Rev. C **89**, 011302 (2014).

[85] A. Umeya, and K. Muto, Phys. Rev. C **74**, 034330 (2006).

[86] N. Yoshinaga, and K. Higashiyama, Eur. Phys. J. A **30**, 343 (2006).

[87] P. R. Sala, N. Blasi, G. LoBianco, A. Mazzoleni, R. Reinhardt, K. Schiffer, K. P. Schmittgen, G. Siems, and P. von Brentano, Nucl. Phys. A **531**, 383 (1991).

[88] T. Hayakawa, J. Lu, K. Furuno, K. Furutaka, T. Komatsubara, T. Shizuma, N. Hasimoto, T. Saitoh, M. Kidera, Y. Hatsukawa, and M. Oshima, Z. Phys. A **357**, 349 (1997).

[89] V. Kumar, P. Das, R. P. Singh, S. Muralithar, and R. K. Bhowmik, Eur. Phys. J. A **17**, 153 (2003).

[90] L. Chen, P. M. Walker, H. Geissel, Yu. A. Litvinov, K. Beckert, P. Beller, F. Bosch, D. Boutin, L. Caceres, J. J. Carroll, D. M. Cullen, I. J. Cullen, B. Franzke, J. Gerl, M. Górska, G. A. Jones, A. Kishada, R. Knöbel, C. Kozhuharov, J. Kurcewicz, S. A. Litvinov, Z. Liu, S. Mandal, F. Montes, G. Münzenberg, F. Nolden, T. Ohtsubo, Z. Patyk, W. R. Plaß, Zs. Podolyák, S. Rigby, N. Saito, T. Saito, C. Scheidenberger, E. C. Simpson, M. Shindo, M. Steck, B. Sun, S. J. Williams, H. Weick, M. Winkler, H.-J. Wollersheim, and T. Yamaguchi, Phys. Rev. Lett. **110**, 122502 (2013).

[91] A. Astier, and M. Porquet, Phys. Rev. C **83**, 034302 (2011).

[92] G. J. Lane, K. H. Maier, A. P. Byrne, G. D. Dracoulis, R. Brodac, B. Fornal, M. P. Carpenter, R.,M. Clark, M. Cromaz, R. V. F. Janssens, A. O. Macchiavelli, I. Wiedenhover, and K. Vetter, Phys. Lett. B **606**, 34 (2005).

[93] G. J. Lane, R. Broda, B. Fornal, A. P. Byrne, G. D. Dracoulis, J. Blomqvist, R. M. Clark, M. Cromaz, M. A. Deleplanque, R.,M. Diamond, P. Fallon, R. V. F. Janssens, I. Y. Lee, A. O. Macchiavelli, K. H. Maier, M. Rejmund, F. S. Stephens, C. E. Svensson, K. Vetter, D. Ward, I. Wiedenhover, and J. Wrzesinski, Nucl. Phys. A **682**, 71 (2001).

[94] P. A. Mello and J. Flores, Nucl. Phys. **47**, 177 (1963).

[95] Y. E. Kim, and J. O. Rasmussen, Nucl. Phys. **47**, 184 (1963).

[96] G. H. Herling, and T. T. S. Kuo, Nucl. Phys. A **181**, 113 (1972).

[97] P. Alexa, J. Kvasil, N. V. Minh, and R. K. Sheline, Phys. Rev. C **55**, 179 (1997).

[98] L. Coraggio, A. Covello, A. Gargano, and N. Itaco, Phys. Rev. C **76**, 061303 (2007).

[99] L. W. Nordheim, Rev. Mod. Phys. **23**, 322 (1951).

[100] P. Alexa, and R. K. Sheline, Phys. Rev. C **56**, 3087 (1997).

[101] E. R. Flynn, G. J. Igo, R. A. Broglia, S. Landowne, V. Paar, and B. Nilsson, Nucl. Phys. A **195**, 97 (1972).

[102] A. Arima, and L. J. Huang-Lin, Phys. Lett. B **41**, 435 (1972).

[103] J. Li, J. X. Wei, J. N. Hu, P. Ring, and J. Meng, Phys. Rev. C **88**, 064307 (2013).

[104] S.-C. Wu, Nucl. Data Sheets **110**, 681 (2009).

[105] A. Astier, P. Petkov, M.-G. Porquet, D. S. Delion, and P. Schuck, Phys. Rev. Lett. **104**, 042701 (2010).

[106] A. Astier, P. Petkov, M.-G. Porquet, D. S. Delion, and P. Schuck, Eur. Phys. J. A **46** 165 (2010).

[107] Y. Suzuki and S. Ohkubo, Phys. Rev. C **82**, 041303(R) (2010).

[108] D. S. Delion, R. J. Liotta, P. Schuck, A. Astier, and M.-G. Porquet, Phys. Rev. C **85** 064306 (2012).

[109] A. R. Poletti, G. D. Dracoulis, A. P. Byrne, and A. E. Stuchbery, Nucl. Phys. A **473** 595 (1987).

[110] H. W. Taylor, B. Singh, and D. A. Viggars, Phys. Rev. C **34**, 2322 (1986).

[111] M. D. Seliverstov, T. E. Cocolios, W. Dexters, A. N. Andreyev, S. Antalic, A. E. Barzakh, B. Bastin, J. Büscher, I. G. Darby, D. V. Fedorov, V. N. Fedosseev, K. T. Flanagan, S. Franchoo, G. Huber, M. Huyse, M. Keupers, U. Köster, Yu. Kudryavtsev, B. A. Marsh, P. L. Molkanov, R. D. Page, A. M. Sjödin, I. Stefan, P. Van Duppen, M. Venhart, S. G. Zemlyanoy, Phys. Rev. C **89**, 034323 (2014).

[112] I. Hamamoto, Nucl. Phys. A **126**, 545 (1969).

[113] M. Rejmund, K. H. Maier, R. Broda, B. Fornal, M. Lach, J. Wrzesiński, J. Blomqvist, A . Gadea, J. Gerl, M. Górska, H. Grawe, M. Kaspar, H. Schaffner, Ch. Schlegel, R. Schubart, and H.J. Wollersheim, Eur. Phys. J. A **8**, 161 (2000).

[114] B. Singh, Nucl. Data Sheets **114**, 2023 (2013).

[115] T. P. Sjoreen, U. Garg, and D. B. Fossan, Phys. Rev. C **21**, 1838 (1980).

[116] C. F. Liang, P. Paris, and R. K. Sheline, Phys. Rev. C **47**, 1801 (1993).

[117] I. Hamamoto, Nucl. Phys. A **141**, 1 (1970).

[118] I. Hamamoto, Nucl. Phys. A **148**, 465 (1970).

[119] S.-C. Wu, Nucl. Data Sheets **108**, 1057 (2017).

[120] Y. A. Akovali, Nucl. Data Sheets **100**, 141 (2003).

[121] M. Aiche, A. Chevallier, J. Chevallier, S. Hulne, S. Khazrouni, N. Schulz and J. C. Sens, J. Phys. G **14**, 9 (1988).

[122] R. D. Lawson, Theory of the nuclear shell model (Clarendon Press Oxford, 1980).